Development of Microwave Kinetic Inductance Detectors for Visible and Near-IR Astronomy Applications

Paul Nicaise

THÈSE DE DOCTORAT
DE L'UNIVERSITÉ PSL

Préparée à l'Observatoire de Paris

Development of Microwave Kinetic Inductance Detectors for Visible and Near-IR Astronomy Applications

Soutenue par
Paul NICAISE
Le 12 décembre 2022

Ecole doctorale n° 127
Astronomie et Astrophysique d'Ile de France

Spécialité
Instrumentation pour l'Astronomie

Composition du jury :

Martina, WIEDNER Directrice de recherche CNRS, LERMA	*Présidente du jury*
Javier, BRIATICO Directeur de recherche CNRS, Thales	*Rapporteur*
Andrea, CATALANO Chargé de recherche CNRS, LPSC	*Rapporteur*
François, PAJOT Directeur de recherche CNRS, IRAP	*Examinateur*
Marie, POIRIER-QUINOT Professeure des Universités, BioMaps	*Examinateur*
Boon-Kok, TAN Chercheur, Oxford University	*Examinateur*
Faouzi, BOUSSAHA Ingénieur de recherche CNRS, GEPI	*Directeur de thèse*
Piercarlo, BONIFACIO Directeur de recherche CNRS, GEPI	Co-*Directeur*

Acknowledgments

Je tiens à remercier en premier lieu et par-dessus tout mon directeur de thèse Dr. Faouzi Boussaha pour son encadrement de grande qualité durant ces trois années. Les responsabilités qu'il m'a confiées m'ont permis de rapidement m'affirmer dans mon travail et développer des compétences dans de multiples domaines qui se sont reflétées dans ce manuscrit. Nos discussions sur les avancées et objectifs à venir étaient souvent brèves mais efficaces puisque nous avions la même façon d'approcher les problèmes. Sa détermination et son optimisme ont également été une source de motivation indispensable dans les moments difficiles. Je remercie également mon co-directeur de thèse Dr. Piercarlo Bonifacio pour la confiance qu'il m'a donné en co-finançant ce travail dans le cadre du projet SPIAKID qu'il dirige. Ses conseils et remarques ont grandement apporté à la qualité du manuscrit et de la soutenance de thèse. Par ailleurs, les quelques discussions que l'on pouvait avoir sur les objectifs scientifiques de SPIAKID ont toujours su m'enthousiasmer, étant passionné d'astronomie depuis toujours. Un immense merci à toute l'équipe R&D du pôle instrumental GEPI qui m'a chaleureusement accueilli et où l'ambiance était toujours agréable. Je remercie tout particulièrement Mme. Christine Chaumont de m'avoir enseigné les procédés de micro-fabrication. Son expertise et sa patience durant les longues journées d'apprentissage en salle blanche m'ont permis en quelques mois d'obtenir mon autonomie dans un milieu qui m'était encore inconnu auparavant. Je tiens également à remercier tout particulièrement Dr. Jie Hu pour le temps qu'il a dédié à me partager ses connaissances sur la cryogénie, me former à manipuler un cryostat, ainsi que tous les composants qu'il a pris le temps de mesurer. En parallèle, je remercie également Dr. Michel Piat pour son accueil à l'APC et le cryostat qu'il nous a gracieusement mis à disposition. Merci à Dr. Samir Beldi de m'avoir formé à l'utilisation des logiciels de simulation hyperfréquences et pour ses précieux conseils concernant les

MKIDs. Merci à M. Florent Reix pour les innombrables échantillons qu'il a découpé pour moi ainsi que nos discussions régulières sur les différents évènements astronomiques qui avaient lieu. Merci à Mme. Josiane Firminy et M. Thibaut Vacelet de m'avoir transmis leur savoir-faire du wire-bonding, me permettant ainsi d'acquérir une prise en main autonome du montage des composants. Merci à Jean-Marc Martin de m'avoir partagé ses connaissances sur la physique des particules. Merci aussi aux opticiens Mme. Alexine Marret ainsi que M. David Horville avec qui nos discussions sur l'optique autour d'un café pouvaient durer des heures et qui m'aura également initié à l'astrophotographie amateur, renforçant ma passion pour l'astronomie et les problématiques liées à la détection. Enfin, merci au directeur Dr. Hector Flores et aux gestionnaires Mme. Sabine Kimmel et Mme. Melissa Heurtel pour leur accompagnement tout au long de la thèse et avec qui la communication fût toujours efficace. Mis à part le GEPI et l'APC, je tiens à remercier des confrères de trois autres laboratoires: Dr. Michael Rosticher et M. José Palomo à l'ENS pour m'avoir formé à la déposition des couches diélectriques par Atomic Layer Deposition nécessaire pour mon travail de thèse. Merci à M. Pierre Baudoz et M. Aurelien Pelleau au LESIA pour les mesures optiques de couches minces par spectrophotométrie ainsi que Dr. Raphaël Galicher pour l'opportunité de présenter mes travaux devant son équipe HRAA. Enfin, merci au Dr. Lina Gatilova et M. Xavier Lafosse au C2N pour les mesures de couches minces par ellipsométrie. Je remercie l'Observatoire de Paris PSL et le CNRS d'avoir mis à disposition tous les outils nécessaires au bon déroulement de mes travaux. Merci également à l'Ecole Doctorale d'Astrophysique et Astronomie d'Ile de France, en particulier au directeur Dr. Thierry Fouchet, le directeur adjoint Dr. Alain Doressoundiram et la gestionnaire Mme. Géraldine Gaillant avec qui les échanges furent toujours faciles et efficaces. Je remercie aussi mon comité de suivi de thèse composé de Dr. Martina Wiedner et Dr. Jean-Michel Martin pour leur écoute et conseils judicieux lors de nos réunions annuelles concernant les difficultés rencontrées dans mes travaux. Un très grand merci à l'ensemble des membres de mon jury de thèse pour le temps précieux qu'ils m'ont accordé en relisant ce manuscrit, en m'écoutant attentivement lors de la soutenance et en partageant leurs remarques et questions pertinentes : la présidente du jury Dr. Martina Wiedner, les rapporteurs Dr. Javier Briatico et Dr. Andrea Catalano et les examinateurs Dr. François Pajot, Dr. Marie Poirier-Quinot et Dr. Boon-Kok Tan. Je remercie le Centre National d'Etudes Spatiales d'avoir été un acteur principal de ma

Abstract

English version

Microwave Kinetic Inductance Detectors (MKIDs) are superconductive thin films LC resonators with high quality factors. They can simultaneously record single-photon events and measure their energy without any added optics. Combined with the ease of multiplexing thousands of pixels into a large array, MKIDs are now at the heart of current and upcoming ground-based astronomy applications. Among them is the SpectroPhotometric Imaging for Astronomy with Kinetic Inductance Detectors (SPIAKID) project at Paris Observatory. We are using MKID technology to build a 20,000 pixels spectrophotometer that will be deployed in 2024 on the 3.58m New Technology Telescope (NTT) in Chile. SPIAKID aims to study the population and metallicity of stars in Ultra Faint Dwarf (UFD) galaxies in the Local group to have a better understanding of galaxy formation and evolution. We will present an original design intended to improve the optical coupling between incident photons and the absorber part of the detector as well as an anomalous response from our superconductor that could offer a new mean of detection.

Version française

Les détecteurs à inductance cinétique (MKIDs) sont des résonateurs LC à haut facteur de qualité faits à partir de couches minces supraconductrices. Ils peuvent simultanément déterminer le temps d'arrivée de chaque photon en mesurant leur énergie sans optique supplémentaire. Grâce au pouvoir de multiplexage des MKIDs qui permet de facilement réaliser des matrices de plusieurs kilopixels, cette technologie est au centre de l'attention pour les nouvelles applications en astronomie. Parmi eux se trouve l'instrument SpectroPhotometric Imaging for Astronomy with Kinetic Inductance Detectors (SPIAKID), projet du GEPI à l'Observatoire de Paris. Nous utilisons la technologie MKID pour construire un spectrophotomètre composé de 20 000 pixels qui sera déployé sur le New Technology Telescope (NTT) de 3.6m au Chili à l'horizon 2025. SPIAKID s'intéressera à la population stellaire des galaxies naines ultra faibles du Groupe Local pour mieux comprendre la formation des galaxies ainsi que la matière noire. Nous présenterons dans ce travail de thèse un design novateur pour améliorer le couplage optique entre les photons incidents et la partie sensible du détecteur ainsi qu'une réponse anormale de notre supraconducteur qui pourrait faire l'objet d'un nouveau moyen de détection.

Contents

iii

Chapter 1

Introduction

For a long time, our knowledge of the Universe was solely based on what the human eye could see. The help of a telescope could enhance the objects brightness and resolution but increasing the size of optical elements soon faced technological limits. Invented in 1970 [1] the Charged Coupled Devices (CCDs) began to dominate the astronomical UV to NIR observations in the 1980's and progressively led to abandon other types of detectors. The information was stored as bits which allowed for digital post-processing to extract features invisible otherwise. CCDs have now been used for countless of instruments to benefit from their megapixels arrays with high efficiency, ease of manufacture and relatively low cost. Probably the most famous telescope to host CCD-based instruments is the Hubble Space Telescope (HST) that have seen several upgrade in its CCD cameras over the decades [2] with the latest being the Wide Field Camera 3 (WFC3) in 2009. Its 160"×160" UV-optical and 123"×137" NIR arrays allow HST to cover a wide 200-1700 nm wavelength range over a wide Field of View (FoV). WFC3 is a great example of how a mature technology can push the limit of the 30 year-old HST by not only providing incredible images, but also making new scientific discoveries up until today [3]. In recent years, Complementary Metal Oxide Semiconductor (CMOS) have progressively caught up to CCDs low-noise and bit depth performance with faster readout, no blooming, and have been widely used in the infrared. But these semiconductor-based technologies still have two major limiting factors. First, the large bandgap of semiconductors such as silicon or germanium and others makes it challenging to record single-photon events even for high-energy photons [4]. As for photons with energies lower than a fraction of 1 eV (far-infrared

and above), their detection is just not achievable. The second major limiting factor is the dark current noise generated by the detectors own radiation, creating false events. Modern CCD and CMOS technologies are cooled down to temperatures as low as 100 K to maximise the Signal-to-Noise Ratio (SNR) but will still require some integration time in certain cases which can be detrimental for observing transient astronomical events such as gamma ray bursts or to counter atmospheric turbulences for direct imaging of exoplanets at high angular resolution.

1.1 Superconducting detectors for astronomy

1.1.1 The first technologies

The first ever use of a superconductor as a detector was a Transition-Edge Sensor (TES) in 1942 [5], only three decades after the discovery of superconductivity. TES is based on the sudden drop of resistivity in superconductors detailed in Sec. 2.2. In the dark, the detector is kept in a superconductive state right below the critical temperature T_c. Each pixel consists of a resistor in which a constant current is applied. If a photon is absorbed by the load, the radiation dissipates into heat and raises the TES temperature above the superconductive state threshold. While the detection principle is fairly simple, the direct readout of TES leads to Joule heating which creates false events. In 1995, a solution was proposed to use a Superconducting Quantum Interference Device (SQUID) coupled to the TES that would indirectly probe the change of the magnetic field around the resistors [6]. The first technology to operate far below the T_c was the Superconductive Tunnel Junction (STJ) based on the Josephson effect [7]. A thin insulating layer separates two superconducting layers where a voltage is applied. If a photon with enough energy breaks Cooper pairs on one side of the insulating junction, the resulting quasiparticles can go through the junction to occupy an electronic state on the other side via photon-assisted tunneling. Another technology called Superconducting Nanowire Single-Photon Detectors (SNSPD) has rapidly grown in the last couple decades to provide high-efficiency photon-counting [8] with unprecedented temporal resolution [9]. SNSPD consists of a single wire with a cross sectional area of a few nm^2 cooled down below its T_c and lets through a superconducting current just below the critical current. A photon event will break Cooper pairs that temporarily form a resistive barrier in a small region, forcing the

superconducting current to flow around this spot and above the critical current which gives rise to a non-zero resistive value in the DC regime. All these technologies aforementioned can record single-photon events on wide bands but either require a complicated fabrication process or do not scale into large arrays required for wide-field astronomy. In 2003, P. Day et al. from the University of California Santa Barbara (UCSB) proposed a solution to these two major setbacks by introducing Microwave Kinetic Inductance Detectors (MKIDs) [10]. For our application, MKIDs are the right balance between sensitivity, ease of fabrication and large array scaling.

1.1.2   Microwave Kinetic Inductance Detectors

MKIDs are single-photon counting, microsecond-time resolving detectors simultaneously capable of low resolution spectroscopy without any added optics. The intrinsic energy resolution of MKIDs in the visible to NIR bands can vary between 10 and 30 depending on the material used [11–13]. The fabrication process covered in Sec. 3 simply consists of a single superconducting layer patterned as localized inductive and capacitive elements forming a microwave circuit with a resonance frequency f_0. The detection mechanics detailed in Sec. 2.5 comes from the change of kinetic inductance directly related to electrons that form the supercurrent inside the inductor. MKIDs can scale into large arrays by tuning the capacitive value of each pixel to a unique f_0, making it possible to multiplex and read thousands of pixels with a single microwave feedline and drastically reduce the electronics complexity and readout noise. In 2009, a joint effort between three european laboratories (Institut Néel, Grenoble; Astronomy Instrumentation Group, Cardiff; Netherlands Institute for Space Research, Leiden) made possible the development of NIKA (New IRAM KID Array), the first millimetric instrument to use MKIDs technology which was to be installed on the IRAM (Institute for Radio Astronomy in the Millimeter range) 30 m telescope in Spain. In 2013, the NIKA instrument had evolved to a dual-band (150 GHz and 240 GHz) camera with 350 pixels sensitive to both polarizations that demonstrated similar performances to the already mature TES technology [14]. Since then, a second iteration simply called NIKA2 has outperformed NIKA on all fronts with an increase of pixels by a tenfold that cover a circular 6.5 arcmin FoV and is a permanent resident of the 30 m IRAM telescope until 2025 [15]. In parallel to NIKA, the UCSB team responsible for inventing MKIDs and led by B. Mazin were developing between 2009 and 2012

3

ARCONS (ARray Camera for Optical to NIR Spectrophotometry), the first optical to NIR instrument using MKIDs technology. ARCONS was an Integral Field Spectrograph (IFS) with 2,024 pixels covering a 20" × 20" FoV in a 400-1100 nm band with energy resolution of 10 at 400 nm [16]. ARCONS paved the way for the next-generation of optical to near-infrared cameras that followed, starting with DARKNESS (DARK-speckle NIR Energy-resolving Superconducting Spectrophotometer) in 2018 used as a testbed to demonstrate high-contrast exoplanets direct imaging with MKIDs [17]. DARKNESS has 10,000 pixels made from sub-stoichimetric titanium nitride TiN_x (also used in my thesis work) and an energy resolution of 5-7 in its wide 400-1400 nm band similar to ARCONS. The basic principle for exoplanet direct imaging requires a coronagraph that blocks out the light from the parent star and isolate potential companions. However, for ground-based observations prone to atmospheric turbulence, part of the light from the parent star will bleed through the coronagraph and create random speckles of light that severely decreases contrast around the star where companions are now hidden. Active optics can partially remedy to speckles with a closed-loop system that analyzes the incoming distorted wavefront and then controls actuators behind the telescope mirror to locally change its curvature to retrieve the true wavefront. While active optics is enough for some astronomical applications, it falls short for the high-contrast and high-angular resolution needed to isolate Earth-like planets that are usually very close to their parent stars and very dim in comparison. By measuring the arrival of photons with a dead time shorter than the atmospheric speckle decorrelation time, DARKNESS can actually beat the seeing and identify the remaining speckles that active optics cannot handle, which are then removed using the Stochaistic Speckle Discrimination (SSD) post-processing technique [18]. The MEC (MKID Exoplanet Camera) is a direct upgrade from the DARKNESS demonstrator upscaled to 20,000 pixels made from Platinium Silicide (PtSi) with the same energy resolution and operating band [19]. Soon after establishing permanent residency inside the 8 m Subaru telescope in Hawaii, MEC has contributed to the discovery of two low-mass and low-separation companions around two different stars [20, 21]. While MKIDs were first intended to rival with existing technologies in the field of astronomy, they prove to be competitive in many different applications across the electromagnetic spectrum such as neutrino physics experiments or even national security matters [22].

1.2 The SPIAKID science case

In the visible to NIR bands, MKIDs have been the subject of intense studies in the past decade to take advantage of their various benefits listed earlier. The SpectroPhotometric Imaging in Astronomy with Kinetic Inductance Detectors (SPIAKID) will be no exception. We aim to build a broadband 400-1600 nm MKID-based camera that will be installed at the 3.6 m New Technology Telescope (NTT) in Chile in 2025 to derive the age and metallicity from stars that compose Ultra-Faint Dwarf (UFD) galaxies in the Local Group. The performance of SPIAKID will be similar to DARKNESS and MEC except for the pixel number that could reach up to 80,000 by using for the first time in an MKID-based instrument a mosaic of 2×2 arrays.

1.2.1 NTT telescope
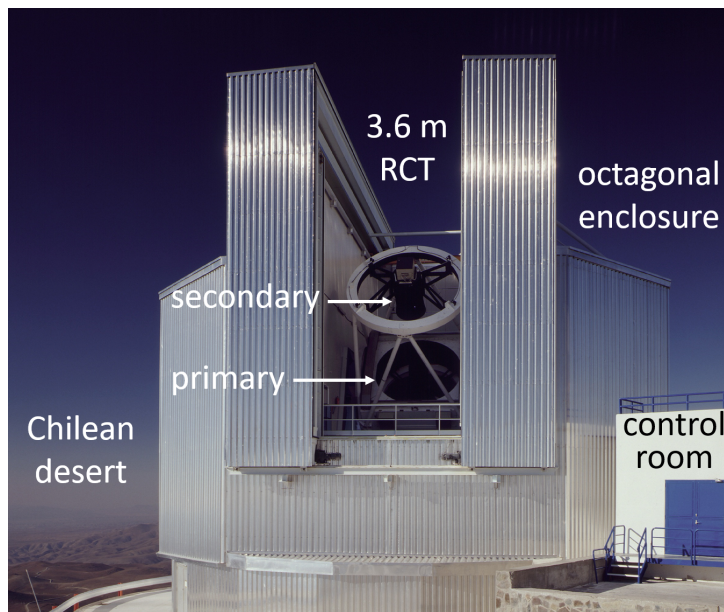
Figure 1.1: The ESO NTT atop La Silla mountain located in the Chilean Atacama desert. The NTT is shown in the operating configuration with the RCT pointing towards the sky inside the octagonal enclosure. An array of MKIDs will be installed at the focal plane of the NTT in 2025 as part of the SPIAKID project. Credit: ESO/C. Madsen

The NTT is a European Southern Observatory (ESO) telescope that saw first light in 1989 at La Silla Observatory in Chile. Due to the complexity of producing large lenses with a homogeneous refractive index, modern optical and near-IR telescopes use reflective optics,

like the NTT, that houses a 3.6 m Ritchey-Chrétien Telescope (RCT). The combination of two parabolic mirrors makes RCTs free of coma and spherical aberrations on a wide FoV. A third elliptical flat mirror is used to redirect incoming light to the instruments that process the data. This configuration has been used on some of the most advanced telescopes like the Very Large Telescope or the Hubble Space Telescope.

The NTT has also pioneered the use of active optics to prevent deformation of the heavy primary mirror falling under its own weight. The mirror is attached to 75 actuators and 24 lateral actuators that locally push or pull the mirror to constantly correct its curvature for optimal image quality. The telescope tracks the sky on an alt-azimuth mount to achieve a more robust and compact mechanical structure than equatorial mounts.

La Silla's location was chosen for multiple reasons. The angular resolution of a ground-based telescope is known to be limited by the seeing of Earth's atmosphere that distort the wavefront of visible light. The high altitude of 2,400 m above sea level and dry environment of the Chilean desert provide some of the best seeing conditions in the world. The observatory is also far from any light-polluted area caused mostly by street lights in cities, one of the main nuisance of ground-based observations that drastically changed the night sky over the last century.

1.2.2 Dwarf and Ultra Faint Dwarf galaxies

In recent models, it has been demonstrated that the formation and evolution of galaxies is related to dark matter. In large spiral galaxies where most of the mass is close to the center, the rotational velocity of neutral hydrogen gas clouds vary only slightly as a function of radial position, which is in disagreement with Kepler's law [23]. This discrepancy between the mass distribution observed in the galaxy and the rotational velocity can be resolved when accounting for dark matter. The majority of the mass of the Universe is supposed to be dark matter that only interacts with normal matter through gravitational waves. It forms structures called dark halos that gravitationally bind and put into motion the normal matter in spiral galaxies outer regions that can consequently reach such velocities. Dark halos are also responsible for binding smaller-size galaxies called dwarfs that are considered the building blocks for larger galaxies [24]. Most dwarf galaxies are billion years old but the abundance of metal-poor constituents they host suggests that

they did not evolve as fast as more massive galaxies like the Milky Way. Up until the 21st century, only a handful of the brightest dwarf galaxies in the nearby Universe called the Local Group were catalogued due to limitations of optical instruments and detectors sensitivity. The two brightest dwarf galaxies orbiting the Andromeda galaxy called M32 and M110 were discovered almost 300 years ago and can be seen in the long-exposure image of Fig. 1.2 captured from my backyard with an amateur astrophotography setup under heavily light-polluted skies.
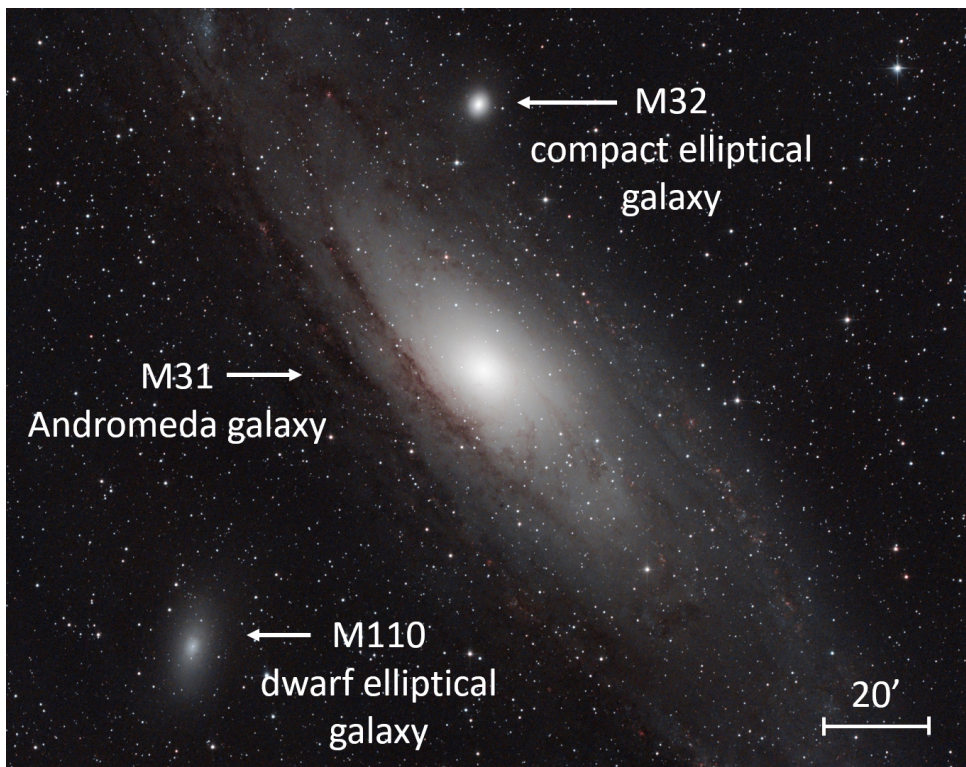
Figure 1.2: Integration of 36 individual 5 min sub-exposures of the Andromeda galaxy and its dwarf satellite galaxies M32 and M110. I captured this field from my backyard in August 2020 using my amateur astrophotography setup that consists of a 0.2 m Newton reflector paired to a 14 bits CMOS sensor cooled down to 0°C on a motorized equatorial mount.

While the result may be aesthetically pleasing, an amateur setup like mine is far from having the angular resolution and sensitivity needed for modern-day science. In 2023, the recently launched James Webb Space Telescope (JWST) will target dwarf companions of both the Milky Way and the Andromeda galaxy as part of the Early Release Science program [25]. The JWST large 6.5 m primary mirror and the absence of atmospheric

perturbations in outer space will allow for an unprecedented resolution of these dwarf galaxies using the NIRCam imager that covers a large 5' × 2' FoV made possible by mosaicking 8 individual sensors.

Between 2004 and 2005, the data from the Sloan Digital Sky Survey allowed the discovery of Willman 1 [26] and Ursa Major I [27], two dwarf galaxies that were particularly faint. These are now classified as UFD galaxies because of their integrated luminosity lower than $10^5 L_\odot$, where $L_\odot$ is the solar luminosity. A few years later, the Dark Energy Survey (DES) in charge of studying millions of galaxies with its large CCD mosaic has pushed the limits of SDSS with eight new confirmed UFDs in the first year [28]. As of 2022, more than 50 UFD galaxies in the Local Group have been catalogued with new candidate discoveries popping up on a monthly basis thanks to DES and other wide-field deep surveys probing the sky [29–31]. UFDs are considered to be the less metal-rich and most dark matter dominated galaxies ever known. The few thousand stars they host would have been responsible for sparking reionization in the early Universe which contributed to the end of the Dark Ages when the Universe was cold, dark and transparent [32, 33].
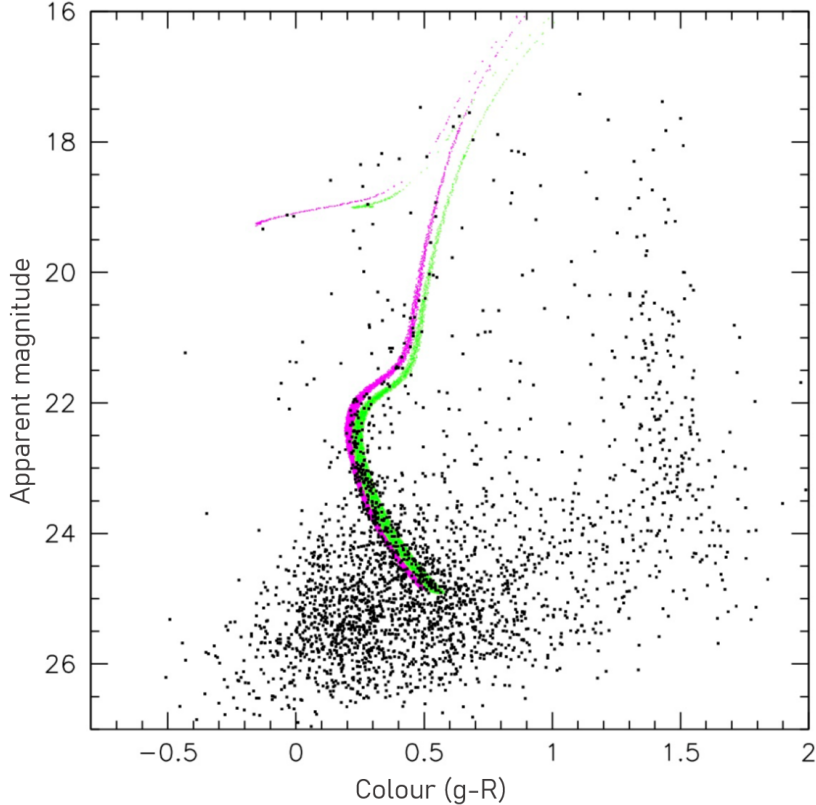
Figure 1.3: Colour-magnitude diagram of the Grus II UFD galaxy in the g and R bands after one hour of observation with a CCD-based instrument in ESO's 8.2 m Antu telescope. The majority of stars in UFD has a higher order of apparent magnitude that prevents accurate spectrometry with semiconductor technologies.

In any galaxy, most elements are synthesised in stars and then dispersed in the interstellar medium. It is usually caused by supernovae explosions, the end stage of the evolution of massive stars, or by stellar winds of fast rotating massive stars and asymptotic giant branch stars [34]. Among the UFDs we expect to find two kinds of objects: galaxies that formed the majority of their stars before reionization was complete [35–37] and tidal dwarfs galaxy that may be formed in galaxy-galaxy interaction. While the former galaxies are necessarily formed by old and very metal-poor stars, the latter can in principle have any metallicity and age, hence the importance to distinguish these two kinds by accurately studying their stellar populations. The pre-reionization fossils are potentially the remnants of the basic "building blocks" that were used to assemble larger galaxies and the tidal galaxies can tell us more about the galaxy interaction history in the Local Group. UFDs are yet to be extensively studied as the sensitivity of current semiconductor

detectors can only observe higher apparent magnitude stars which constitutes a small fraction of the total stellar population in UFD galaxies as seen in Fig. 1.3 and the inefficient multi-band photometry method to successively place colour filters in front of the detector is time-consuming. With the single-photon sensitivity and simultaneous energy resolution over a large spectral band provided by MKIDs technology, SPIAKID is set to image and obtain the spectra of numerous low-magnitude stars over a wide field in record time and hopefully answer some of the most sought-after questions regarding dark matter and early galactic formation.

1.2.3   The KID in SPIAKID

SPIAKID will be designed to target the stellar population of UFD galaxies up to the 24th magnitude in a wide 400-1600 nm band with a 2 arcmin × 2 arcmin FoV on a single observation. With this ambitious goal, the KID at the center of the SPIAKID instrument must meet a few requirements. The absorbing part of the resonator consists of a single 60 nm thick TiN_x layer with a targeted $T_c \approx 1$ K patterned into a meander with 0.5 µm gaps for an expected energy resolution of 10 at 400 nm. The size of the Niobium capacitors is optimized to be read out in the 4-8 GHz microwave bandwidth to avoid the resonator harmonic frequencies above 8 GHz, resulting in a 2 MHz frequency spacing between each pixel achieved by the natural multiplexing power of MKIDs. In total, there are 20,000 pixels equally distributed across 10 readout lines to minimize spectral collisions and cross-talk. It also removes any single point failure because a fabrication defect on the feedline or a faulty readout cable in one of the sub-arrays would affect only 10% of the total number of pixels.
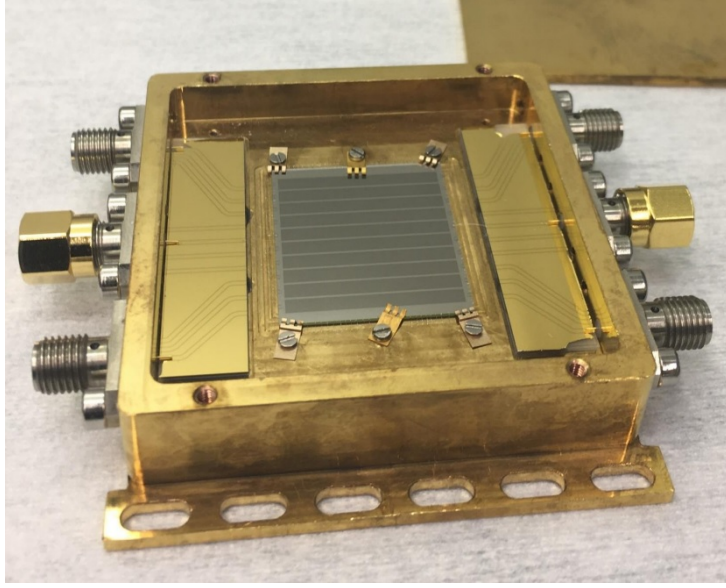
Figure 1.4: Early prototype of the 20,000 pixel array mounted on a gold-plated copper box ready for characterization.

The total size of the array is 23×23 mm^2 so that each pixel covers 0.45 arcsec of the sky that corresponds to an image size of 85 µm in the telescope focal plane. In order to rescale the telescope image to the pixel pitch of 180 µm, the use of optical elements inside the cryostat is necessary to reduce the native f/11 NTT focal ratio by a factor of $\frac{180}{85} = 2.1$ that corresponds to f/23. A microlens array is also placed in front of the pixels to focus the light on the absorbing part of the resonators. For MKIDs, a smaller volume means an increase in sensitivity but the microlens array constraints the minimum size of the absorber. The meander area in SPIAKID has been set to 37×38 µm^2 so that the microlens array can be placed far enough at 0.7 mm above. The pixels will be read continuously by sending a RF signal in the form of a frequency comb with 2 MHz spacing and a time resolution of less than 2 µs. The overall readout noise will be dominated by the cryogenic Low-Noise Amplifier (LNA) so it must be chosen accordingly to stay below the maximal targeted readout noise of -94 dBc·Hz^{-1}.

However, a single 20,000 pixel array in this configuration will only cover a FoV of 1 arcmin which is not enough to image most UFD galaxies in a single observation as shown by the red dashed horizontal line in Fig. 1.5. The spectro-imaging of such UFDs would required at least four exposures, thus increasing the time-on-target by a factor of four.
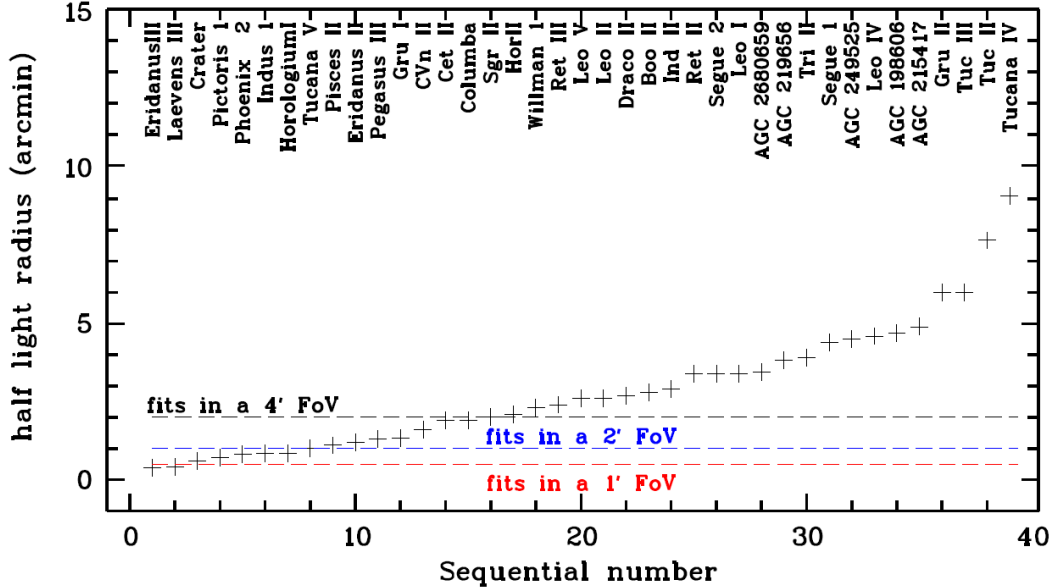
Figure 1.5: Angular size of the known UFD galaxies in our Local Group. The dashed horizontal lines represent the FoV necessary to image the totality of the UFD in a single observation.

To increase the FoV, the SPIAKID instrument is designed to support a 2×2 mosaic of 20,000 pixel arrays at the focal plane. If we demonstrate that the first array can reach the targeted performance, the instrument can hold up to three additional arrays as an unconditional upgrade with the corresponding readout electronics. The full mosaic could then cover a 2 arcmin FoV with the unprecedented number of 80,000 pixels, a feat for an MKID-based instrument.

1.3 Thesis structure and objectives

This thesis work is separated into 5 chapters with the first being this introduction that demonstrates the necessity to use novel detector technologies such as MKIDs to tackle the challenges of modern astronomy. The second chapter will focus towards the basic elements of superconductivity and microwave circuits to fully understand the operating principle of MKIDs and the third chapter will cover the entirety of the actual fabrication and characterization of MKIDs. In the fourth chapter, I will present my extensive work on a new MKIDs geometry designed to increase the optical coupling between incoming photons and the detector using an optical stack. This will include the characterization

of the optical parameters of our thin films to build a model to optimize the thickness of each layer. This study will also demonstrate the feasibility of fabricating such a design and testing it in real conditions using a cryostat and an optical fiber that simulates an astronomical object. The fifth and final chapter that was not originally planned will cover the anomalous response we have witnessed in all of our MKIDs far below the usual operating temperature which was discovered during my thesis. This response has been attributed to thermal perturbations and we have formulated a model presented in that chapter to describe this phenomenon.

Chapter 2

Superconductivity and MKIDs theory

Metals such as titanium, niobium or aluminium used for this work have a superconducting transition temperature when cooled down to cryogenic temperatures. Our detectors take advantage of this superconductive state to reach levels of sensitivity unsurpassed by conventional CCD and CMOS detectors.

2.1 Brief history of superconductivity

In 1911, the first event of superconductivity was recorded by Dutch physicist Heike Onnes while measuring the DC resistivity of mercury at very low temperatures. During the process, the resistivity gradually decreased as the metal was cooled down and suddenly dropped to 0 when the temperature reached 4.2 K. The experiment was repeated for multiple metals that also showed this abrupt transition but each time at a different temperature than mercury. In 1933, German physicist Walther Meissner discovered that superconductors are able to expulse any magnetic field that goes through them [38]. This led the London brothers to formulate two years later the first superconductivity theory from these two notable experimental results. A couple decades later, in 1950, Russian physicists Vitaly Ginzburg and Lev Landau proposed that electrons in a superconductive state form a superfluid and classified superconductors into two types based on their magnetic properties. It was finally in 1957 that American physicists John Bardeen, Leon

Cooper and Robert Schrieffer together formulated the BCS theory to describe superconductivity microscopically and described the behavior of electrons interacting in pairs to form the superfluid [39, 40]. In 1962, B. D. Josephson predicted the supercurrent tunneling through a thin insulator that was previously thought possible only for normal state metals [7]. All of these phenomena will be covered in the following sections.

2.2 Resistivity in superconductors
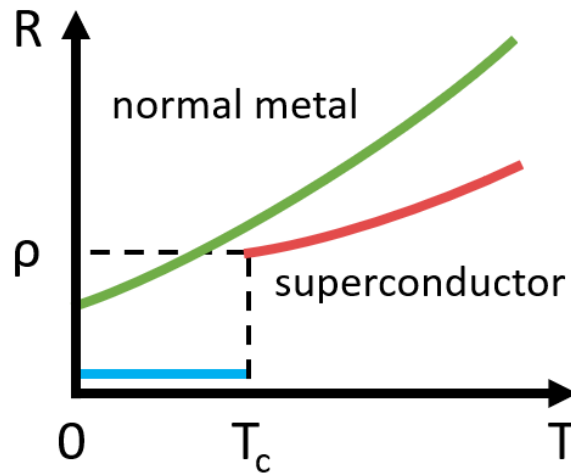
Figure 2.1: For a normal metal, the resistivity decreases continuously in DC mode with decreasing temperature which is not the case for a superconductor where the resistivity suddenly drops to 0 below a certain temperature. We define T_c and ρ respectively as the critical temperature and resistivity at the superconducting transition.

In a given electric field, the resistivity of a metal corresponds to the amount of scattering caused by the collision of free electrons with ions in the lattice. When cooling down a metal in its normal state, resistivity decreases continuously with temperature. However, some metals can transition from a normal to a superconducting state at a specific temperature different for every metal called the critical temperature T_c illustrated in Fig. 2.1. Hence, at $T < T_c$, the passing of an electron can induce lattice vibrations known as phonons that locally increase the density of positive charges. This causes a second electron to be attracted by this polarization through the electron-phonon interaction and creates a Cooper pair 2e represented in Fig. 2.2 with a binding energy 2Δ lower than the Fermi energy [41].
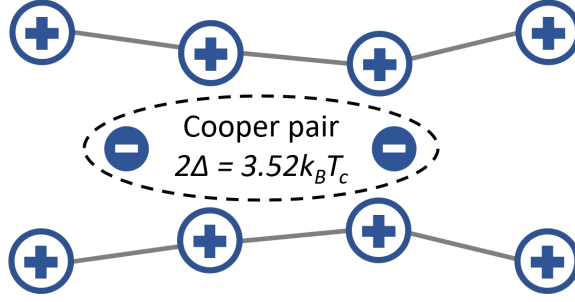
Figure 2.2: Electrons in a superconductor can form pairs by interacting with the positive charges of the metal lattice. At a given time, the electron on the right distorts the lattice it passes through which forms a denser positive area that attracts the left electron, forming a Cooper pair with a total binding energy 2Δ.

For temperatures close to the absolute zero, the binding energy $2\Delta(0)$ is defined according to the BCS theory as follow.

$$2\Delta(0) = 3.52 k_B T_c \tag{2.1}$$

where $k_B = 1.38 \times 10^{-23}$ J·K^{-1} is the Boltzmann constant. The band gap in superconductors is small compared to the one in semiconductors, which makes them interesting for photon detection purposes. The maximum distance at which two electrons can interact is called the coherence length ξ_0, typically on the order of a few micrometers, and can be derived from the BCS theory.

$$\xi_0 = \frac{\hbar v_F}{\pi \Delta(0)} \tag{2.2}$$

where $\hbar = 1.05 \times 10^{-34}$ J·s is the reduced Planck constant and $v_F = 2E_F/m$ is the Fermi velocity of the electrons directly related to the Fermi energy. E_F corresponds to the energy separating the occupied states from the non-occupied states in a Fermi gas at 0 K. Unlike electrons in a normal state, Cooper pairs form a superconducting electron density n_s that do not suffer from scattering inside the metal lattice. Normal electrons follow the Fermi-Dirac statistics as they are fermions with semi-integer spins that can occupy different energy states. However, in a superconductor, two fermions with same spin can form a single Cooper pair with an integer spin that occupies the lowest quantum

16

state known as the Bose-Einstein condensate. All Cooper pairs in the superconductor macroscopically overlap into a single and infinite wave function. This population can thus be accelerated without any loss by a time-varying electric field $\vec{E} = E_0 \exp(jwt)$ with an angular frequency ω, forming a supercurrent with a current density $\vec{J_s}$. Assuming $\vec{E}$ to be uniform and electrons being accelerated by the Lorentz force, we can derive from Newton's second law the first London equation:

$$\frac{\partial \vec{J_s}}{\partial t} = \frac{n_s e^2}{m} \vec{E} \tag{2.3}$$

where e and m are respectively the charge and mass of the electron. We can extract using Ohm's law the complex conductivity in the AC regime from equation 2.3:

$$\sigma(\omega) = \frac{\sigma_0}{1 + j\omega\tau} \tag{2.4}$$

where τ is the mean time between electron-electron collision events and σ_0 is the complex conductivity in the DC regime when $\tau \to \infty$ such as:

$$\sigma_0 = -j\frac{n_s e^2}{\omega m} \tag{2.5}$$

The conductivity σ_0 is purely reactive hence the supercurrent exhibits no DC resistivity.

2.3 Meissner effect
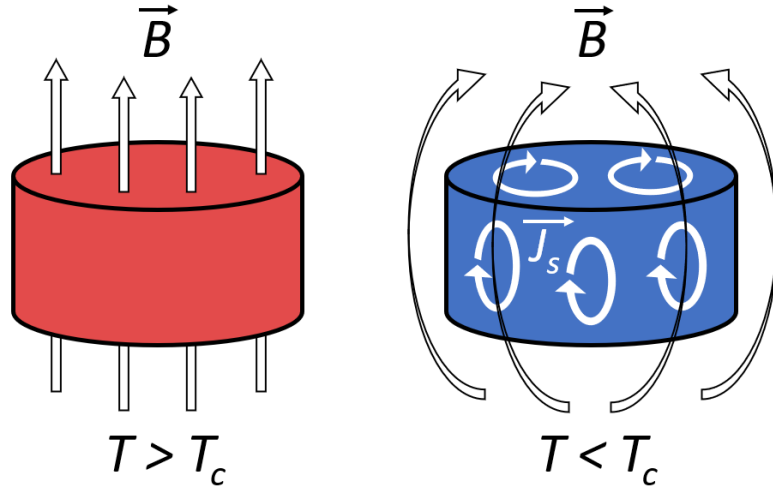
Figure 2.3: The Meissner effect is the repulsion of an external magnetic field $\vec{B}$ when the metal is in its superconductive state (blue cylinder) by producing surface currents.

One other notable feature of superconductors is their near perfect diamagnetism. In a superconducting state, the surface currents of a metal prevents any external magnetic field $\vec{B}$ below the critical magnetic field value to penetrate its bulk except over a small depth λ_L called the London penetration depth. To describe this quantity, we first need to apply Maxwell-Faraday equation to equation 2.3 and derive the second London equation:

$$\vec{\nabla} \times \vec{J}_s = -\frac{n_s e^2}{m} \vec{B} \tag{2.6}$$

Subsequently, the penetration depth can be expressed in Maxwell-Ampère equation by applying equation 2.6:

$$\nabla^2 \vec{B} = \frac{1}{\lambda_L^2} \vec{B} \qquad \text{with} \quad \lambda_L = \sqrt{\frac{m}{\mu_0 n_s e^2}} \tag{2.7}$$

where $\mu_0 = 1.26 \times 10^{-6}$ H·m^{-1} is the vacuum permeability. Considering $x \geq 0$ the depth of the superconductor bulk where $x = 0$ is the surface, a particular solution of equation 2.7 can be written as follow:

$$B(x) = B_0 \exp(-x/\lambda_L) \tag{2.8}$$

As equation 2.8 suggests, the magnetic field rapidly decays inside the superconductor and is divided by e over the characteristic length λ_L that is typically on the order of a few hundred nanometers. For detection purposes that will be further discussed in Sec. 2.7, the thickness t_s of our superconducting films must be $t_s \ll \lambda_L$ to get a homogeneous current density.
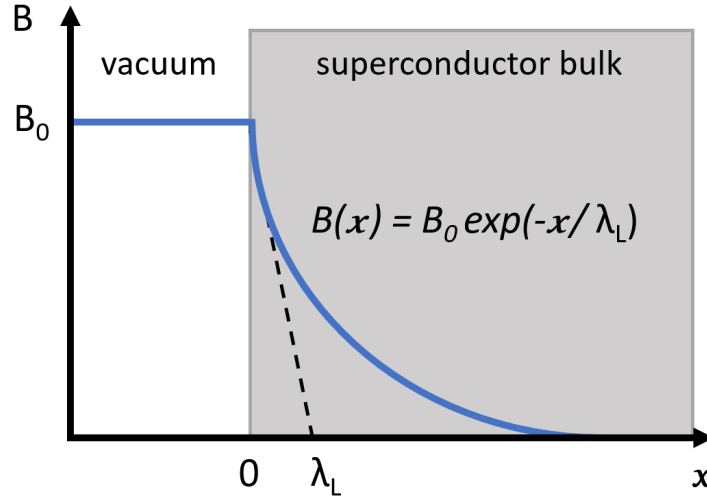
Figure 2.4: Representation of the magnetic field intensity as a function of distance inside the superconductor bulk. The magnetic field is subject to an exponential decay with a characteristic length λ_L.

2.4 Quasiparticles

In a superconductor, some electrons are still thermally excited and cannot form Cooper pairs. These are called quasiparticles that behave like normal electrons with a population density n_{qp} and current density $\vec{J}_{qp}$. If we consider the same electric field $\vec{E}$ described in Sec. 2.2, we can extract the quasiparticle complex conductivity σ_{qp} from the Drude model:

$$\sigma_{qp} = \frac{n_{qp}e^2\tau}{m(1+\omega^2\tau^2)} - j\frac{n_{qp}e^2\omega\tau^2}{m(1+\omega^2\tau^2)} \tag{2.9}$$

19

In the case of normal electrons, the mean time between collisions is on the order of $\tau = 10^{-14}$ s. The usual MKIDs resonance frequency is on the order of $f_0 = 10^9$ Hz so the product $\omega^2\tau^2 \ll 1$ in Eq. 2.9 and thus can be approximated as:

$$\sigma_{qp} = \frac{n_{qp}e^2\tau}{m} \tag{2.10}$$

The paired and unpaired electrons respectively form the normal and superfluid that coexist in a superconductor as defined by the two fluid model [42]. The total population density n can be expressed as:

$$n = n_{qp} + n_s \tag{2.11}$$

The proportion of paired electrons depends on the temperature $T \leq T_c$ of the superconducting material.

$$\frac{n_s}{n} = 1 - \left(\frac{T}{T_c}\right)^4 \tag{2.12}$$

For MKIDs, the n_s/n ratio should be close to 1. The standard operating temperature typically does not go below $T_c/10$ to avoid the increase of TLS noise at lower temperatures [43]. The thermally excited quasiparticles density at $T \ll T_c$ represented in Fig. 2.5 can be approximated for the BCS case by:

$$n_{qp} = 2N_0\sqrt{2\pi k_B T \Delta(0)} \exp\left(-\frac{\Delta(0)}{k_B T}\right) \tag{2.13}$$

where N_0 is the single spin density of states at the Fermi energy and $k_B T$ is the quasiparticle energy. From Eq. 2.13, the total number of quasiparticles in the considered volume V can be expressed as $N_{qp} = n_{qp}V$. If a photon with energy $h\nu > 2\Delta(0)$ is absorbed by the superconductor, it will break a certain number of Cooper pairs into quasiparticles. The excess in quasiparticle density δn_{qp} in this non-equilibrium state is expressed by:

$$\delta n_{qp} = \frac{\eta_{qp}h\nu}{V\Delta(0)} \tag{2.14}$$

where $\eta_{\mathrm{qp}} \approx 0.6$ [44] is the Cooper pair breaking efficiency and V is the volume of the considered absorber. It means that in a superconducting layer with unity absorbance, barely more than half of photons are downconverted to quasiparticles. After a short period of time, quasiparticles will recombine into Cooper pairs by releasing energy in the form of phonons. The characteristic time between the photon event and recombination is called the quasiparticle lifetime noted τ_{qp} that typically lasts several microseconds and can be expressed as [45]:

$$\tau_{qp} = \frac{\tau_0}{n_{qp}} \frac{2N_0(k_B T_c)^3}{4\Delta^2} \tag{2.15}$$

where τ_0 is the characteristic electron-phonon interaction time of the material. During this time, quasiparticles can diffuse over a distance l_{qp} expressed as:

$$l_{qp} = \sqrt{D\tau_{qp}} \tag{2.16}$$

where D is the normal diffusion constant. To increase δn_{qp} which defines the responsivity of MKIDs, we try to reduce V and T_c.
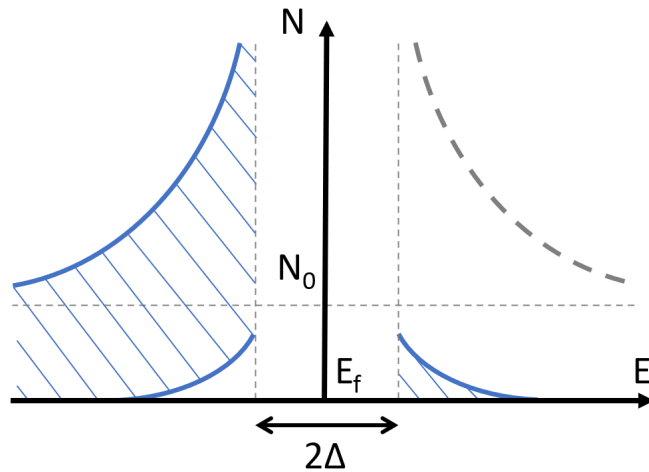
Figure 2.5: The bandgap centered on the Fermi energy separates the two different density of states of electrons in a superconductor. The left side represents electrons in Cooper pairs and on the right, the minimum energy 2Δ they need to acquire to becomes quasiparticles. At non-zero temperature, there is always a small portion of quasiparticles represented in the lower right side that are thermally excited and constitutes the generation-recombination noise floor.

2.5 Kinetic inductance

For a given electric current I passing through an inductive element, the total energy E_{tot} has two components:

$$E_{tot} = E_m + E_k \tag{2.17}$$

where E_m and E_k are respectively the magnetic and kinetic energy. In a normal metal where there is electron scattering, E_m is predominant and is given by:

$$E_m = \frac{1}{2}L_m I^2 \tag{2.18}$$

where L_m is the magnetic component of the inductor and is exclusively geometry-dependant. However, in a superconductor where there is no resistive loss, Cooper pairs acquire an important velocity v_s that translates into kinetic energy E_k expressed as:

$$E_k = \frac{1}{2}n_s m v_s^2 \tag{2.19}$$

If we now apply an alternating current, the inertia of Cooper pairs prevents them from stopping instantly and re-accelerate in the opposite direction. The electric field lags the current by a phase of 90° which creates the inductance involved in the MKIDs detection process called kinetic inductance L_k. The MKIDs inductive absorber typically has a film thickness $t_s \ll \lambda_L$ to ensure a uniform current distribution. In that case, L_k is defined by the Mattis-Bardeen theory as:

$$L_k = \frac{m}{n_s e^2 t_s} \tag{2.20}$$

Another common way to express L_k is related to the BCS theory and is given by:

$$L_k = \frac{\hbar \rho_n}{\pi \Delta t_s} \tag{2.21}$$

where ρ_n is the material resistivity measured right above its T_c. In order to avoid measuring each sample's residual resistivity at very low temperatures which would require a

two-day cooldown cycle in the cryostat, we can instead measure ρ_n once and only measure the resistivity at room temperature ρ_{300K} for all other samples. Then, using the Residual Resistance Ratio $RRR = \rho_{300K}/\rho_n$ that defines the ratio between the material resistivity at room-temperature and before its superconducting transition, we are able to compute the residual resistivity from the room-temperature measurement only. We also define the kinetic inductance fraction α:

$$\alpha = \frac{L_k}{L_k + L_m} \tag{2.22}$$

Since the magnetic inductance do not play any part in MKIDs detection process, α should be close to 1 to improve sensitivity. From equation 2.5, the overall current density at low frequencies ω is still dominated by J_s. At higher frequencies and notably in the microwave range, σ_0 decreases significantly so in order to keep the current constant, electrons are forced to flow through the resistive path. As equation 2.20 and 2.12 suggests, the same behavior is observed when getting closer to the T_c of the superconducting material. Less electrons will form Cooper pairs which constrain the current density to favor the resistive path as well.

2.6   Microwave RLC resonator

MKIDs are superconducting thin films patterned into microwave resonators that have a complex conductivity which is difficult to measure experimentally. Instead, we probe the change of surface impedance and extract the scattering parameters with our readout electronics. The first MKIDs arrays were generally distributed-element circuits such as half-wave or quarter-wave resonators chosen for their unequivalent simplicity and are still used nowadays for certain millimeter and sub-millimeter applications [46]. However, the lack of topological area for multiplexing to produce kilopixels arrays would be too challenging for visible to NIR applications. These resonator lines also have inhomogeneous current density which makes the sensitivity of a pixel spatially dependant. Therefore, we use lumped element resonators where a localized inductor and capacitor form an RLC resonator to completely decouple detection from multiplexing matters. An RLC resonator has an inductance L, a capacitance C and resistive loss R which in our case corresponds to quasiparticles scattering. The electromagnetic response of a thin film can be described

by its surface impedance $Z_s = R + jX$ and can be expressed as follow for an RLC circuit:

$$Z_s = R + j\frac{LC\omega^2 - 1}{C\omega} \tag{2.23}$$

where $\Im(Z) = X$ is the sum of the inductor and capacitor reactance. When these two reactances cancel out and Z_s becomes purely resistive, the circuit will act as a damped harmonic oscillator with a decay proportional to R. The associated angular resonance frequency ω_0 is given by:

$$\omega_0 = \sqrt{\frac{1}{LC}} \tag{2.24}$$

At ω_0, the average energy stored E_{stored} inside the inductor as magnetic energy will be transferred moments later to the capacitor as electric energy and so on, which gives this relation:

$$E_{\text{stored}} = \frac{1}{2}LI^2 = \frac{1}{2}CU^2 \tag{2.25}$$

A similar relation can be applied to the average power dissipated $P_{\text{dissipated}}$ caused by resistive loss R with each oscillation:

$$P_{\text{dissipated}} = \frac{1}{2}RI^2 = \frac{1}{2}\frac{U^2}{R} \tag{2.26}$$

From equations 2.25 and 2.26, we define a critical parameter to describe microwave resonators which is called the internal quality factor Q_i:

$$Q_i = \omega_0 \frac{E_{\text{stored}}}{P_{\text{dissipated}}} = \frac{1}{R}\sqrt{\frac{L}{C}} \tag{2.27}$$

The fabrication process detailed in Sec. 3 plays a key role for obtaining high quality factors of at least $Q_i = 100{,}000$.

2.7 Surface impedance

The surface impedance introduced in Sec. 2.6 can be described by the different physical quantities defined in previous sections. Considering a thin film ($z \approx 0$) with infinite surface in the xy plane, Z_s can be defined by the transverse electromagnetic wave components as:

$$Z_s = \frac{E_x(0)}{B_y(0)} = \sqrt{\frac{j\mu_0\omega}{\sigma}} \qquad (2.28)$$

If we consider the resistive loss to be negligible in the superconducting thin film at MKIDs operating temperature, we can rewrite Eq. 2.28 by handling Maxwell equations and Faraday's law correctly such as:

$$Z_s \approx j\omega\mu_0\lambda_{\text{eff}} \qquad (2.29)$$

where λ_{eff} is the magnetic field effective penetration depth. In fact, the electrodynamic response of our detector can be described by the complex conductivity defined in the Mattis-Bardeen theory [47]. Depending on the properties of the superconducting material, the surface impedance can be approximated either as the extreme anomalous limit ($\xi_0 \gg \lambda_{\text{eff}}$ and $l_{e^-} \gg \lambda_{\text{eff}}$, with l_{e^-} the electron mean free path) or the local limit ($\xi_0 \gg l_{e^-}$ and $\lambda_{\text{eff}} \gg l_{e^-}$) In our case, the sensitive absorber is made of TiN that has a reported Fermi velocity $v_F(\text{TiN}) = 7 \times 10^5$ m·s and electron free mean path $l_{e^-}(\text{TiN}) = 50$ nm [48]. The resulting TiN coherence length computed from Eq. 2.2 is $\xi_0(\text{TiN}) \approx 100$ nm. The thin film we deposit for the MKID absorber has a thickness $t < l_{e^-}$, in this case the effective penetration depth can be approximated by [49]:

$$\lambda_{\text{eff}} \approx \sqrt{\frac{\xi_0}{t}} \qquad (2.30)$$

The quasiparticle excess induced by a photon event expressed in Eq. 2.14 is responsible for the fractional change of surface impedance:

$$\frac{\delta Z_s}{Z_s} = \frac{\delta n_{qp}}{2N_0\Delta} \qquad (2.31)$$

Since detection is measured through this fractional change, Eq. 2.31 shows the importance of having a low-T_c material patterned in a reduced volume (i.e. Eq. 2.14) cooled at temperatures $T \leq T_c$ to increase sensitivity.

2.8 MKID operating process

As explained in Sec. 2.5, MKIDs can detect photons via the change of kinetic inductance inside the inductor where the Cooper pair density is the highest. When a photon $h\nu > 2\Delta$ is absorbed by the inductor, some Cooper pairs are broken into quasiparticles that can in turn break more Cooper pairs if they have still more energy than the bandgap, creating a cascade that changes n_s/n. To grasp the influence of this variation on the resonator, we can rewrite equation 2.24 as:

$$f_0 = \frac{1}{2\pi\sqrt{(L_k + L_m)C}} \tag{2.32}$$

In the dark, the RLC circuit is characterized by a transmission dip and a steep phase slope on resonance. When there is a photon event, the overall kinetic inductance increases which creates a frequency shift Δf but also a phase shift $\Delta\phi$ that is characterized as a pulse response in the time-domain. Moreover, the Q_i is affected by the increase of n_{qp}, the resistive loss will increase which will translate into a reduced dip amplitude.

$$n_s \searrow \implies L_k = \frac{m_e}{n_s e^2} \nearrow \implies f_0 = \frac{1}{2\pi\sqrt{(L_m + L_k)\,C}} \searrow$$
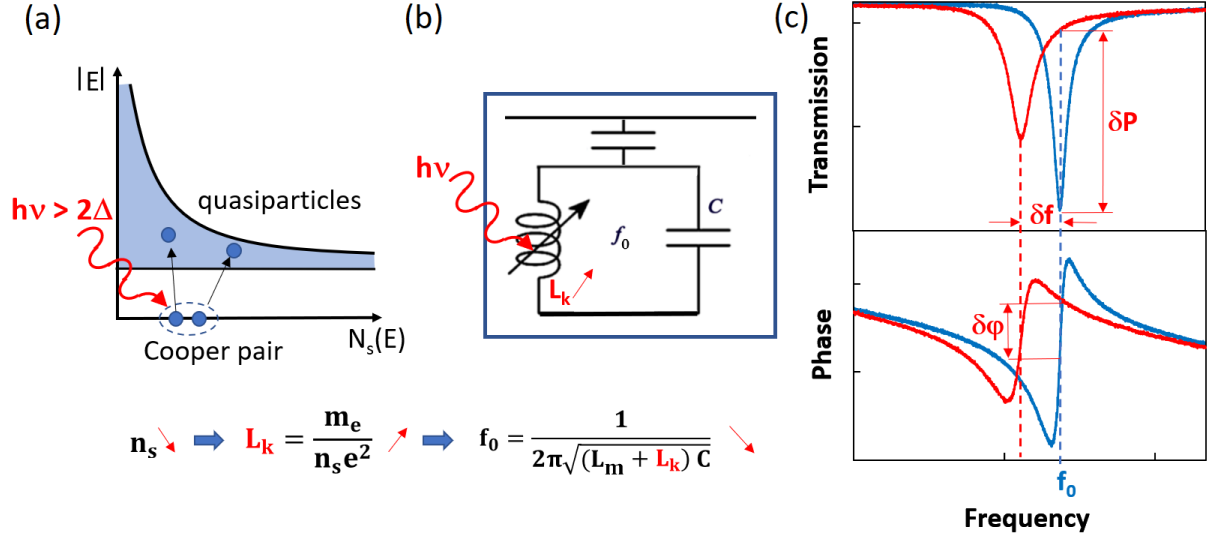
Figure 2.6: Illustration of the basic principle of MKID detection. (a) An incoming photon of energy $h\nu > 2\Delta$ can break Cooper pairs into an excited quasiparticle state that will (b) change the kinetic inductance of the RLC resonator which (c) translates into a frequency and phase shift.

2.8.1 Two-port representation

As shown in Fig. 2.7, an MKID can be represented as a two-port network with a load Z_{MKID} on a transmission line with a characteristic impedance Z_0. The scattering parameters are a mathematical construct that quantifies the distribution of energy through a multi-port network. Each port has a reflection and transmission scattering parameter that can be extracted by the electronics detailed in Sec. 3.7.
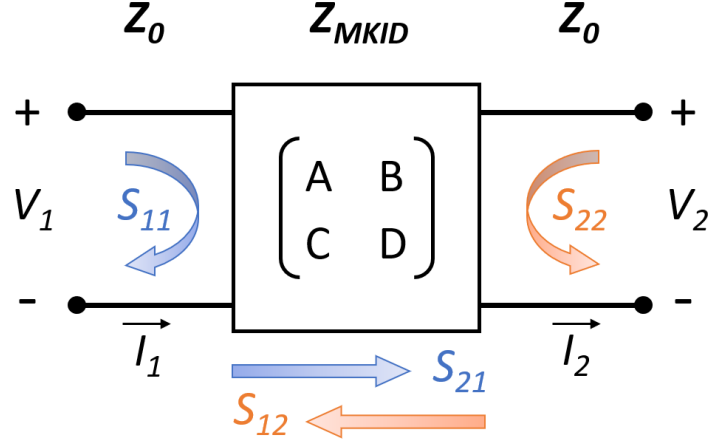
Figure 2.7: Two-port representation of an MKID resonator and the corresponding scattering parameters.

For a 2-port network, a 2×2 ABCD matrix is enough to describe the nature of the load such as:

$$\begin{pmatrix} V_1 \\ I_1 \end{pmatrix} = \begin{pmatrix} A & B \\ C & D \end{pmatrix} \begin{pmatrix} V_2 \\ I_2 \end{pmatrix} \tag{2.33}$$

where V_1, I_1 and V_2, I_2 are respectively the voltage and current at port 1 and 2. In the case of a lumped element MKID, we can consider the load to be connected to the transmission line as a series impedance which translates to:

$$\begin{pmatrix} A & B \\ C & D \end{pmatrix} = \begin{pmatrix} 1 & Z_{\mathrm{MKID}} \\ 0 & 1 \end{pmatrix} \tag{2.34}$$

The scattering parameter commonly used to read an MKID is the forward transmission parameter S_{21} from port 1 towards port 2 which can be expressed from Eq. 2.33 and 2.34 as:

$$S_{21} = \frac{2}{A + B/Z_0 + C Z_0 + D} = \frac{2}{2 + Z_{\mathrm{MKID}}/Z_0} \tag{2.35}$$

28

2.8.2 Multiplexing

The resonance frequency f_0 in equation 2.24 is defined by the values of L and C which depend on many parameters such as the material, film thickness but also the geometry. The advantage of using localized elements for multiplexing is that we can modify the capacitor geometry without affecting the inductive absorber part. To do so, we remove portions of the capacitor's fingers so that each RLC circuit has a unique f_0 as demonstrated in Fig. 2.8 that we usually represent as the magnitude of the forward scattering parameter $10 \log S_{21}$ in decibels (dB).
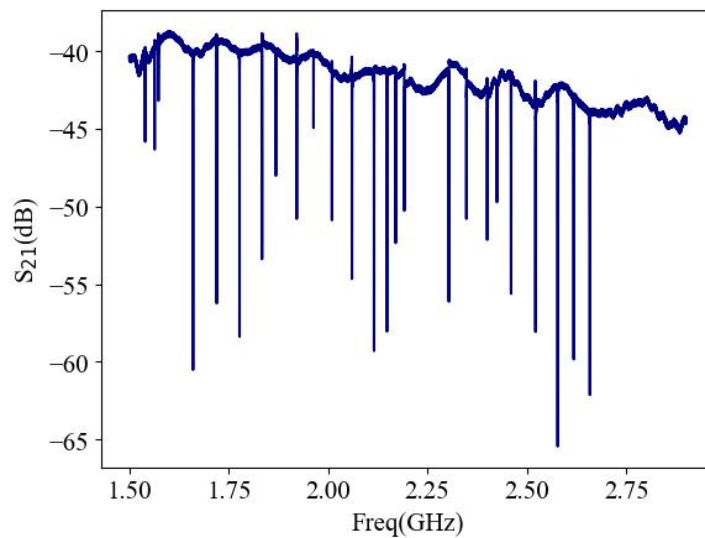
Figure 2.8: Magnitude of the S_{21} parameter at 50 mK measured on a 25-pixel reference sample on which photon counting was observed. Each dip corresponds to the resonance frequency of one pixel that acts as a band-stop filter. If a photon event is recorded on one pixel, only the corresponding dip will be affected. For this sample, there are no spectral collisions as we can identify all 25 resonances.

The frequency step between two consecutive resonances must be large enough to avoid collisions which would render pixel identification impossible. In kilopixels arrays, the gradient in film homogeneity or defects in the fabrication process make collisions very probable so we try to space them out as much as possible while staying in the frequency band imposed by the readout electronics.

2.8.3 Coupling to the transmission line

In order to operate, the RLC circuits needs to be coupled to a transmission line that has two purposes. It first acts as a feedline in which a frequency comb is sent to excite all the resonators so that each one of them will be affected by the frequency that corresponds to its f_0. The second purpose is to simultaneously read the resonators since the RLC circuits at their f_0 act as a short to ground and every transmission dip spectrally resolved on the line can be extracted from the S-parameters. Fig. 2.9 is a schematic illustration of the different elements of the resonator and how they are coupled to both the feedline center strip and ground planes.
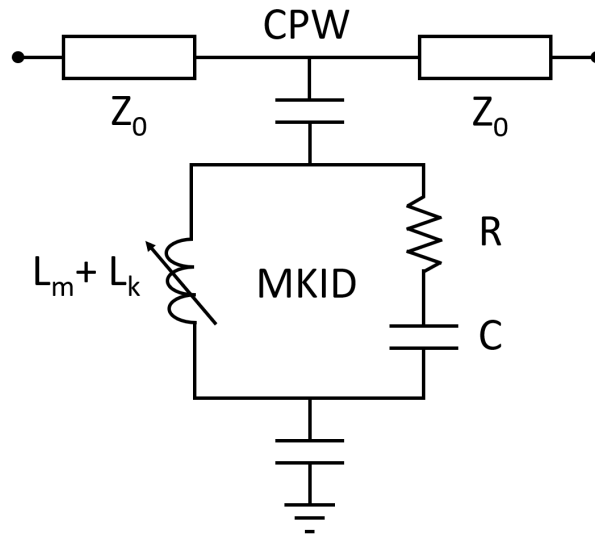
Figure 2.9: Schematic representation of an MKID LC resonator with a resistance that is quasiparticle dependant. A CPW feedline with characteristic impedance Z_0 is capacitively coupled to the resonator and the mean of detection comes from the change of kinetic inductance that modifies the MKID resonance frequency.

The advantage of using a single transmission line for thousands of pixels is that it can reduce noise and readout electronics complexity. However, the whole array is prone to fail if the line is either open or shorted during fabrication. The transmission line we use is a Coplanar Wave Guide (CPW) that consists of a center conducting stripline with ground planes on each side. The CPW allows for impedance matching at $Z_0 = 50\ \Omega$ with a compact design in opposition to the more common microstrip geometry that would be as wide as the pixel size, which is not fitting for kilopixels arrays. The main mode

in CPW is quasi-TEM which corresponds to the electric field and magnetic field to be perpendicular to one another and also perpendicular to the direction of propagation. The mode propagating inside the center strip is not pure TEM because of the medium asymmetry between the dielectric below the line and the free-space above it. Since the CPW is quasi-TEM, the coupling to the resonators can be either capacitive or inductive. In our case, it is always capacitive and is quantified by the coupling quality factor Q_c related to Q_i by:

$$\frac{1}{Q} = \frac{1}{Q_c} + \frac{1}{Q_i} \tag{2.36}$$

where Q is the resonator total quality factor. Unlike Q_i that is mainly fabrication dependant, Q_c can be tuned by geometry parameters such as the distance between the CPW and resonator, the area of coupling or the resonator geometry. In the visible to NIR range, the size of the resonator's inductance is usually much smaller than that of the capacitor so we favor a capacitive coupling. The quality factors can be rapidly estimated following the method shown in Fig. 2.10 by measuring the resonance bandwidth at half power which is 3 dB below the baseline for Q_c and 3 dB above the dip for Q_i.
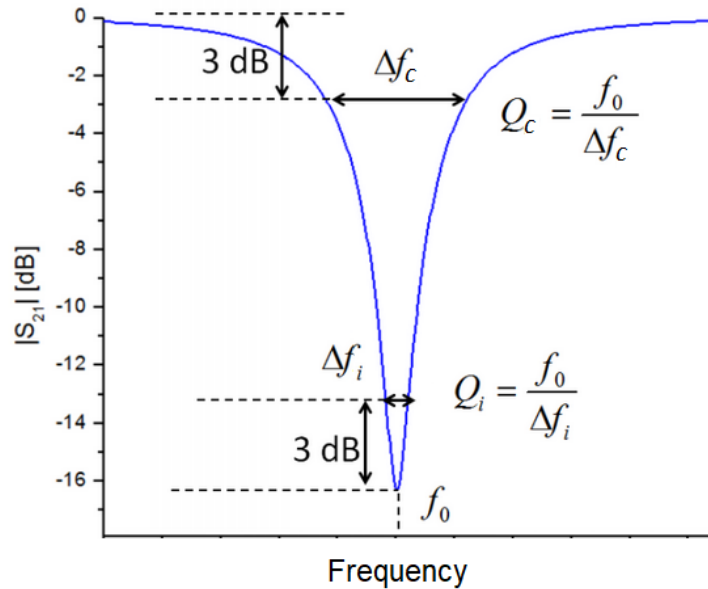
Figure 2.10: Illustration of the method to estimate the MKID quality factors using the transmission resonance dip.

In order to keep Q_i relatively high to be able to read a resonance even after the increased

loss caused by a photon event, we try to limit Q_c below 100,000. Q_c should not be designed to be too low either because it would make the resonance depth extremely steep which would also cause difficulties in the electronic reading.

2.9 MKIDs sensitivity

The theoretical limiting energy resolving power of an MKID operating in single-photon mode is known as the Fano limit and can be expressed as [50]:

$$R_{\text{Fano}} = \frac{1}{2\sqrt{\ln 2}} \sqrt{\frac{\eta_{\text{qp}} h\nu}{F_{\text{Fano}} \Delta(T)}} \tag{2.37}$$

where the Fano factor $F_{\text{Fano}} = 0.2$ for most superconductors [51] and is inversely proportional to energy resolution. The theoretical value of R_{Fano} in Eq. 2.37 for low T_c materials would thus be between 60 and 100 for the Vis-NIR range but the current R achieved by the different groups varies between 10 and 30 [11, 13]. This resolving power seems to be partially limited by TLS noise even though there are a few different noise sources to consider which are detailed below. The usual way to define the sensitivity of any detector is given by measuring for each noise source detailed below the Noise-Equivalent Power (NEP) that can be defined as the input power in a system that will be doubled at the output. The different noise sources Power Spectral Density (PSD) can be measured experimentally using a signal generator and plotted as a noise spectrum represented in Fig. 2.11.
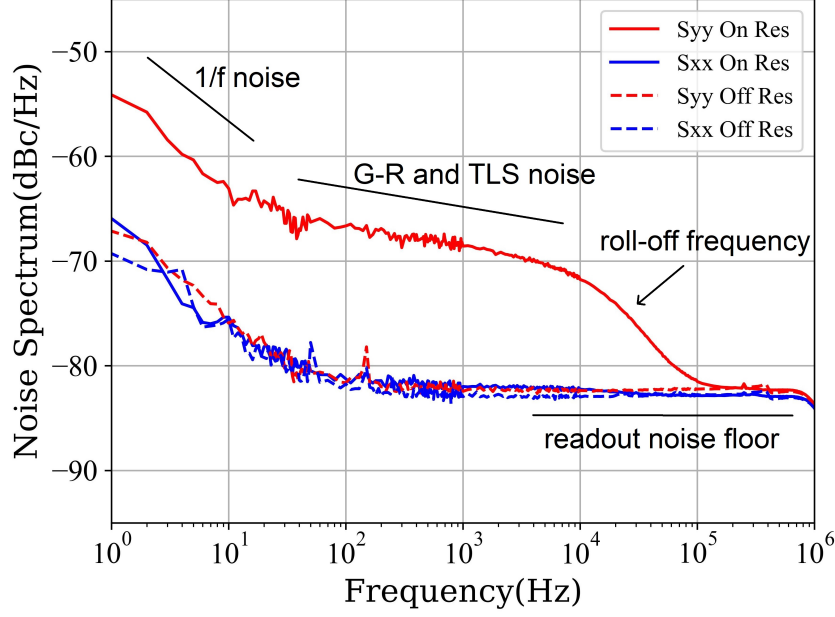
Figure 2.11: Typical PSD of an MKID on and off resonance normalized by the square of the resonance frequency. S_{xx} and S_{yy} correspond respectively to the amplitude and phase noise of the resonator measured relative to the generated signal in dBc/Hz. From 0 to 50 Hz, the $1/f$ noise is dominant on and off resonance in both noise components. From 50 Hz onwards, S_{xx} on resonance is only affected by the readout noise so it is usually not regarded to study the noise in MKIDs. In S_{yy}, the TLS noise is responsible for the $f^{-1/2}$ slope from 50 Hz to 10 kHz and the generation-recombination noise also has an influence until the roll-off frequency reciprocal to the resonator response time at 50 kHz where readout noise becomes the noise floor.

2.9.1 Photon noise

Photon noise does not come from the detector limitations but rather from the statistical properties of photons. The rate at which photons from a light source hit the detector follows a Poisson distribution and the photon event probability is defined as:

$$P(n) = \frac{N_{ph}^n}{n!} \exp(-N_{ph}) \tag{2.38}$$

where N_{ph} is the mean number of photons received and n is the photon occupation number per mode. The standard deviation of the distribution in the case of visible photons ($n \ll 1$) is equal to $\sqrt{N_{ph}}$. If we still consider visible photons, the NEP of photons can

be approximated as [52]:

$$\mathrm{NEP}_{\mathrm{photon}} = \sqrt{\frac{2P_{\mathrm{opt}}h\nu}{\eta_{\mathrm{qe}}}} \tag{2.39}$$

where P_{opt} is the optical illumination power and η_{qe} is the detector quantum efficiency. The reported NEP varies between 10^{-17} and 10^{-16} W·Hz$^{-1/2}$ [53, 54]. The combined NEP of every intrinsic noise source in an ideal MKID should be lower than this value.

2.9.2 Readout noise

The measurement readout noise is the only source of white noise in MKIDs and is limited by the cryogenic amplifier so we use a Low-Noise Amplifier (LNA) at the 4 K stage to limit thermal noise. Readout noise constitutes the noise floor at high frequencies but should not be considered as a limiting factor in MKIDs sensitivity. The readout noise PSD can be expressed as:

$$S_{read} = \frac{4Q_c^2 k_B T}{Q^2 P_{read}} \tag{2.40}$$

where P_{read} is the MKIDs readout power. In the case of $Q_i \ll Q_c$, the readout noise contribution would be too important so it is necessary to design and fabricate resonators that have a Q_i that is at least equal or higher than Q_c. Readout noise should generally be kept below -80 dBc/Hz as seen in Fig. 2.11.

2.9.3 1/f noise

$1/f$ noise is a noise source present in any electronic device and whose PSD is inversely proportional to frequency. It is thus the dominant noise source at low frequencies up to the $1/f$ corner that has been measured at 50 Hz in our devices.

2.9.4 Two-Level System noise

The Two-Level System (TLS) noise is known for being the main source of frequency noise in MKIDs and more generally across various superconducting technologies where the most flourishing field is quantum computing [55]. Yet, the behaviour of TLS is still

the subject of many investigations with no unifying microscopic theory available to date. As represented in Fig. 2.12, TLS is the result of quantum tunneling of particles between two distinct energy levels $\Delta E = E_2 - E_1$ separated by a potential barrier V that can be crossed below a certain temperature with a tunneling energy Δ_0.
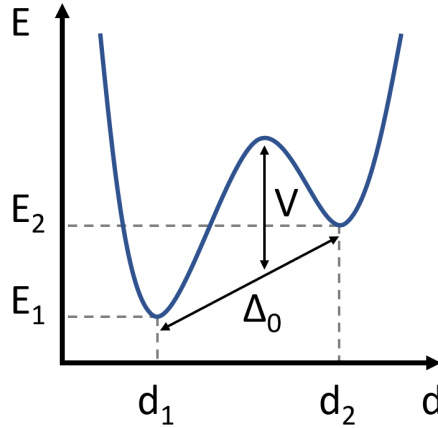
Figure 2.12: Representation of the double-well potential responsible for TLS in amorphous materials. At very low temperatures and weak electric field, a particle with energy Δ_0 can tunnel between two minima separated by $\Delta E = E_2 - E_1$ that randomly modifies the dielectric constant and increase the fractional frequency noise in Eq. 2.41

TLS is mostly observed in the bulk of amorphous substrates or at the interface between thin-film layers in the form of a nanometer-thick TLS-hosting layer. To minimize the TLS contribution, our thin films are deposited on very low dielectric loss sapphire substrates and undergo a drastic wet cleaning process as described in Sec. 3.1 as well as a RF plasma cleaning before deposition. The TLS influence on the MKIDs response can be described as the random variation of the dielectric constant that directly modifies the f_0 of a resonator without any photon event. The closest and most accurate model to date is as follows [56]:

$$\frac{f_0 - f}{f} = \frac{F_{\text{TLS}}\delta_0}{\pi} \left\{ \Re\left[\Psi\left(\frac{1}{2} + \frac{1}{2i\pi}\frac{\hbar\omega}{k_B T} \right) \right] - \ln\frac{\hbar\omega}{k_B T} \right\} \qquad (2.41)$$

where the TLS filling factor F_{TLS} is the fraction of the electric field energy in the volume that hosts TLS and Ψ is the complex digamma function. δ_0 is the TLS-induced dielectric

loss tangent in the $k_B T = 0$ limit for a weak non-saturating field. The generalized TLS contribution to dielectric loss can be expressed as:

$$\delta_{\text{TLS}} = \delta_0 \tanh\left(\frac{\hbar\omega}{2k_B T}\right) \tag{2.42}$$

From Fig. 2.12 and Eq 2.41, we can conclude that higher bath temperatures will increase the particles energy $k_B T$ up to a point where there is no more potential barrier between the two energy states. For example, in quantum computing, each qubit is actually a TLS with known resonance frequency that can couple with unwanted TLS with energy lower than $k_B T$ and create random fluctuations in the qubit [57]. Below a certain turning point that varies depending on the film properties, TLS becomes increasingly dominant and is responsible for a large transient and dissipationless pulse response in MKIDs that will be detailed in Sec. 5.1. In the case of superconducting microresonators such as MKIDs, the dielectric loss tangent δ_{TLS} in Eq. 2.42 is inversely proportional to the resonator internal quality factor Q_i [58].

Another way to look at TLS is through the PSD given by [43]:

$$S_{\text{TLS}}(f) = k(f, \omega, T) \frac{\displaystyle\int_{V_{\text{TLS}}} |\vec{E}(r)|^3 \mathrm{d}^3 r}{4\left(\displaystyle\int_{V_{\text{tot}}} \epsilon(r)|\vec{E}(r)|^2 \mathrm{d}^3 r\right)^2} \tag{2.43}$$

where $k(f_0, f, T)$ is the noise spectral density coefficient responsible for the $f^{-\frac{1}{2}}$ slope in Fig. 2.11. We can also project the TLS on the phase noise as a function of resonator quality factors:

$$S_{\text{TLS}}(f) = S_{yy}(f) \frac{Q_c^2}{4Q^4} \tag{2.44}$$

In order to minimize TLS, it is crucial to keep in mind during the MKID design and fabrication process that all efforts should go towards obtaining a high total Q. The previous Eq. 2.43 describes the ratio of electric energy stored in V_{TLS} the region contributing to TLS to the total electric energy in the resonator volume V_{tot}. The noise contribution from V_{TLS} can be minimized by scaling down the capacitor size or by increasing readout power

to saturate the TLS. Most of the particles will be forced to occupy an excited state which will prevent energy state tunneling.

2.9.5 Quasiparticles generation-recombination noise

MKIDs suffer from a dark current noise that involves quasiparticles called Generation-Recombination (G-R) noise. At normal operating temperature and in the dark, there is still enough heat to cause random variations in the number of quasiparticles that have enough energy to break Cooper pairs. The spectral influence of G-R noise is mainly observed between the $1/f$ noise and the roll-off frequency of the recombination bandwidth $f_0/2\pi\tau_{qp}$. The PSD of thermally excited quasiparticles can be expressed as:

$$S_{N_{qp}}(f) = \frac{4N_{qp}\tau_{qp}}{1 + (2\pi f\tau_{qp})^2} \tag{2.45}$$

From Eq. 2.13 and 2.45, we observe a temperature dependence of G-R noise in $\exp(-1/k_BT)$ that decreases exponentially with decreasing temperature. The associated NEP can be written as:

$$\text{NEP}_{G-R} = \frac{2\Delta}{\eta}\sqrt{\frac{N_{qp}}{\tau_{qp}}} \tag{2.46}$$

At the normal MKIDs operating temperature, the G-R NEP is reported to be around $\text{NEP}_{G-R} \approx 10^{-19}$ W·Hz$^{-\frac{1}{2}}$ [59]

Chapter 3

MKIDs fabrication and measurements process

The fabrication process is the most critical part of my work towards developing a new MKID geometry. If overlooked, the internal quality factor of the resonators can greatly decrease, making characterization impossible. At Paris Observatory, we have a dedicated cleanroom for better control over each step of fabrication. This facility gathers all equipment needed for the fabrication of MKIDs in an environment where the concentration of microscopic particles is controlled to minimize wafer contamination. Under the classification of cleanrooms (ISO 14644-1), the Paris Observatory facility is class ISO 7 ($<$10 000 particles/ft^3 under 0.5µm) with fume hoods class ISO 5 ($<$100 particles/ft^3 under 0.5µm).

3.1   Sapphire wafer cleaning

Before starting the photolithography process, it is necessary to remove contamination from the wafer. All our devices are deposited onto sapphire substrates that offers a high dielectric constant compared to quartz and do not suffer from undesirable substrate modes like in high-resistivity silicon substrates. The cleaning process we use for a sapphire wafer is based on the silicon cleaning process developped at SRON and has allowed for high quality factors in our previous works. If this crucial step is overlooked, the organic, particulate and metallic contaminants at the substrate surface can greatly affect the thin-film

layer deposition [60]. In that case, the internal quality factor of the MKIDs can be greatly affected and the increase of TLS noise can lead to no resonance.

The first step is to degrease the surface using wet cleaning. The wafer is immersed in a mixture containing half deionized water, half *RBS 25 Concentrate* detergent. The beaker is then placed in a heated water bath with ultrasonic waves for ten minutes to degrease the surface more effectively. This exact process is then repeated respectively with a beaker full of aceton and one with isopropanol. The next step is to remove carbonate residues using reactive-ion etching (RIE). An oxygen plasma is generated inside a vacuum chamber to burn these residues on the wafer surface. The wafer is then soaked inside an acid solution called Piranha to remove the burnt organic contaminants. After 10 minutes, we place the wafer in deionized water before rinsing it. This step is repeated after each acid cleaning. The different wet cleaning solutions used throughout the cleaning process are detailed in Table A.1.

We then use a basic solution called Standard Clean 1 (SC1) to eliminate inorganic particles. The various cleaning are bound to leave oxidation layers that will later on generate TLS noise. For this reason, we end the cleaning process with Hydrogen Fluoride (HF) diluted in water to remove these unwanted layers and passivate the surface to make it hydrophobic. The wafer is finally heated on a hot plate at 110°C for one minute to evaporate any remaining water particule.

3.2   Photolithography

In order to quickly pattern the microwave circuits with patterns size down to 0.7 µm as demonstrated in Fig. 3.2, all the arrays in this work were fabricated using photolithography. Even though MKIDs were first praised for their ease of fabrication, the designs in this work will usually need more than two different layers. The whole process described below is thus repeated multiple times where each run focuses on all features made from the same material. It is recommended to pattern and deposit the TiN resonators in the first run right after wafer decontamination to ensure the highest Q_i possible but some designs here did not allow it and yet excellent Q_i were measured.

3.2.1 By Lift-off
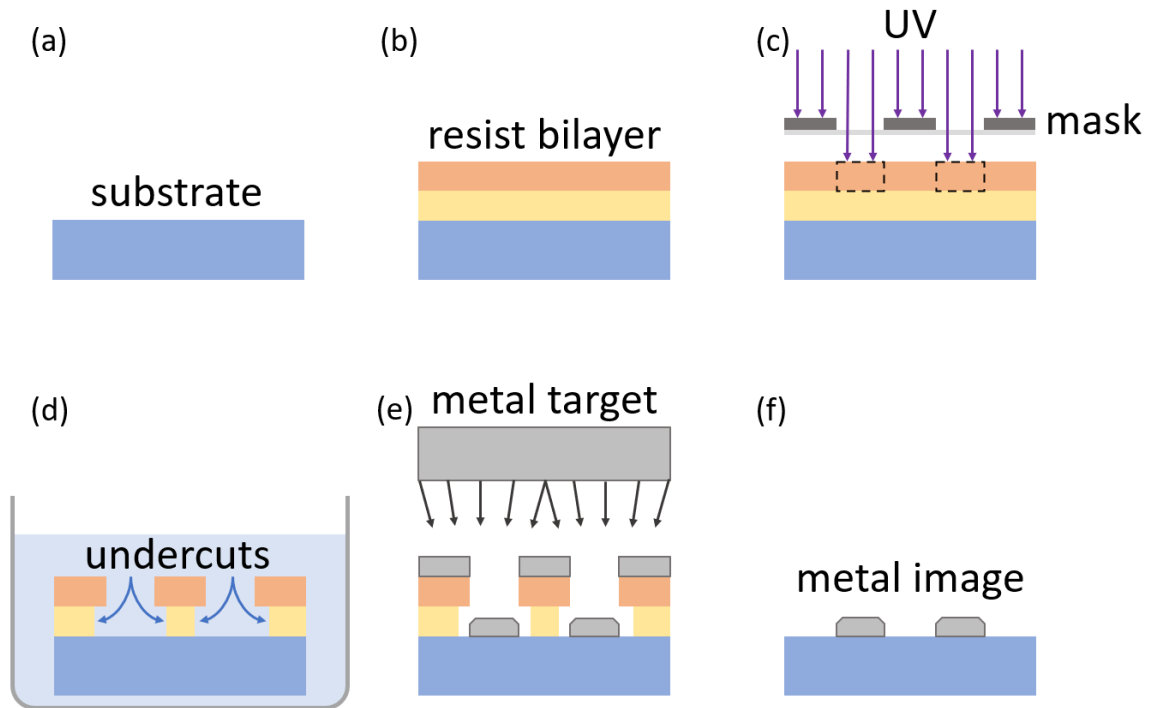
Figure 3.1: (a) A cleaned substrate is (b) spin-coated with a bilayer of resist. (c) The desired image is transferred by illuminating a photomask with UV light so that (d) the exposed resist can be dissolved by wet development. (e) A metal is sputtered and (f) only the desired structures will stay on the wafer once the remaining resist is dissolved in aceton.

In the case of metal deposition detailed in Sec. 3.3.1 and 3.3.2, the process used is photolithography by lift-off. The first step is to spin coat the wafer with a UV-sensitive viscous resin called photoresist or simply resist. The wafer is held in place on a vacuumed rotating platform that spins at high velocity to homogeneously coat the resist. Since the metal deposition is isotropic, it is important to have a steep resist profile so we use a bilayer where a less sensitive resist is spin-coated on top of a more sensitive one. This way, we can create a T-shape profile known as undercuts during the development process that greatly reduces sidewalls deposition. The under layer of resist we employ is called *LOR 1A* which is recommended for patterning features with a resolution down to 0.5 µm. The top resist used in combination with the *LOR 1A* is a positive resist called *SPR 700*. Additionally for the first run, we spin-coat the wafer with an adhesion promoter called hexamethyldisilazane (HMDS) prior to the bilayer. This allow for an hydrophobic surface

that prevents the aqueous base to slip through the resist bilayer during development and lift unwanted parts of the thinner structures. The wafer is finally prebaked on a hotplate to evaporate solvents and harden the resist. The next step is to define the microwave circuit structures inside the resist. The positive resists we use are microscopically composed of long polymer chains that can be ruptured if exposed to UV light. This photochemical reaction will render the exposed resin soluble for later removal during the development process. In order to illuminate only certain parts of the resist, we use a photomask in low-vacuum contact with the wafer that will allow to print the image of the features onto the resist with a resolution that is diffraction-limited. Depending on the size of the features, we can use different spectral lines of our mercury lamp. In the case of features larger than 1 µm, we use the I-line (365 nm). For features down to 0.7 µm, an additional optical low-pass filter with a cutoff wavelength at 340 nm is necessary to increase the resolution.
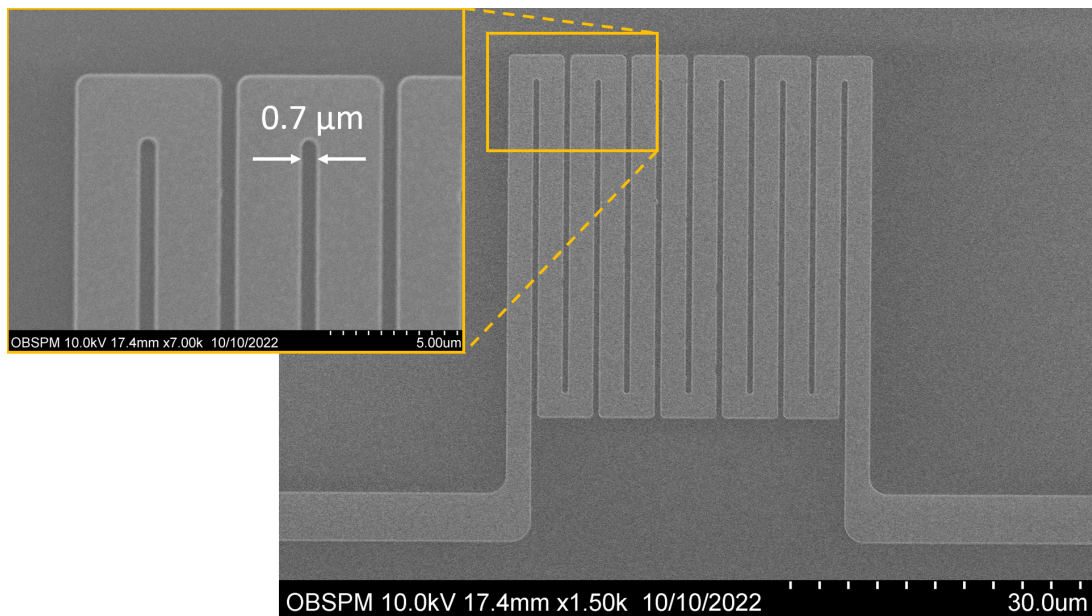
Figure 3.2: Image of an inductive meander taken with a Scanning Electron Microscope (SEM). The photolithographic technique allows us to pattern elements with a resolution down to 0.7 µm as seen here with the meander gaps.

For the first run, the image can be simply printed onto the resist but for the following runs, we need to align the new features to the already existing ones with a mask aligner that typically offers an alignment precision of 1 µm. To help with alignement, we usually define crosses at every corner of the photomask that we superpose with the crosses previously

deposited on the wafer by adjusting translation and rotation. The resist will become more transparent during exposition which helps the UV light to penetrate in depth and react more efficiently with the polymers. Once the resist has been exposed to UV light long enough, the wafer undergoes a post-exposition bake to boost the photoreaction. Finally, we proceed to the wet development of the exposed resist to complete the image transfer from the mask to the resist. The wafer is immersed in a base solution which dissolves the exposed resist at a rate that is pH and temperature dependant. Once the top layer of the resist bilayer has been removed, the solution will dissolve the bottom layer that is not photosensitive. This way, the base will also penetrate over a small distance below the top layer of the resist that has not been exposed to light and create undercuts. After deposition, the remaining resist is dissolved in an aceton bath so that only the metal image in contact with the wafer remains.

3.2.2 By Etching
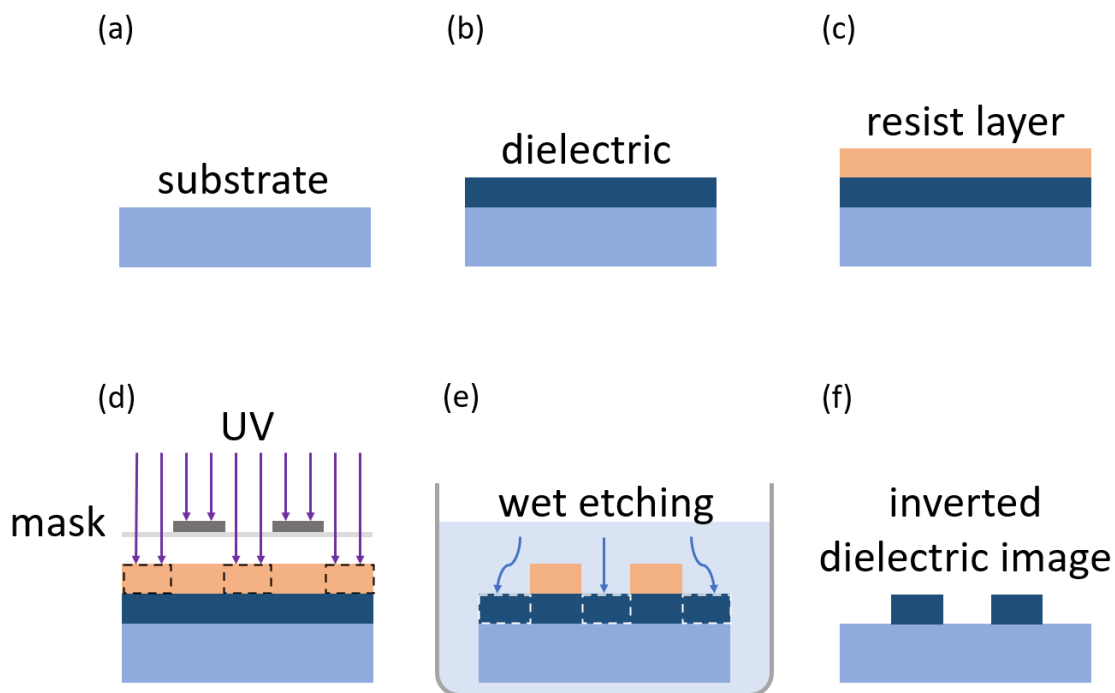
Figure 3.3: (a) On a clean substrate, (b) a dielectric is deposited using Atomic Layer Deposition (ALD). (c) A single resist layer is spin-coated and (d) the undesired structures are exposed to UV light. (e) Once the resist has been developed, the unwanted parts of the dielectric are removed by wet etching and (f) the resulting dielectric image is inverted compared to the photomask.

In the case of dielectric deposition detailed in Sec. 3.3.3, the resist cannot withstand a deposition of several hours at temperatures close to 200°C hence the lithography process comes after deposition. Once the dielectric layer is deposited directly on the whole wafer, a resist image is created on top of it in the same fashion as for lift-off but is inverted to cover all the elements we want to protect from etching. There is no need for a resist bilayer because wet etching creates smooth profiles. Once the inverted resist image is developed, the wafer is immersed again in a developer to start the wet etching process that will remove the exposed dielectric parts at a rate of around 2 nm/minute. Since we use wet etching, the aqueous base can create undercuts which is not critical in our design but we still make sure that our structures are a bit larger than expected to compensate.

3.3 Deposition techniques

In this work, all metals were deposited by Physical Vapor Deposition (PVD) and dielectrics by Chemical Vapor Deposition (CVD). The PVD process used are magnetron sputtering and thermal evaporation and the CVD process used is Atomic Layer Deposition (ALD), all of which are detailed in the following sections.

3.3.1 Magnetron sputtering

PVD allows for a fast deposition and good step coverage necessary for our designs. The main PVD technique used in this work for Nb, Al and TiN is called sputtering. The wafer is inserted inside a high-vacuum chamber (10^{-8} mbar) through a load-lock to greatly reduce the pumping time after chamber insertion. Above the wafer is a cylinder of the material we want to deposit called a target. An inert gas like argon is fed into the chamber at a rate measured in Standard Cubic Centimeters per Minute (sccm). A direct current is applied and with enough power, electrons from the target will ionize the gas into a plasma state. The positively charged ions will be attracted and accelerated towards the negatively charged target and with enough velocity, they can transfer their momentum to eject atoms out of the target. The electric potential between the target and the wafer will force these atoms to be deposited onto the substrate at a rate that is on the order of a nanometer each second. Additionally, the argon ions can also eject electrons out of the target that will replenish the plasma by ionizing other argon atoms. To help boost

the reaction and also prevent unnecessarily overheating the wafer and damage the resist image, we use magnetron sputtering where a magnetic field will confine the plasma near the target. A water-cooling system runs below the sample holder to further reduce the wafer's temperature during sputtering. For the case of TiN, we use reactive sputtering where the atoms ejected out of the Ti target by the argon plasma will directly react with a N_2 gas fed into the chamber. By tuning the rate of the nitrogen flow, one can achieve different TiN_x crystalline structures and effectively change the material's T_c. A stoechiometric TiN film ($T_c = 4.6$ K) is not sensitive enough by itself to count photons and a pure Ti film ($T_c = 0.4$ K) cannot be cooled down by our cryostat below $T_c/10$ to ensure $\frac{n_s}{n}$ close to 1. For the range between these two film compositions, a small change in the nitrogen flow rapidly modifies the T_c of the TiN_x film as seen from the steep blue curve in Fig. 3.5. Local changes of nitrogen density inside the chamber during sputtering greatly limit homogeneity for large arrays. The resulting T_c can be really unstable from one batch to another and TiN has been set aside by several groups to focus on other material alternatives such as platinum silicide or hafnium which also come with their sets of challenges [61, 62]. During my thesis work, we chose to persevere with titanium nitride and demonstrated high Q_i TiN_x-based MKIDs with sufficient T_c reproductibility thanks to intense characterization.
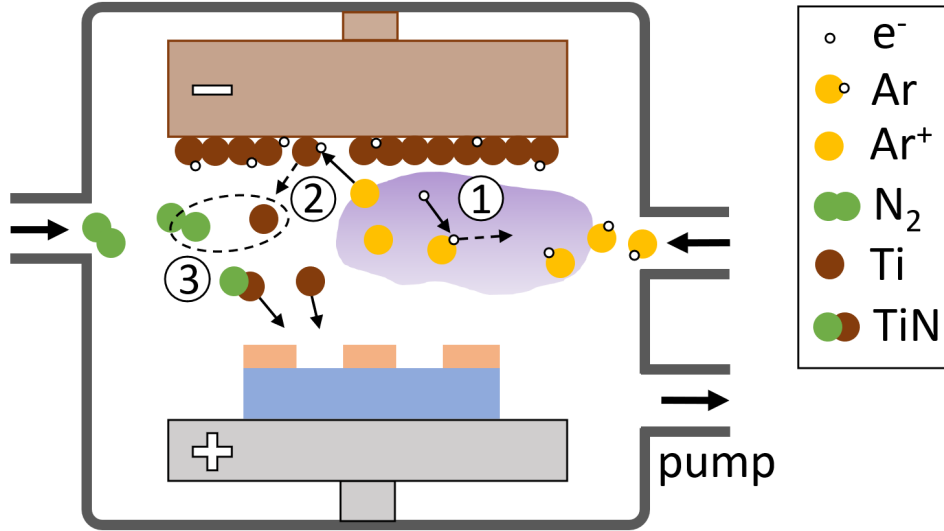
Figure 3.4: Reactive sputtering of TiN: (1) An argon gas fed into the chamber is ionized by electrons from the titanium target and creates a plasma (in purple) kept close to the target thanks to the magnetron. (2) The argon ions are accelerated towards the target and eject titanium atoms outwards where (3) they may or may not react with the nitrogen flow to form a sub-stoichiometric TiN_x film.

3.3.2 Thermal evaporation

The only metal that is not sputtered during this work is gold because it can easily contaminate other targets in the sputtering chamber so instead we use another PVD technique called thermal evaporation. Inside a vacuum chamber, some pieces of solid gold are placed inside a highly refractory recipient called a crucible and the wafer is placed above it facing down. A high current is applied to a tungsten filament that will heat the crucible through resistive heating and will sublime gold at the right temperature. Before depositing, we cover the wafer and proceed to a first run of sublimation that will remove impurities from the crucible without polluting the wafer. For the second run, the cover is removed and the heated gold will evaporate upwards onto the wafer and deposit at a rate on the order of a few nanometers per second. Since thermal evaporation has a poor film adhesion to the substrate, we first deposit a 5 nm thick Ti layer by using a second crucible inside the chamber. We previously used resistive heating to deposit silicon monoxide (SiO) but was abandoned for the lack of control over the thickness and the poor film purity that

eventually affected our resonators quality factors.

3.3.3 Atomic Layer Deposition

A strong alternative to SiO with a higher refractive index is aluminium oxide (Al_2O_3) that can be deposited from the vapor phase using ALD. The conformality on high-aspect ratio structures that ALD offers is required to cover the 100 nm step in the optical stack MKID design. The deposition of successive atomic layers makes the dielectric film more compact which reduce its loss tangent and thus TLS noise. ALD consists in sending sequential pulses of gas called precursors on a wafer inside a vacuum chamber in the right pressure and temperature range to prevent the precursors unwanted condensation or desorption. The precursors used for growing Al_2O_3 are water (H_2O) and trimethylaluminium ($Al(CH_3)_3$) abbreviated as TMA. Initially, the substrate is already hydroxilated, meaning that its surface is terminated with OH groups ready to react with a precursor. TMA is first pulsed inside the chamber and each molecule will form an Al-O bond with one hydroxile by losing a CH_4 group. This self-limiting process will saturate the surface with a Al-CH_3 monolayer and any excess TMA can be purged along with the CH_4 by-product. Water is then pulsed inside the chamber and react with the monolayer to form an Al-O-Al bridge by once again releasing a CH_4 gas. The reaction also renews an hydroxile coating on the surface and the cycle ends with a second purge. One cycle is the combination of all these successive pulse and purge steps to grow an Al_2O_3 monolayer with a thickness of around one angstrom.

3.4 TiN deposition parameters

Titanium Nitride is chosen as the sensitive part of our MKIDs mainly because of its high film resistivity and low T_c that increase sensitivity from L_k defined in Eq. 2.21. The deposition of the MKIDs TiN_x absorber is the most critical step amongst all film growths because it uses reactive sputtering represented in Fig. 3.4 to make a N_2-Ar gas react with a Ti target. The ratio of N_2:Ar inside the chamber will change the crystallographic nature of the film which results in a tunable T_c. Since we have set the Ar gas flow to 50 sccm in all of our sputtered film growths, we will only refer to the N_2 flow in our measurements. In order to achieve single-photon detection, the Cooper pairs in TiN_x film should have a

low enough $\Delta(0)$ while maintaining a sufficiently high n_s/n ratio limited by the cryostat cooling ability. A compromise should also be found between the film resistivity and its total kinetic inductance. From all these constraints, we decided to aim for a $T_c = 2$ K that corresponds to a 4.9 sccm N_2 flow which is located right in the steep transition phase. The first issue is that the N_2 flow feedback sensor we use has a $\pm$ 0.1 sccm uncertainty which translates into a large $\pm$ 3 K uncertainty in the film T_c and affects reproducibility. The other issue is that sub-stoichiometric TiN in reactive sputtering is known for its lack of homogeneity regardless of the film thickness caused by small local changes in the N_2:Ar gas ratio inside the chamber, making it difficult to obtain a constant L_k over the whole wafer needed for kilopixels arrays [63].
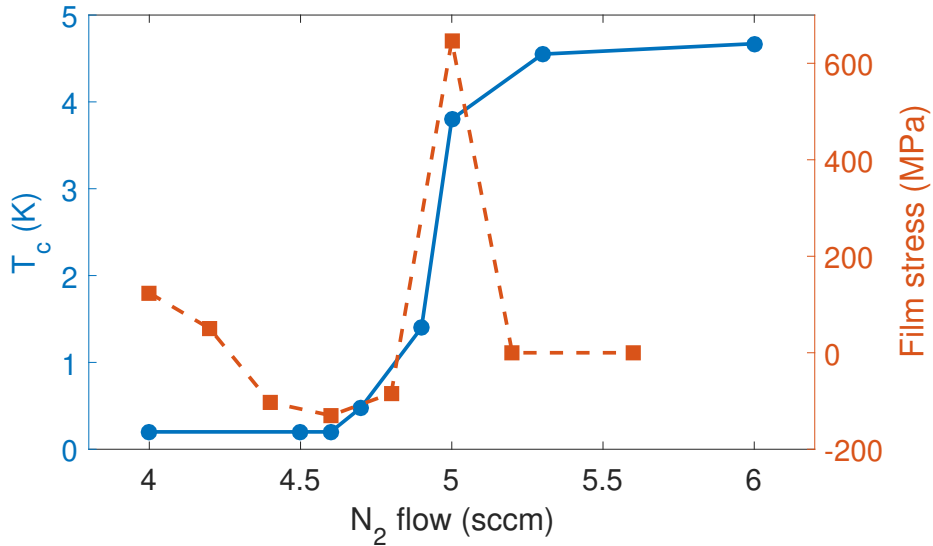
Figure 3.5: Measurements of the TiN_x film T_c and stress at room temperature as a function of nitrogen flow. The films were deposited by reactive sputtering with a constant argon flow of 50 sccm, DC power $P_{DC} = 700$ W and pressure $P_r = 0.6$ Pa. The T_c transition before the stoichiometric state is very abrubt and corresponds to the T_c region we are aiming with a 4.9 sccm N_2 flow. To greatly reduce characterization time from cooling down samples and determine their T_c, we can quickly deduce the T_c at room temperature by comparing the stress induced on the substrate before and after deposition represented by the dashed curve.

Fortunately, we are able to deduce the film T_c directly from the film stress parameter with good accuracy [64]. This allows for a room-temperature T_c estimation of a plain

film instead of having to pattern a feedline and cool down the sample to determine its T_c, which saves roughly two days per data point in Fig. 3.5. Some TiN parameters can also drift over time so a fast regular re-characterization is now possible. The first step is to measure the curvature of a substrate in at least two defined orthogonal directions using a mechanical profilometer. We do the same measurement on the substrate after deposition of a TiN_x layer with a known thickness to extract the film stress and we repeat this process for different N_2 flow. The dashed curve in Fig. 3.5 shows a strong dependence between TiN_x sub-stoichiometric state and film stress where the TiN_x crystal structure changes rapidly from one orientation to another. Since we had not yet characterized sub-stoichiometric TiN_x at the beginning of this work, most of the samples fabricated and measured in the next chapters were made of stoichiometric TiN with a 6 sccm N_2 flow. These kind of films were not sensitive enough for single-photon detection but allowed us to unexpectedly study a novel TLS-related phenomenon.

3.5   Device dicing and mounting

Once that all the desired thin layer structures are deposited on the wafer, we proceed to wafer dicing. We usually define four individual arrays on a 2-inch wafer for one of the following two reasons: we can either pattern up to four different geometries with the same deposited layer or we can ensure backup arrays that are identical in the case of a critical fabrication defect on one of them. With the several layers needed for some designs and the experience I gained over the years in the cleanroom, I have learned to favour the latter. The wafer surface has been coated with a thick layer of resist to prevent particle contamination and is diced into squares using a mechanical dicing saw that rotates at high speed and is cooled down with pressurized deionized water. The backside of the wafer is sticked to a special tape resistant to dicing which also hold the wafer in place inside the machine. The dicing tape will prevent the small 1×1 cm^2 dies to freely move during the process and also makes it easier for storage purposes later on. One of the four arrays is then chosen and cleaned with aceton to remove the resist before mounting the chip for characterizations. The chip is mounted inside a gold-platted box to start wire bonding. This process uses a micrometer thin aluminium wire to create thermal or electric bonds between the chip and the box. The wire goes through a needle that can be lowered with

a lever and the box is placed beneath the needle on a platform that can be operated with a mouse controller. Once the aluminium wire is in contact with the chip, the needle will put a downward pressure with ultrasounds on the chip to create the first weld. The needle is then lifted and the process is repeated on the box to create the bond. If the duration and force of the ultrasounds are not high enough, the wire will not stick to the surface, if they are too high, the wire might break. The ultrasounds for the second weld are stronger to intentionally break the wire and start a new bond somewhere else. In order for the ultrasounds to be effective during welding, the chip must be held in place by four clamps with screws on each corner as seen on the picture in Fig. 3.6.
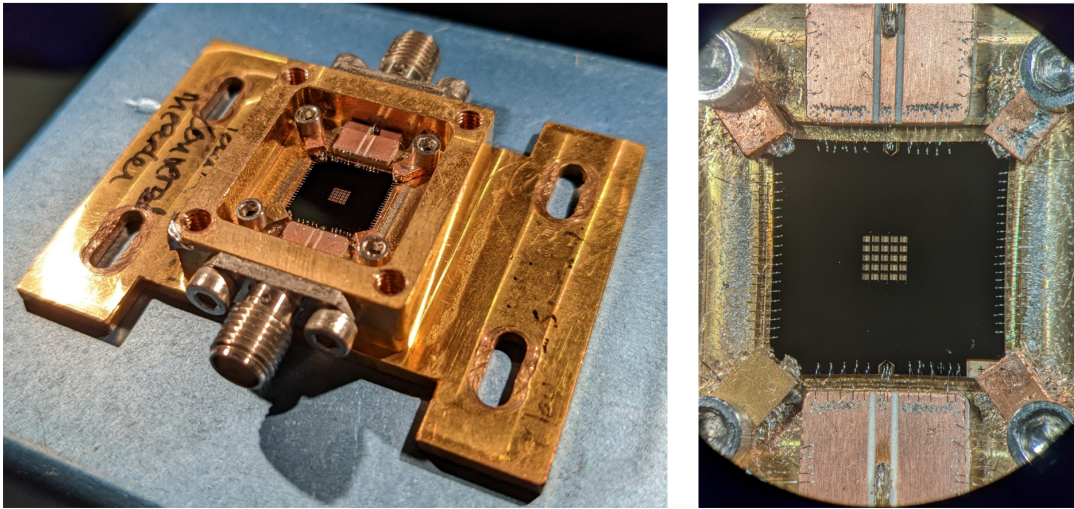
Figure 3.6: The MKIDs chip is mounted inside a gold-platted copper box and held in place by four clamps on each corner. We use aluminium wire bonding to connect the feedline to the two 50 Ω SMA connectors via CPW stripboards. We also bond aluminium wires all across the chip to define a common ground as well as thermal bridges with the box to ensure an effective thermalisation.

To further increase grip, we place soft indium chunks at the inferface between the clamp and the substrate before tightening the screws. The first use of these wires is to electrically connect a part of the chip to the box. The chip CPW center strip is connected on each side to the two 50 Ω SMA connectors for easier integration inside the cryostat later on. The CPW ground planes are all connected with the box to a common ground via these bonds. The second use of these wires is to create thermal bridges between the chip and the box to ensure an effective cooldown.

3.6 Adiabatic Demagnetization Refrigerator

In order to operate and characterize MKIDs, we need to cool down the devices to temperatures below $T_c/10$. The measurements were conducted in a cryostat made available at the AstroParticule et Cosmologie (APC) lab of Université Paris Cité. Their cryostat can reach temperatures down to 50 mK which was necessary to characterize the TLS-related phenomenon described in Sec. 5.2. All devices characterized in this work were cooled down using an Adiabatic Demagnetization Refrigerator (ADR). There is no efficient way to cool down a chip from room temperature directly to 50 mK because a cryostat can be approximated as a black body that radiates energy with a thermal gradient proportional to T^4. For this reason, the cryostat has three intermediate cooling stages: 70 K, 4 K and 1 K where each stage is thermally shielded from the previous one by a solid metal cover that halves the heat load. The 100 mK stage that hosts the MKID is shielded by a solid superconducting niobium cover from the Earth's stray magnetic field as well as the ADR strong magnetic field needed for operation. This shield is however optional for TiN-based MKIDs as TiN is not sensitive to magnetic fields. Furthermore, an external pump is used to create an insulating vacuum inside the cryostat to prevent heat conduction and convection through air or any gas medium. The cryostat is pre-cooled by a pulse-tube down to 4 K.
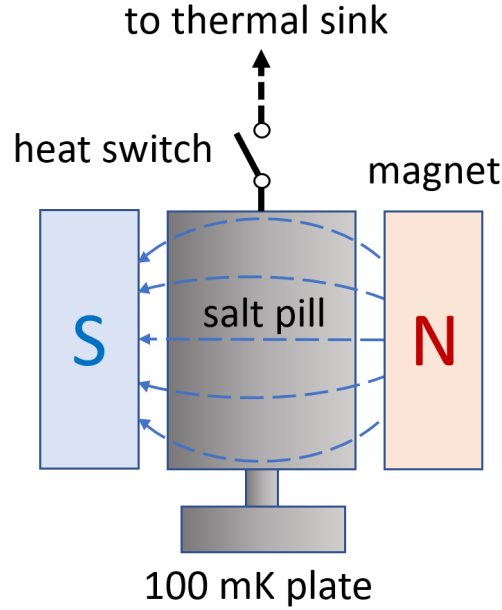
Figure 3.7: Simple ADR schematic in the operating cycle. The charged salt pill cools down the 100 mK plate by transforming thermal vibrations entropy into electron angular momentum entropy. A superconducting magnet nearby applies a magnetic field (blue dashed arrows) to the salt pill to control the plate temperature. Once the salt pill has reach a certain amount of entropy, the heat switch is closed to dump the heat into the 4 K plate thermal sink while the salt pill is being recharged.

To keep the chip to temperatures close to absolute zero, ADR goes through a cyclic cooling that alternates between an operating and charging cycle. The basic principle of ADR is to absorb heat from the entropy of random magnetic moments of a paramagnetic substance in the form of a salt pill. At the microscopic level, electrons inside the salt pill have various angular momenta called spins that do not cancel out like in most materials. When the salt is not charged, the entropy of spins which corresponds to the degree of disorder is high. If we apply a current into a nearby superconducting magnet, it can create a magnetic field strong enough to force the momenta of electrons in the salt pill to rearrange and align with minimum entropy. From this ordered state, heat can then be absorbed passively by the salt pill by transforming thermal vibrations entropy into magnetic moment entropy. In order to keep a constant bath temperature during the operating cycle, the magnetic field created by the superconducting magnet is regulated by a feedback loop to decrease slowly over time and compensate for the salt pill increasing spin entropy. In our case, a

fully charged salt pill can hold the colder stage at 100 mK for 48 hours with a recharge time of one hour. The coldest temperature our ADR can reach with reasonable stability is 50 mK which is necessary for characterizing the TLS noise in our samples. Once the current controlling the decreasing magnetic field reaches 0, the salt pill will start heating up. A highly conductive heat switch is then closed between the 1 K and 4 K stages to dump heat into the 4 K plate that is the temporary colder part of the cryostat and is called a thermal sink. The switch also stays closed during the salt pill recharging cycle because this process produces heat. Before starting the next operating cycle, the switch is open and we ensure the proper disconnection with the thermal sink via a DC block represented in Fig. 3.8. Our measurements are usually done with certain temperature steps ranging from 50 to 500 mK so we manually control the magnet current to reach these temperatures.

3.7 Readout setup
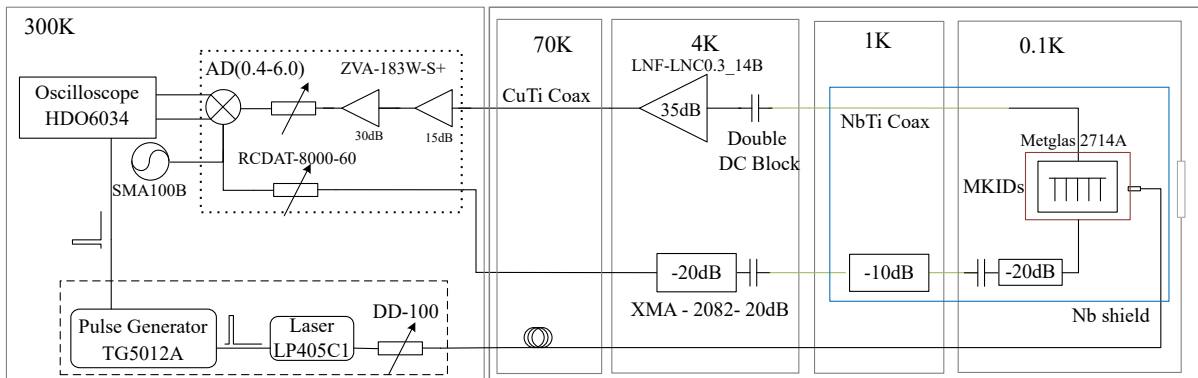
Figure 3.8: The MKIDs response is extracted from the standard homodyne detection scheme: A signal generator sends a signal with a single frequency that is attenuated through the different cryostat stages to excite the MKIDs array. It is then reamplified and multiplied with the initial signal in an I-Q mixer. The process is repeated as a frequency sweep for every point around the resonance. For photon response, the array is illuminated by an optic fiber connected to a laser. The duration and power of the pulse are controlled by a pulse generator connected to the oscilloscope for synchronization.

In order to read and characterize the MKIDs array, we use the standard homodyne detection scheme layout from Fig. 3.8. At room temperature, a Local Oscillator (LO) sends

through a coaxial cable an oscillating signal with a single frequency to the array. A first variable attenuator can reduce the signal power up to -60 dB which is used for the MKIDs readout power characterization. The signal then enters the cryostat and is respectively attenuated by -20 dB, -10 dB and -20 dB at the 4 K, 1 K and 100 mK stages before arriving to the array to excite the resonators. The output signal goes through a NbTi superconducting coaxial cable to prevent thermal noise to be amplified afterwards. According to the noise behavior in cascaded amplifier, the first amplifier of the cascade must have the highest gain and add the minium noise possible so we use a Low-Noise Amplifier (LNA) at the 4 K stage to prevent thermal noise in the readout. The LNA is followed by two room-temperature 15 dB and 30 dB amplifiers to reach the desired gain and a final 0 to -60 dB variable attenuator. The RF signal retrieved from the MKIDs is then multiplied by the original LO signal with the same frequency inside an I-Q mixer that consists of two separate mixers. The first one directly mixes both signals in-phase to retrieve the real part of the signal. The second is preceded by a phase shifter that shifts the RF signal by 90° and is then mixed with the LO signal to reconstruct the imaginary part of the modulated signal. The in-phase and quadratic components that respectively correspond to the resonator amplitude and phase are finally read on the oscilloscope. Since homodyne detection only covers a single frequency at a time, this process is repeated as a frequency sweep to cover the whole resonance and the discrete step we set can vary depending on the resonator quality factors.

For frequency noise measurements represented in Fig. 2.11, we average noise inside a certain frequency range which is called binning to avoid any eccentric value. The bin width for $f < 50$ Hz is 1 Hz, for $50 < f < 1$ kHz is 10 Hz and for $f > 1$ kHz is 100 Hz. As detailed in Sec. 2.8.1, an MKID LC resonator can be approached as a 2-port system. It can be read by a Vector Network Analyzer (VNA) that sends a signal into one of the two MKIDs ports and retrieve both the phase and amplitude of the resonator by measuring either the reflection back from the same port or the transmission through the second port. In our case, the most useful scattering parameter is the forward transmission S_{21} expressed by:

$$S_{21}(f) = A \exp(-2\pi j f \tau_c) \left[1 - \frac{\dfrac{Q}{Q_c} \exp(j\phi_0)}{1 + 2jQ\dfrac{\delta f}{f_0}} \right] \tag{3.1}$$

where A is a complex constant depending on the measurement setup, τ_c is the cable length delay, ϕ_0 is a phase shift induced by impedance mismatch and $\delta f = f - f_0$ is the spectral shift from resonance. If the VNA measures the MKID off-resonance ($\delta f \to \infty$) the forward transmission parameter $10 \log_{10}(S_{21}(f)) \to 0$ dB reaches its maximum value. When correcting for the cable delay and impedance mismatch terms, Eq. 3.1 can be expressed on resonance ($f = f_0$) as:

$$S_{21}(f_0) = 1 - \frac{Q}{Q_c} \tag{3.2}$$

For a resonator with virtually no RF loss ($Q_i \gg Q_c$), the forward transmission depth at the resonance frequency is infinite ($S_{21}(f_0) \to -\infty$). Since Q_i and Q_c are proportional as defined in Eq. 2.36, this will lead to an infinitely narrow resonance dip that cannot be sampled by the electronics. If we consider the other extreme limit ($Q_i \ll Q_c$), $S_{21}(f) \to 1$ reaches its maximum value and the resonance dip will be too shallow to be measured. As for the critical condition $Q_i = Q_c$, it corresponds to a resonance depth of $\log_{10}\left(\frac{1}{4}\right) = -6$ dB. In practice, we aim for a Q_i one order of magnitude higher than Q_c to ensure that we have a high total Q with healthy resonances that will not saturate at medium readout power. Since the internal quality factor of the resonators are usually degraded during the fabrication process, we tend to slightly overshoot Q_i in simulations. The MKID resonance derived from S_{21} can be represented in the I-Q plane as a circle where the angle and radius corresponds respectively to the phase and dissipation which can be extracted from Eq. 3.1 and 3.2:

$$\theta = -\arctan 2Q\frac{\delta f}{f_0} \qquad\qquad r = \frac{Q}{2Q_c} \tag{3.3}$$

where $\theta \in \left[-\frac{\pi}{2}; \frac{\pi}{2}\right]$ and $r \in \left[0; \frac{1}{2}\right]$.

This representation allows for more clarity concerning the evolution of the MKID resonance point under optical illumination.
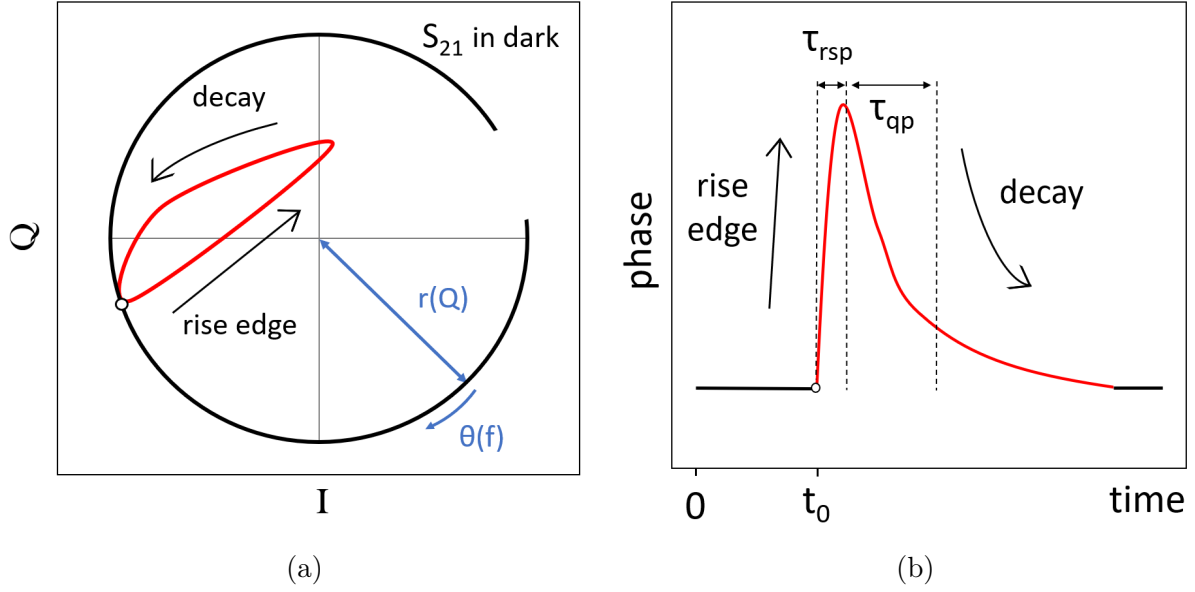
Figure 3.9: (a) Representation of the MKIDs pulse response in the I-Q plane normalized by the frequency-dependant cable delay described in Eq. 3.1. The black curve corresponds to the S_{21} under no optical illumination and the white dot the initial position of the resonance at t_0. (b) Pulse response in the time-domain where the light pulse is sent at t_0. The MKID response time τ_{rsp} and quasiparticle lifetime τ_{qp} are represented.

In the I-Q plane of Fig. 3.9a, the red curve represents the trajectory of the initial resonance point after a short light pulse. First, the rise edge goes towards the center due to quasiparticles dissipation while rotating around the circle caused by the change of kinetic inductance. Once the light pulse and Cooper pair breaking process are over, the resonance point decays back to its original. In the time-domain of Fig. 3.9b, the rise time is usually very short compared to the decay defined by the characteristic quasiparticle lifetime τ_{qp}. The frequential noise discussed in Sec. 2.9 can also be represented in the I-Q plane like shown in Fig. 3.10
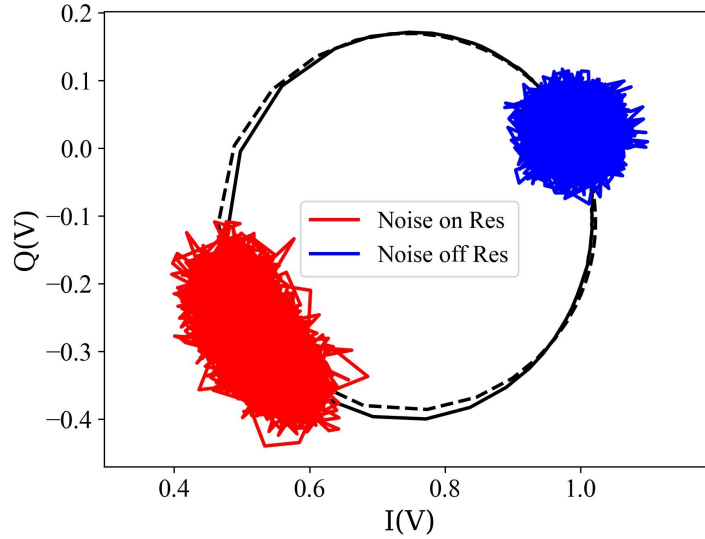
Figure 3.10: Frequential noise on and off resonance represented on the I-Q plane.

This representation confirms two things: the frequential noise measured off resonance (in blue) is white noise as it has no preferred direction and the frequential noise measured on resonance (in red) is more prominent in phase as it flattens along the resonance circle and not towards or away from the center.

3.8 Photon response setup

For photon response, a pulse generator sends a square signal with a width w_p on the order of a few hundreds of nanoseconds to one of the three available laser diode (405, 850 or 1550 nm) connected to a commercial SM980-5.8-125 optical fiber that is single-mode between 980 and 1550 nm. This fiber runs inside the cryostat to illuminate the MKIDs array and is set at a distance of 35 mm with an illumination diameter of 5 mm as presented in Fig. 3.11b.
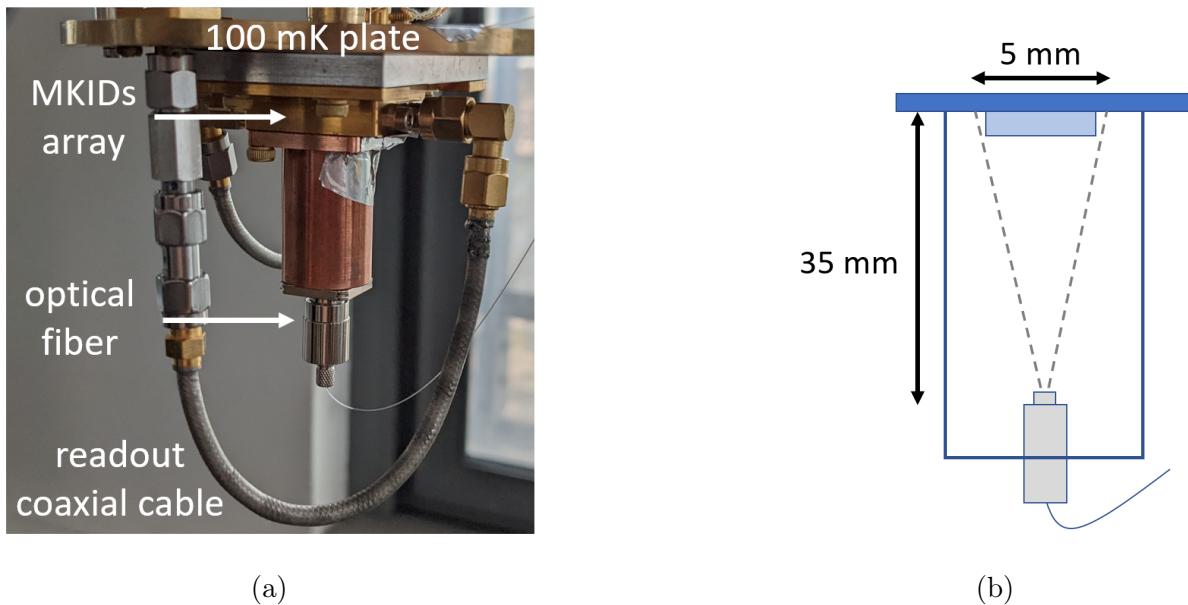
Figure 3.11: (a) Picture of the MKIDs array installed on the ADR 100 mK plate with the illumination setup. (b) Representation of the dimensions with which the MKIDs array is illuminated.

The resulting pulse response can be determined using the homodyne scheme described previously and can be compared with the original pulse generator squared signal that was also sent to the oscilloscope. The time during which the photon event can be measured is directly proportional to the quasiparticle lifetime of the material. The resonator must quickly respond to the change in surface impedance in order to be read by the electronics before quasiparticles recombine. This response time is proportional to the resonator bandwidth and can be expressed as:

$$\tau_{\mathrm{rsp}} = \frac{Q}{\pi f_0} \tag{3.4}$$

and should satisfy $\tau_{\mathrm{rsp}} \ll \tau_{qp}$ to ensure a proper photon detection.

3.9 Optimal filtering for single-photon detection

In order to determine the energy resolution of our MKIDs, we have to accurately quantify the phase shift induced by a single photon. We use the illumination setup described in the previous section with very short light pulses of 20 ns with a 25 dB attenuation and record

the MKIDs phase response. It is safe to assume that there are thousands of photons hitting the detector with each pulse but considering the large illumination area, the MKIDs filling factor, its absorbance and quantum efficiency, only a few photons or sometimes none are actually detected by each pixel. Even though optical MKIDs are photon-noise limited, their intrinsic noise level dominated by TLS or G-R are usually around an order of magnitude lower, which means that it is impossible to extract the single-photon response from the raw data. Instead, if we assume the MKIDs phase response to follow an exponential distribution, we can use optimal filtering in the frequency domain to remove most of the coloured noise. Since this work only focus on sample characterization, the filtering is not done in real-time but rather with post-processing. Let us consider the phase response whose actual amplitude A is mixed with frequency-dependant noise $N(f)$, the Fourier transform $\Phi(f)$ of the raw phase response $\phi(t)$ can be written as:

$$\Phi(f) = AM(f) + N(f) \tag{3.5}$$

where $M(f)$ is the model of what the actual amplitude A should look like. $M(f)$ can be obtained by simply averaging the phase response of the resonator over a few hundreds of discrete light pulses. Photon noise is not white but rather follows a Poisson distribution so the template will naturally converge towards the desired shape. This template is then converted in the frequency domain using the Fourier transform and normalized by 1. As for determining the frequential noise $N(f)$ of the MKID, it has already been covered in Sec. 3.7. An example of $M(f)$ and $N(f)$ has been represented in Fig. 3.12.
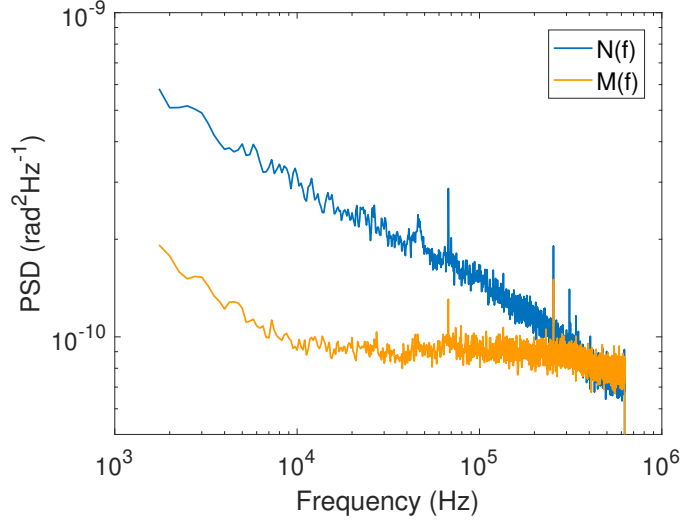
Figure 3.12: Example of the spectral density of the MKID noise $N(f)$ and its phase response template $M(f)$ taken from the reference sample that has given single-photon response.

Finally, we can write the equation for the optimal filter as [65]:

$$A = \frac{\displaystyle\int_{-\infty}^{+\infty} \frac{\Phi(f)M^*(f)}{|N(f)|^2}df}{\displaystyle\int_{-\infty}^{+\infty} \left|\frac{M(f)}{N(f)}\right|^2 df} \tag{3.6}$$

where $M^*(f)$ denotes the conjugate transpose of $M(f)$. The pulse amplitude in Eq. 3.6 is estimated at each frequency and averaged by the square of the SNR $|M/N|^2$.

Chapter 4

Optical stack MKIDs

The principle of improving photon coupling to a detector has been relevant in nature for thousands of years, long before human-made detectors ever existed. The biological evolution of numerous nocturnal species is responsible for a very complex reflecting layer behind their retina known as *tapetum lucidum* [66]. It has allowed for better visibility at night where they must stay alert to hunt for some, or avoid being hunted for others. Since the last century, for astronomical applications, researchers have mimicked the tapetum lucidum in the form of a backshort cavity to increase the optical coupling in conventional detectors but also in superconducting technologies such as TES [67]. In recent years, considerable efforts have been put towards optical coupling in MKIDs for visible and NIR bands. It has been claimed in simulations that unity absorption can be reached by using either an anti-reflection coating above the sensitive part of the pixel and/or a reflector below [68, 69]. However, there has been no follow-up on actual high-Q MKIDs using these geometries since, let alone improving the optical coupling. We will discuss in this work the significant amount of photons in the visible and NIR range that are lost by transmission through the absorber layer as we try to increase the detector's sensitivity by reducing the volume of the absorber [11]. Since we cannot reduce its area more than the microlens arrays allow us, the only remaining dimension on which we can play is thickness. Here, we propose to place a reflecting layer below the absorber separated by a quarter-wave-thick dielectric layer that will act as a backshort cavity to retrieve photons that have been transmitted through and offer a second pass on the sensitive part of the pixel. We will first study the optical parameters of the thin layers to find the optimal coupling geometry

and present the MKID design in simulations. Finally, we will characterize the fabricated sample as well as reference samples for an in-depth analysis of the performance of the optical stack geometry and influence over the resonator.

4.1 Theoretical model of the optical stack

In order to design an effective optical stack, it is essential to accurately determine the optimal thickness of each layer. It is important to note that both the spectrometer measurements and the transmission line model from ellipsometry measurements that will be covered in these next sections consider the layers to be solid and do not take into account the absorber meander shape for the ease of this study. This might induce small variations when applied to the actual MKIDs array but should not tamper with the actual designing of the optical stack dimensions.

4.1.1 1-layer model

A photon can be described as a complex electromagnetic wave $\tilde{u}(z) = \tilde{E} \exp\left[j(\omega t - \tilde{k}z)\right]$ with a complex wave number $\tilde{k}(\lambda)$ that is wavelength dependant. The change of medium from free space to the first layer of our detector will act as a lossy perturbation to incoming photons which translates into a complex refractive index:

$$\tilde{n} = n - j\kappa \tag{4.1}$$

where κ denotes the extinction coefficient that quantifies the attenuation of absorbed light relative to the distance z inside the medium and is not to be mistaken with the notation of the wave number. In the case of a transparent dielectric layer such as Al_2O_3, the attenuation is negligible so $\kappa = 0$. From Eq. 4.1, a few optical quantities can be introduced such as the phase velocity of the incident wave $\omega/\tilde{k} = c/\tilde{n}$ where c is the speed of light in vacuum and the complex relative permittivity given by:

$$\tilde{\epsilon} = \tilde{n}^2 = \epsilon_a - j\epsilon_b \tag{4.2}$$

The real and imaginary part of $\tilde{\epsilon}$ can be obtained from n and κ that are available to us

by ellipsometry using these relations:

$$\epsilon_a = n^2 - \kappa^2 \qquad\qquad \epsilon_b = 2n\kappa \qquad\qquad (4.3)$$

We can now introduce the dielectric loss tangent induced by the electromagnetic wave and defined by the angle with the impedance plane of the layer. It can be expressed from the dielectric dispersion equation in terms of complex relative permittivity by:

$$\tan \delta_\epsilon = \frac{\epsilon_b}{\epsilon_a} \qquad\qquad (4.4)$$

Finally, we can describe the complex wave number $\tilde{k}$ and impedance of the electromagnetic wave $\tilde{\eta}$ with said dielectric loss tangent $\tan \delta_\epsilon$ by [69]:

$$\tilde{k} = k\sqrt{\epsilon_a(1 - j\tan\delta_\epsilon)} \qquad\qquad \tilde{\eta} = \frac{\eta_0}{\sqrt{\epsilon_a(1 - j\tan\delta_\epsilon)}} \qquad\qquad (4.5)$$

where $\eta_0 = \sqrt{\mu_0/\epsilon_0} \approx 376.73\ \Omega$ is the intrinsic impedance of a free-space medium and $k = 2\pi/\lambda$. In the case of a lossless dielectric thin film ($\delta_\epsilon = 0$), $\tilde{k} = k\sqrt{\epsilon_a}$ and $\tilde{\eta} = \eta_0/\sqrt{\epsilon_a}$. For a perfect electrical conductor ($\delta_\epsilon = \frac{\pi}{2}$), $\tilde{k} = -\infty$ and $\tilde{\eta} = 0$.

When a photon that is initially in free space ($\tilde{n}_0, \tilde{k}_0$) arrives at a normal incidence on the thin film medium of our detector ($\tilde{n}_1, \tilde{k}_1$) at position $z = z_f$, the incident wave $\tilde{u}_I(z < z_f) = \tilde{E}_I \exp\left[j(\omega t - \tilde{k}_0 z)\right]$ give rise to a transmitted wave given by [70]:

$$\tilde{u}_T(z > z_f) = \frac{2\tilde{n}_0}{\tilde{n}_0 + \tilde{n}_1} \tilde{E}_I \exp\left[j\tilde{k}_0 z_f\left(\frac{\tilde{n}_1}{\tilde{n}_0} - 1\right)\right] \exp\left[j\left(\omega t - \frac{\tilde{n}_1}{\tilde{n}_0}\tilde{k}_0 z\right)\right] \qquad (4.6)$$

and a reflected wave given by:

$$\tilde{u}_R(z < z_f) = \frac{\tilde{n}_0 - \tilde{n}_1}{\tilde{n}_0 + \tilde{n}_1} \tilde{E}_I \exp(-2j\tilde{k}_0 z_f) \exp\left[j(\omega t + \tilde{k}_0 z)\right] \qquad\qquad (4.7)$$

From Eq. 4.6 and 4.7, the transmittance and reflectance between the two media can thus be defined respectively as $T_0 = \left|\frac{2\tilde{n}_0}{\tilde{n}_0 + \tilde{n}_1}\right|^2$ and $R_0 = \left|\frac{\tilde{n}_0 - \tilde{n}_1}{\tilde{n}_0 + \tilde{n}_1}\right|^2$

4.1.2 P-layers model

The same principle described in the previous section can be applied to a stack of multiple layers where the different wave components can be determined at each interface but will not be covered here due to its considerable length. Instead, we will describe the optical stack as a series of P transmission lines as shown in Fig. 4.1 where the optical parameters of the p-th line experimentally measured are η_p, $\tilde{k}_p$ and the transmission line length d_p.
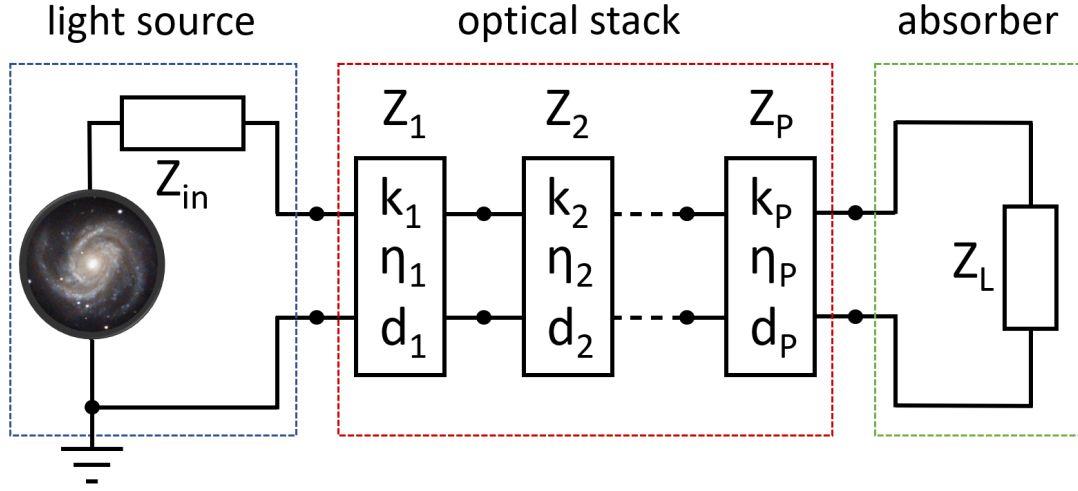
Figure 4.1: Schematic representation of the transmission line model with P layers used in this study to match the light source impedance Z_{in} with the MKID absorber Z_L.

The transfer matrix M_p of the p-th layer can be cascaded with the other matrices to extract the total optical stack parameters. The total transfer matrix M_{tot} of the cascaded P layers constituting the optical stack can be expressed as the product of the matrices M_p of each p-layer by:

$$M_{\text{tot}} = \begin{bmatrix} M_{11} & M_{12} \\ M_{21} & M_{22} \end{bmatrix} = \prod_{p=1}^{P} M_p = \prod_{p=1}^{P} \begin{bmatrix} \cos(\tilde{k}_p d_p) & j\eta_p \sin(\tilde{k}_p d_p) \\ j\eta_p^{-1} \sin(\tilde{k}_p d_p) & \cos(\tilde{k}_p d_p) \end{bmatrix} \tag{4.8}$$

The modelled total reflection R_m and transmission T_m through the optical stack can be extracted from Eq. 4.8 as:

$$R_m = |M_{11}|^2 \qquad\qquad T_m = |M_{12}|^2 \tag{4.9}$$

4.2 Measurements of optical film parameters

The different optical parameters of the thin films that constitute the optical stack were characterized by a commercial spectrometer in order to compare possible deviations with the theoretical model proposed in the previous section.

4.2.1 Spectrometry measurements

The measurements of thin films transmission and absorption were conducted at Laboratoire d'Etudes du Rayonnement de la Matière en Astrophysique (LERMA) using a commercial optical spectrometer with a 400-1000 nm wavelength range. The transmission measurement as illustrated in Fig. 4.2a consists of sending a collimated light beam through the sample wafer and split the ouput light as an intensity spectrum. A neutral-density filter can eventually be used to attenuate the intensity of the light source in case it saturates the spectrometer.

(a)

(b)
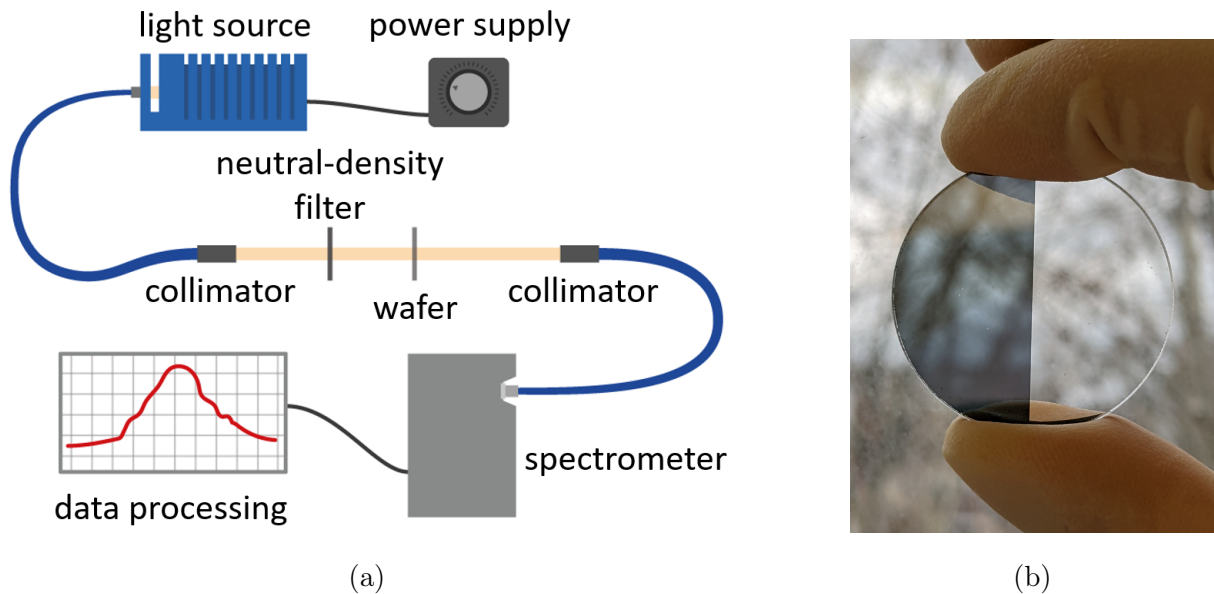
Figure 4.2: (a) Illustration of the experimental measurement of transmission through a sample wafer. Light from a powered source is collimated inside an optical fiber towards the sample wafer and is retrieved inside a second optical fiber with a collimator to be sent to the spectrometer that is connected to a computer to save the data. (b) Picture of a sample wafer on which the studied layer is deposited on only half the surface.

In order to obtain the total transmission T_s, the thin film is deposited only on one half

of the surface by a simple photolithography process while the other half is used as a transmission reference through the transparent fused silica (amorphous SiO_2) substrate depicted in Fig. 4.2b. The measurements on each half are done successively by translating the sample wafer relative to the light beam to keep a normal incidence in relation with the sample wafer's surface and avoid decollimation. In case the thin film is not transparent enough, it is recommended to increase the integration time of the spectrometer to obtain a better resolution in the spectrum. In order to remove the dark current noise inherent to the spectrometer, it is necessary to calibrate the "light" spectra S_f and S_r with "dark" spectra D_f and D_r with the light source off and the corresponding integration times t_f and t_r. Each spectrum acquisition is repeated 10 times to refine the measurements. The resulting transmission spectrum T_s corresponds to the ratio of the calibrated light spectra and is normalized by the integration time of each half as follow:

$$T_s = \frac{S_f - D_f}{S_r - D_r} \times \frac{t_r}{t_f} \tag{4.10}$$

The reflection measurements differ slightly from the transmission measurements. In Fig. 4.2a, the receiving end of the optical fiber would be placed on the same side as the input beam. The two ends have a small angle of incidence $\approx 10°$ relative to the normal of the wafer's surface which is considered to be 0 for ease of processing. Since we measure the reflection on the substrate, we have to take into account the reflectance of fused silica that can be found in literature as $R_{SiO_2} = 0.034$ in the visible range for angles $\leq 10°$ [71]. The same spectrum acquisition and calibration steps conducted for transmission are reproduced here and the total reflection R_s can be expressed similarly as in Eq. 4.10 by:

$$R_s = \frac{\frac{S'_f - D'_f}{S'_r - D'_r} \times \frac{t'_r}{t'_f}}{2R_{SiO_2}} \tag{4.11}$$

The $\frac{1}{2}$ factor is here to remove the substrate backside reflection that would otherwise double the intensity of the reflected light.

4.2.2 Ellipsometry measurements

The complex refractive index of some thin films used in this work like aluminium are well established in literature. Others like reactively sputtered TiN_x are less common and have optical properties that greatly vary from one report to the other, or even from one year to the other as we experienced. For the sake of a refined model towards the optimization of the optical stack, the complex refractive index of every different layer we deposit have been kindly measured at Centre de Nanosciences et Nanotechnologies (C2N). The principle of ellipsometry is to extract the complex refraction index of a material from the vertical and horizontal polarization components of light reflected off the material surface which are respectively named $r_p(n, \kappa, d)$ and $r_s(n, \kappa, d)$. The material is deposited on a high-resistivity silicon substrate with known optical constants to easily remove its influence on the measurements.
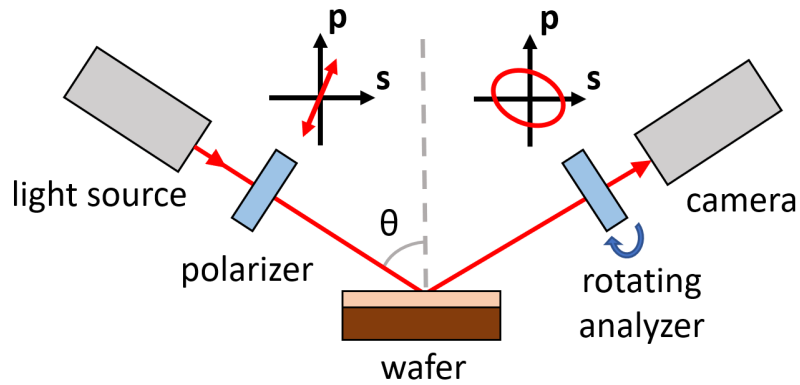
Figure 4.3: Representation of the ellipsometry technique to determine the complex refractive index of our thin films. A light source with a known linear polarization is reflected off the sample wafer to create a circular polarization that is analyzed by a camera.

As illustrated in Fig. 4.3, a beam of light is linearly polarized by a polarizer in a direction that must contain both p and s plane polarization components. The light is then directed towards the sample wafer with a known angle θ to the normal of the wafer's surface that is usually close to the Brewster angle to have a maximal response difference between r_p and r_s. The reflected light is elliptically polarized and can be described as a sine wave by placing a rotating analyzer in front of the camera. The resulting amplitude Ψ and phase Δ of this sine wave are given by [72]:

$$\Psi = \arctan \frac{|r_p|}{|r_s|} \qquad\qquad \Delta = \arg(r_p) - \arg(r_s) \qquad (4.12)$$

The output signal is then compared with the input signal to obtain the amplitude and phase shift. Since the thickness of the measured layer d is known, it is possible to determine the two unknown quantities n and κ from the three measured parameters $r_p(n, \kappa, d)$, $r_s(n, \kappa, d)$ and d.

4.3 Optical stack model and measurements results

In the following subsections, we will successively present each layer optical parameters that have been measured by spectrometry and compare it with the transmission line model that uses the complex refractive index obtained by ellipsometry. We will also discuss the optimal thickness of each layer to maximize absorption within the sensitive part of the MKID.

4.3.1 Aluminium reflector

The first element of the optical stack is the reflector. We chose aluminium because of its reflectance close to unity in the 400-1600 nm range. The optical parameters of aluminium that will be used in this study have not been measured by ellipsometry because they are already well established in literature [73].
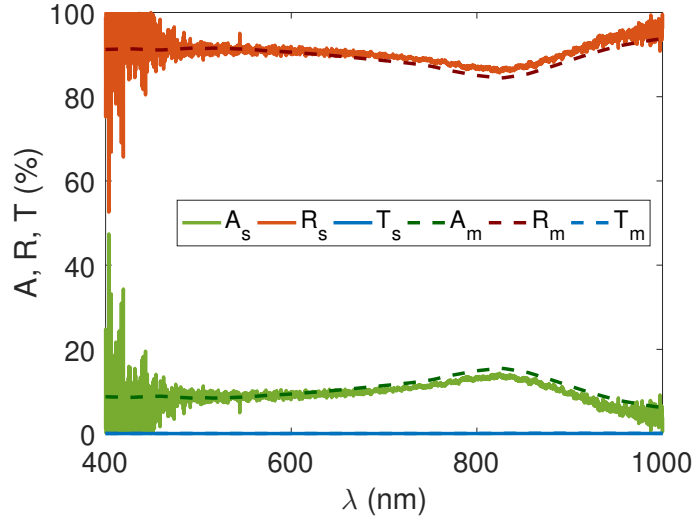
Figure 4.4: Measurements of absorbance, reflectance and transmittance from spectrometry (A_s, R_s and T_s) and from the model based on ellipsometry measurements (A_m, R_m and T_m) for a 50 nm-thick aluminium layer.

In Fig. 4.4, the measurements done by spectrometry on a 50 nm aluminium film show that the reflectance R_s is above 90% across the whole range which is consistent with the transmission line model R_m represented by the red dashed curve. As expected for aluminium, both the measured and modelled transmittance are null. The absorbance is deduced from reflectance and transmittance by $A = 1 - (R + T)$ which explains why in this particular case A_s and A_m are perfectly symmetric to R_s and R_m respectively.
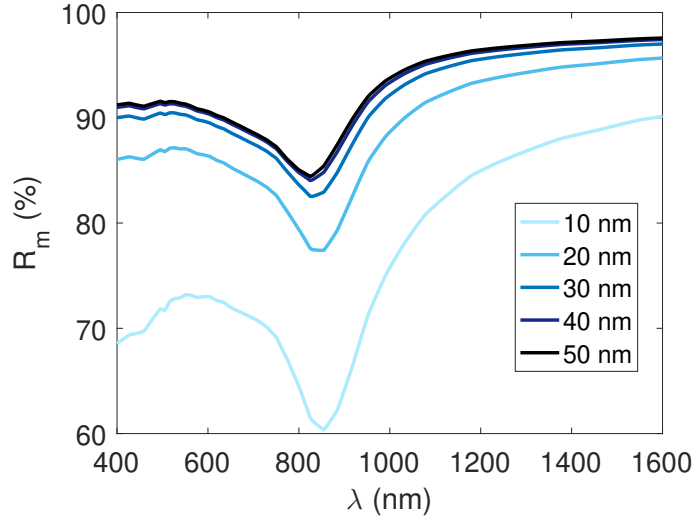
Figure 4.5: Modelled reflectance R_m of an aluminium film with a thickness ranging from 10 to 50 nm

From the transmission line model, we can quickly determine the minimum thickness aluminium must have to reach its maximum reflectance. The results shown in Fig 4.5 indicate that the thickness of the aluminium film should not be thinner than 30 nm, otherwise there would be significant loss by transmission. Since there is an uncertainty of a few nanometers during sputtering, we will aim for a 40 nm thick aluminium layer in our design. A thicker aluminium layer could introduce step coverage issue between the capacitor directly on the substrate and the inductor atop the optical stack.

4.3.2 Aluminium oxide spacer layer

On top of the aluminium reflector is a dielectric spacer layer. The main purpose of this spacer layer is to electrically isolate the two conductive components of the optical stack which are the absorber and the reflector. The addition of a dielectric layer will necessarily introduce dielectric tangent loss so it is critical to choose a material accordingly. During the first year of this study, the only material available to us was silicon monoxide (SiO) in the form of grains that were thermally evaporated onto the wafer. This process described in Sec. 3.3.2 is known to evaporate unwanted particles that are present in the chamber which affects the film quality. There is also little control over the film thickness which can be problematic when optimizing the optical coupling of the stack. Following the measurements of the MKIDs internal quality factor, the resulting SiO layer was indirectly

determined by simulations to have a high $\tan\delta \approx 10^{-4}$. Later on, the ALD technique described in Sec. 3.3.3 became available thanks to our cooperation with Ecole Normale Supérieure (ENS) so we transitioned from evaporated SiO to ALD Al_2O_3. This technique was previously used by our group to replace large IDC capacitors with smaller Metal-Insulator-Metal (MIM) capacitors that drastically increased MKIDs spatial resolution while keeping the same operating bandwidth [74]. In that study, the insulating part of the MIM was Al_2O_3 deposited by ALD which has allowed for high MKIDs $Q_i = 10^5$. Similarly to the SiO layer, we indirectly measured the dielectric loss tangent of ALD Al_2O_3 to be $\tan\delta \approx 10^{-6}$ which is two orders of magnitude less than for SiO. The deposition of Al_2O_3 free of unwanted particles, the lower dielectric losses and the better control over the film thickness make it a preferable alternative over evaporated SiO. The refractive index of dielectrics is purely real ($\kappa = 0$) so the only optical constant we measured by ellipsometry for Al_2O_3 is represented in Fig. 4.6 and is consistent with values reported elsewhere [75].
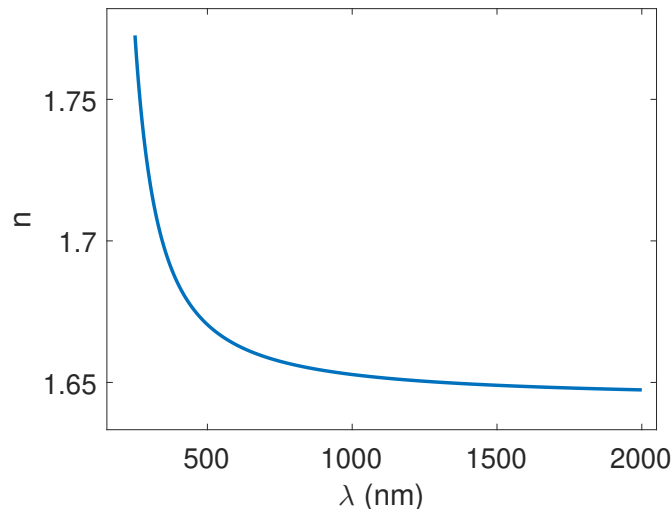
Figure 4.6: Real refractive index of an Al_2O_3 layer measured by ellipsometry.

Apart from isolating two conductive layers with low dielectric loss, Al_2O_3 has been chosen for its excellent transparency in the 400-1600 nm range. The spacer layer thickness can be tuned to match the impedance of the other optical stack layers and maximize transmission or reflection when needed. Thankfully, the transmission line model takes into account the medium impedance defined by the dielectric constant in Eq. 4.5. Consider Z_{in} the front end impedance (input), Z_L the back-end impedance (load) and Z_1 the Al_2O_3 layer

impedance with finite length d_1 and refractive index n_1 illustrated in Fig. 4.1, the input impedance is given by:

$$Z_{in} = Z_1 \frac{Z_L + jZ_1 \tan(kn_1d_1)}{Z_1 + jZ_L \tan(kn_1d_1)} \tag{4.13}$$

If we want to achieve maximum transmittance, the transmission line should not disrupt the impedance of the passing photon wave. In the case of a single layer in-between two free-space media, the length of the line should be $d_1 = \lambda/2n_1$ to match the input impedance with the load. In Eq. 4.13, the imaginary part will be reduced to 0 as the term $\tan\left(\frac{2\pi}{\lambda}\frac{n_1\lambda}{2n_1}\right) = 0$ which results in $Z_{in} = Z_L$. As expected in Fig. 4.7, the first non-zero transmission maximum is centered on $\lambda/2n$ (mod $\lambda/2$) and since $\kappa = 0$ for dielectrics, the amplitude of the wave is not dampened by the transmission line.
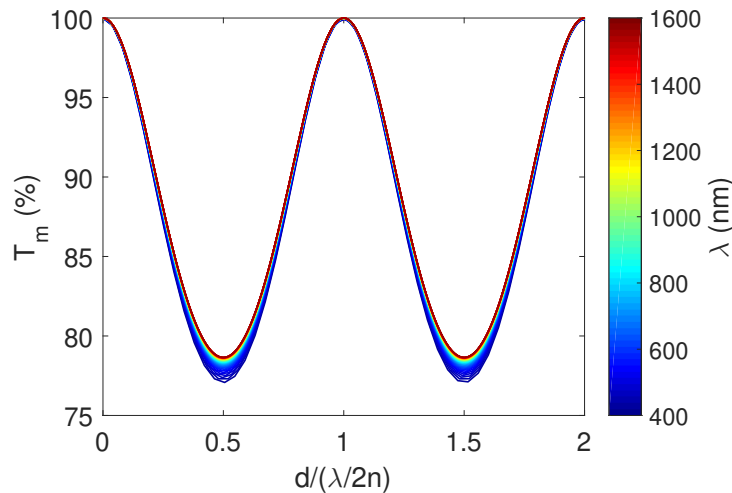
Figure 4.7: Modelled transmittance of Al_2O_3 with a variable thickness d normalized by the guided half-wavelength $\lambda/2n$ with n the Al_2O_3 refractive index.

The coloured curves represent the transmittance for an incident photon wavelength ranging from 400 nm (blue) to 1600 nm (red). As an example, for an incident photon with $\lambda = 400$ nm, the dielectric thickness must be $d = \lambda/2n = 120$ nm to achieve unity transmission. The actual dielectric thickness embedded in the optical stack cannot be computed this way before considering the influence of the absorber layer on the input impedance that will be discussed in the next subsections. We can also model the Al_2O_3 layer on top of the aluminium reflector to determine the thickness needed to obtain maximum reflectance as we ultimately want to reflect as much light as possible back to the

absorber. The results obtained in Fig. 4.8 are consistent with Fig 4.7 as it is centered on $\lambda/2n$ again.
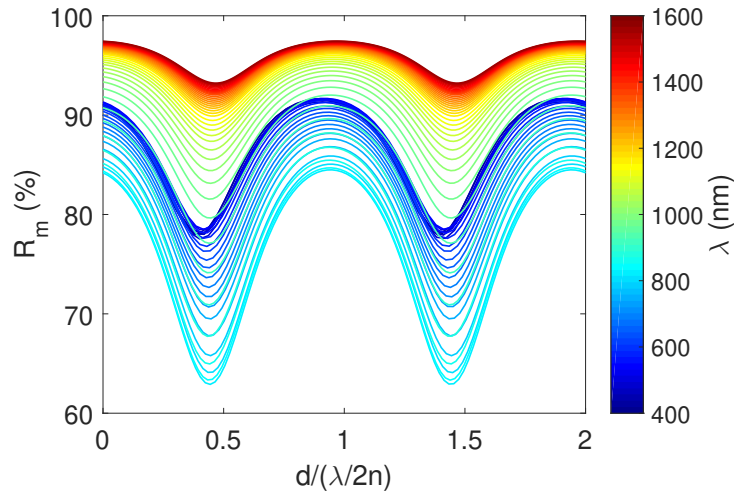
Figure 4.8: Modelled reflectance of the 40 nm thick aluminium reflector layer preceded by a Al_2O_3 layer with a variable thickness d normalized by the guided half-wavelength $\lambda/2n$ with n the Al_2O_3 refractive index.

Since the Al_2O_3 layer corresponds to the first change of medium in both Al_2O_3 and Al_2O_3/Al models, it is expected that maximum reflectance of the Al_2O_3/Al stack occurs when the transmittance of Al_2O_3 is the highest. The amplitude of reflectance is wavelength-dependant because of aluminium that do not have a constant reflectance across the 400-1600 nm range. The lowest and highest curves in Fig. 4.8 respectively corresponds to 800 and 1600 nm which is consistent with the minimum and maximum reflectance of aluminium shown in Fig. 4.5.

4.3.3 Stoichiometric TiN absorber

In this work, most of the early fabricated samples were made using stoichiometric TiN as the absorber because sub-stoichiometric TiN_x was not yet fully characterized. The main advantage of using stoichiometric TiN is that we deposit it with a nitrogen flow of 6 sccm that is outside the unstable region of Fig. 3.5 so it is easier to achieve the required homogeneity over a large surface needed for kilopixels arrays. However, photon counting has never been achieved with stoichiometric TiN that is less sensitive than TiN_x. We will thus investigate whether the optical stack could compensate for this decreased sensitivity

to achieve single photon mode with TiN. The optical constants presented in Fig. 4.9 of our deposited TiN thin film were measured by ellipsometry according to the experiment detailed in Sec. 4.2.2.
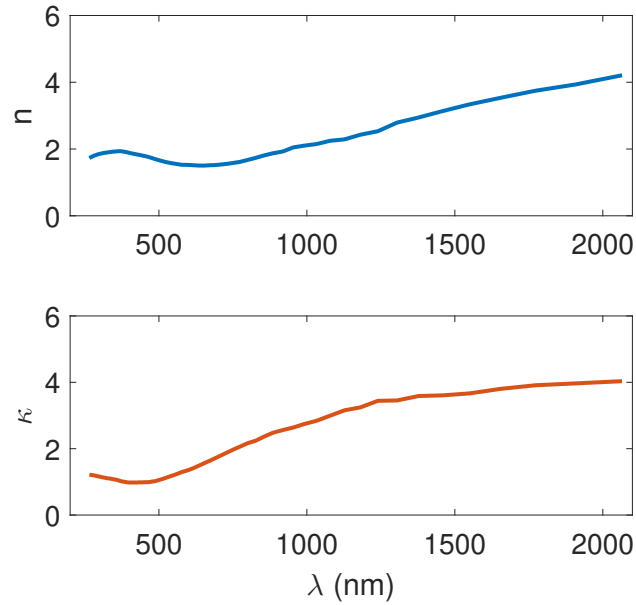
Figure 4.9: Measurements by ellipsometry of the real refractive index n and imaginary extinction coefficient κ of a stoichiometric TiN film as a function of wavelength λ.

The values we obtain are in accordance with measurements reported elsewhere [68, 76]. From these two optical constants, we can now model the expected reflectance and transmittance detailed in Sec. 4.1.2.
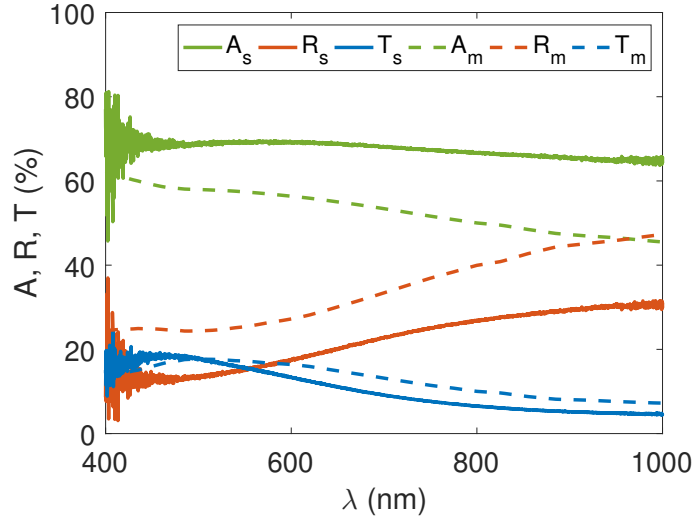
Figure 4.10: Measurements of absorbance, reflectance and transmittance from spectrometry (A_s, R_s and T_s) and from the model based on ellipsometry measurements (A_m, R_m and T_m) for a 60 nm-thick stoichiometric TiN layer.

From Fig. 4.10, we observe that the indirectly measured absorbance of a 60 nm thick TiN film is very high, around 70% across the 400-1000 nm range. The measured transmittance and reflectance however do not exceed 30%. The mixture of nitrogen with titanium changes the optical properties of the film from a highly reflective metal to a darker brownish ceramic material with increased absorbance. In the case of stoichiometric TiN, the optical stack could potentially increase the film absorbance closer to unity but its overall optical influence will have a limited efficiency compared to the TLS noise the dielectric might introduce. The transmission line model is also represented in Fig. 4.10 and seems to fit the measurements correctly except for an offset in reflectance that is around 15% higher than measured. The offset is also present in absorbance because it is directly computed from transmittance and reflectance. Now that we have finally determined the optical parameters of each layer composing the optical stack, we can determine the optimal thickness of the Al_2O_3 layer to reflect as much photons as possible back to the absorber. Unlike Al_2O_3, TiN has a complex refractive index whose amplitude almost doubles between 500 and 1000 nm as seen in Fig. 4.9. This means that an optimal dielectric thickness can be computed locally but will never be valid globally. Since we are looking to reflect lost photons transmitted through the absorber, we will optimize the dielectric thickness where TiN transmittance is the highest. According to the measurements and model in Fig. 4.10,

this corresponds to the 400-800 nm range where $T_m > 10\%$. In the same fashion as in the previous subsections, we can model the total optical stack as a function of dielectric thickness. The useful parameter that will give us information on the stack influence is the reflectance plotted in Fig. 4.11.
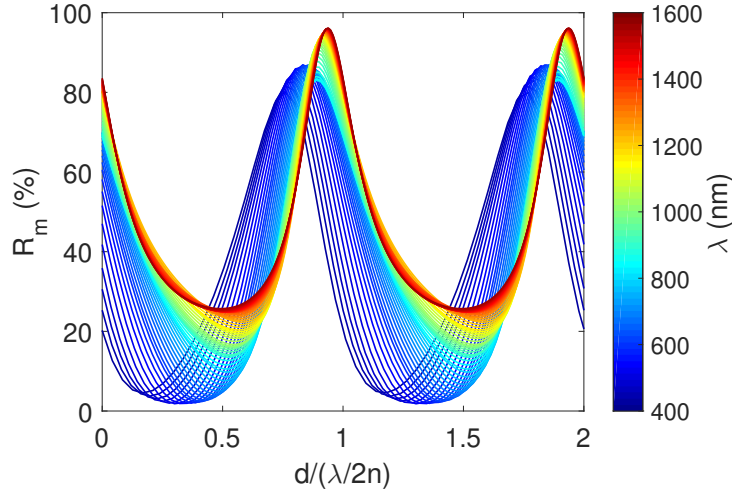
Figure 4.11: Modelled reflectance off the whole optical stack with a 60 nm thick TiN 6 sccm layer, an Al_2O_3 layer with a variable thickness d and a 40 nm thick aluminium reflector layer. The thickness d is normalized by the guided half-wavelength $\lambda/2n$ with n the Al_2O_3 refractive index.

The modelled reflectance we obtain is the combination of the reflection of every layer and is not as straightforward as in previous figures. In this stack, reflectance is mostly caused by the TiN absorber which reflects around 20% of the total incident photons as well as the Al reflector that reflects around 90% of the 20% transmitted photons. Since the model assumes that $\kappa = 0$ for the dielectric layer, the considerable variations in reflectance amplitude for a particular wavelength is only caused by the variation of the dielectric thickness. The efficiency of the optical stack thus relies on how much light it can trap. In other terms, we aim for a dielectric thickness where the modelled reflectance R_m is the lowest. For most wavelengths, the optimal thickness in Fig. 4.11 corresponds to the guided quarter-wavelength $\lambda/4n$. This remarkable length is widely used in electronics and optics to match the impedance of a source with the load. The resulting input impedance can be computed from Eq. 4.13 as $Z_{in} = Z_1^2/Z_L$. If we optimize the optical stack for photons in the 400-800 nm range following the quarter-wave condition, this corresponds to a dielectric

thickness ranging in-between 50 and 70 nm. For our design, we will take the mean value of 60 nm. The continuous blue curve in Fig 4.12 obtained by spectrometry confirms that adding the 60 nm thick Al_2O_3 layer below the TiN layer does not deteriorate the transmission and even slightly improves it thanks to impedance matching between layers which is consistent with the dashed curves that represent the transmission line model (triangles) and Zemax simulations (circles).
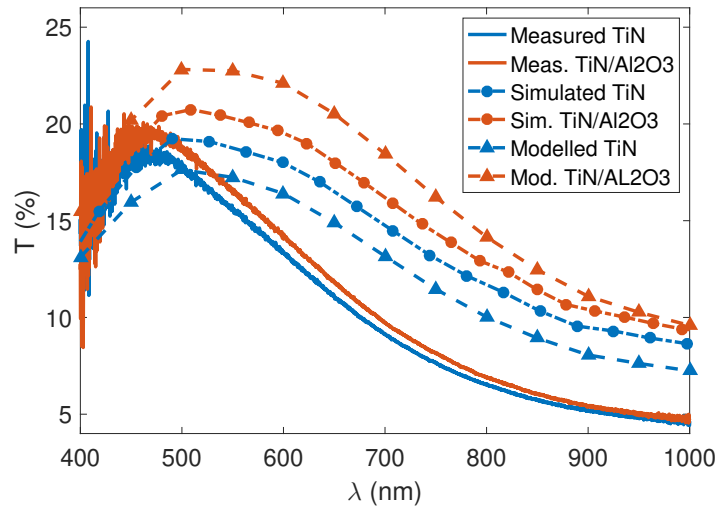
Figure 4.12: Transmittance of a 60 nm-thick TiN 6 sccm layer with a 60 nm-thick Al_2O_3 layer below (in red) and without (in blue). The continuous lines represent direct spectrometry measurements, the triangles represent the model from ellipsometry measurements and circles represent Zemax simulations.

To summarize, the optical stack from front to back consists of a 60 nm TiN absorber layer, a 60 nm Al_2O_3 spacer layer and a 40 nm Al reflector. The reflectance of this configuration was measured by spectrometry as represented in blue in Fig. 4.13 and is consistent with the transmission line model represented in red.
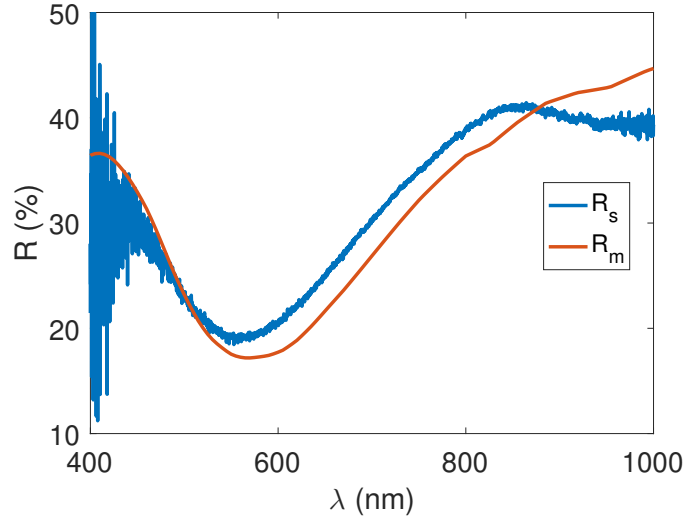
Figure 4.13: Reflectance off the whole optical stack with a 60 nm thick TiN 6 sccm layer, a 60 nm thick Al$_2$O$_3$ layer optimized for the 400-800 nm photon range and a 40 nm thick aluminium reflector layer. The spectrometry measurements and model from ellipsometry measurements concur on a dip in reflectance centered on 600 nm. This means that the optical stack is most efficient in this area as expected from the thickness optimization for that range.

The dip in reflectance is centered on 600 nm as it is the median value of the 400-800 nm range chosen for the spacer layer optimization.

4.3.4 Sub-Stoichiometric TiNx absorber

Ultimately, if we want to precisely determine the quantum efficiency increase from the optical stack, we have to use a more sensitive material for the absorber to get single-photon response. In parallel with this work, we have characterized sub-stoichiometric TiN$_x$ with a 4.9 sccm N$_2$ flow and a measured $T_c \approx 2$ K. The optical constants of sub-stoichiometric TiN$_x$ are inconsistent in literature because of its unstable crystallographic structure so it is necessary to measure by ellipsometry the refractive index of the TiN$_x$ films we grow.
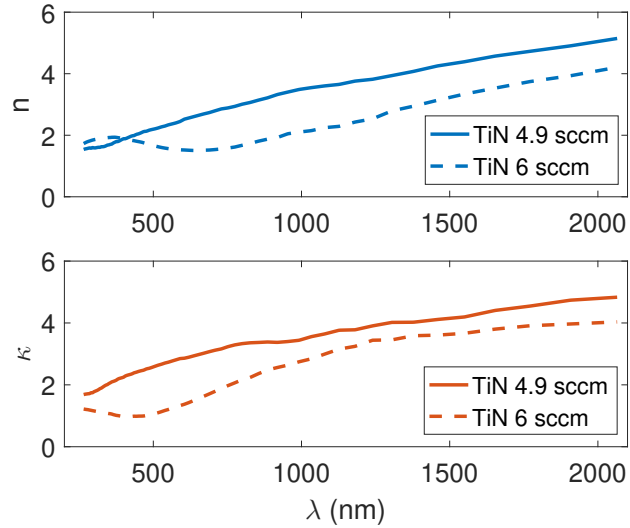
Figure 4.14: Measurements by ellipsometry of the real refractive index n and imaginary extinction coefficient κ of a sub-stoichiometric TiN_x film as a function of wavelength λ. The optical constants of TiN 6 sccm first shown in Fig. 4.9 are represented again here in dashed lines for comparison.

The complex refractive index of TiN_x shown in Fig. 4.14 differs at shorter wavelengths from TiN. As TiN_x has a more metallic composition, the extinction coefficient is naturally higher. In the same fashion as for TiN, we have deposited thin films measured by spectrometry and compared to the transmission line model that uses the optical constants obtained by ellipsometry represented in Fig. 4.15.

(a) $t_1 = 60$ nm   (b) $t_2 = 30$ nm
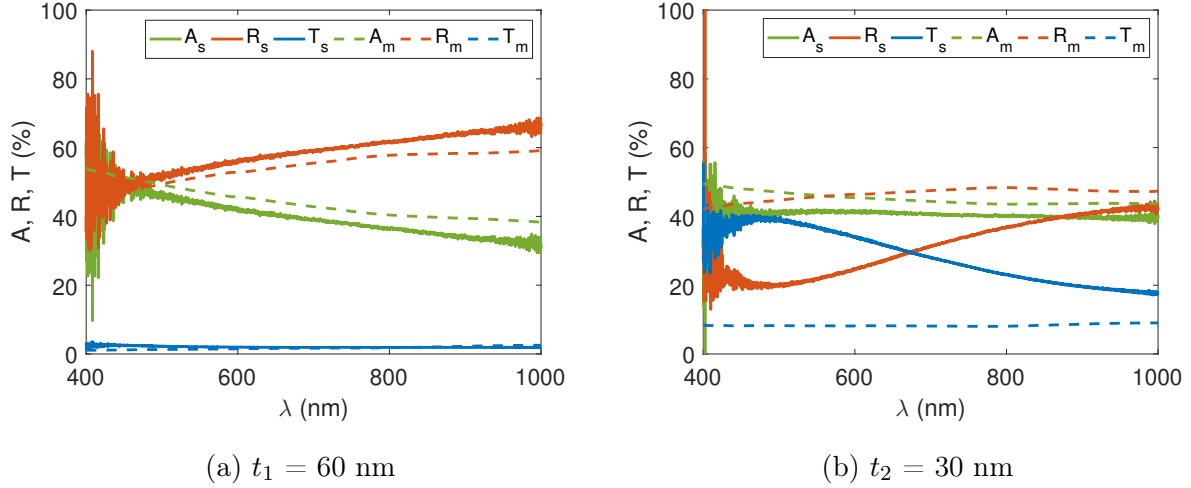
Figure 4.15: Measurements of absorbance, reflectance and transmittance from spectrometry (A_s, R_s and T_s) and from the model based on ellipsometry measurements (A_m, R_m and T_m). The subfigures (a) and (b) represent two different film thickness t_1 and t_2 respectively of sub-stoichiometric TiN$_x$ (N$_2$ flow: 4.9 sccm).

For 60 nm, the measurements in Fig. 4.15a concur with the model. The transmittance is close to 0 over the whole range and reflectance is dominant with a mean value around 60%. In this configuration, efforts should go towards an anti-reflection coating on top of the TiN$_x$ layer as proposed by other groups [68, 69] while a reflector would be unnecessary. This is not the case in Fig. 4.15b when we reduce the thickness of TiN$_x$ by half. The measured transmittance increases almost by a tenfold while reflectance decreases by half. Surprisingly, reducing the TiN$_x$ thickness do not affect the overall absorbance which stays at a constant 40% over the whole range. It has been demonstrated that for MKIDs, the volume of the absorber is inversely proportional to photon sensitivity [11]. Since the absorber must have a minimum surface for a microlens array to focus light at a realistic distance, the only dimension in which we can further reduce the volume is thickness. The TiN$_x$ thickness should not be inferior than 30 nm because otherwise absorbance will start to drop and kinetic inductance will increase to a point where the RF loss can severely impact the resonator Q_i. In the case of a 30 nm thick TiN$_x$ layer, responsivity will be doubled and the use of a reflector with correct optical coupling becomes relevant again. It is also worth mentioning that the modelled transmittance in Fig. 4.15b differs completely from the actual spectrometry measurements. We have compared the evolution of the model with measurements for five different TiN$_x$ layer thickness in Fig. 4.16

(a) Model using the measured $\tilde{n}$ of TiN_x (b) Measurements of TiN_x by spectrometry
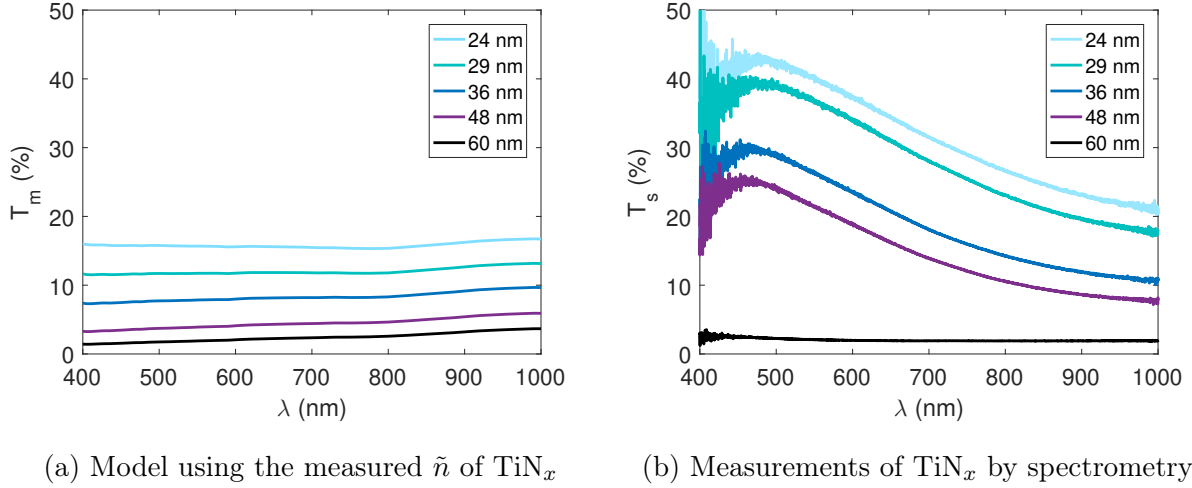
Figure 4.16: Model and measurements transmittance of TiN_x layers with thickness ranging from 24 to 60 nm

The modelled transmittance in Fig. 4.16a is constant over the whole range and seems to increase exponentially with decreased thickness, reaching a maximum of 15% for a 24 nm-thick TiN_x layer. As for the measured transmittance in Fig 4.16, only the 60 nm sample is consistent with the model where transmittance is close to none. Otherwise, for every other sample, the shape of the measured transmittance is closer to stoichiometric TiN in Fig. 4.12 even though the complex refractive index of TiN_x is different. However for the same thickness, the transmittance amplitude of TiN_x is lower than TiN but is still peaking at 45% for a 24 nm-thick layer. We also notice that the transmittance amplitude between samples do not vary consistently probably because of the high uncertainty of the TiN_x crystallographic structure from one deposition to the other. The shape and amplitude discrepancy between the model based on ellipsometry and the spectrometry measurements of TiN_x samples deposited by reactive sputtering has not been reported elsewhere and should be further investigated. We believe that this transmission line model used by other groups as well can only partially describe the optical parameters of TiN_x below a certain thickness because of its unstable crystallographic nature.

4.4 Design of the optical stack MKID geometry using a microwave EM solver

Now that the material and thickness of each layer composing the optical stack has been defined, we have to design the MKID geometry itself to proceed to microwave characterization at cryogenic temperatures. In order to properly design this geometry, we will use the *Sonnet*® ElectroMagnetic (EM) solver that consider the whole MKID structure as a 3D planar circuit. *Sonnet*® is based on method-of-moments analysis and adaptive meshing for refined simulations by taking into consideration cross-coupling and parasitic effects. *Sonnet*® is widely used for MKIDs simulation because of its ability to register the effects of kinetic inductance L_k, a critical parameter inherent to superconductors. The phase and amplitude of MKIDs can be extracted from the S-parameters to compute the expected resonance frequency and quality factors. In this study, the resonator and coupling to the feedline will depend on the stoichiometry of TiN. We will present the two main designs and simulate the influence of the optical stack over the resonator.

4.4.1 Stoichiometric TiN resonator design parameters

The optimized MKID design used for this work is depicted in Fig. 4.17. The resonator is composed of an inductive and a capacitive element and has a total surface area of $275{\times}275$ µm^2. The inductive absorber is shaped into a $42{\times}37$ µm^2 meander, which is the usual geometry that we have well characterized in previous studies. For ease of fabrication, we have decided to pattern 0.7 µm gaps instead of the usual 0.5 µm which should not affect absorption much in the 400-1600 nm range. The meander has 2.5 µm-wide arms extending towards the IDC to connect both elements together. These extensions are also part of the total inductive element as the Cooper pair density is not negligible. The total inductance value from the meander and extensions combined can be estimated by:

$$L_k^{\text{tot}} = L_k \left(\frac{l_m}{w_m} + \frac{l_e}{w_e} \right) \tag{4.14}$$

where $l_m = 470$ µm and l_e are respectively the meander and extensions total length and $w_m = 2.5$ µm and w_e are respectively their widths. If we want to minimize the contribution of the extensions to confine the Cooper pair density in the meander, we have to reduce

the l_e/w_e ratio in 4.14. In this design, the extension arms width will be twice the width of the meander such as $w_e = 2w_m$ and the meander length will be twice the length of the two extension arms combined such as $l_m = 2l_e$. In that case, the extension arms should account for 1/5th of the total detected photons. The capacitor is a large 260×200 µm² IDC with thin 1 µm-wide fingers and 1 µm-wide gaps to suppress TLS noise. It is possible to estimate the capacitance using an analytical equation [49] which gives for the full IDC $C_{\text{IDC}} = 1.5$ pF. These superconducting layers are deposited on a 280 µm thick sapphire substrate with the cleaning process detailed in Sec. 3.1 to ensure that the resonators will have the highest internal quality factors possible.
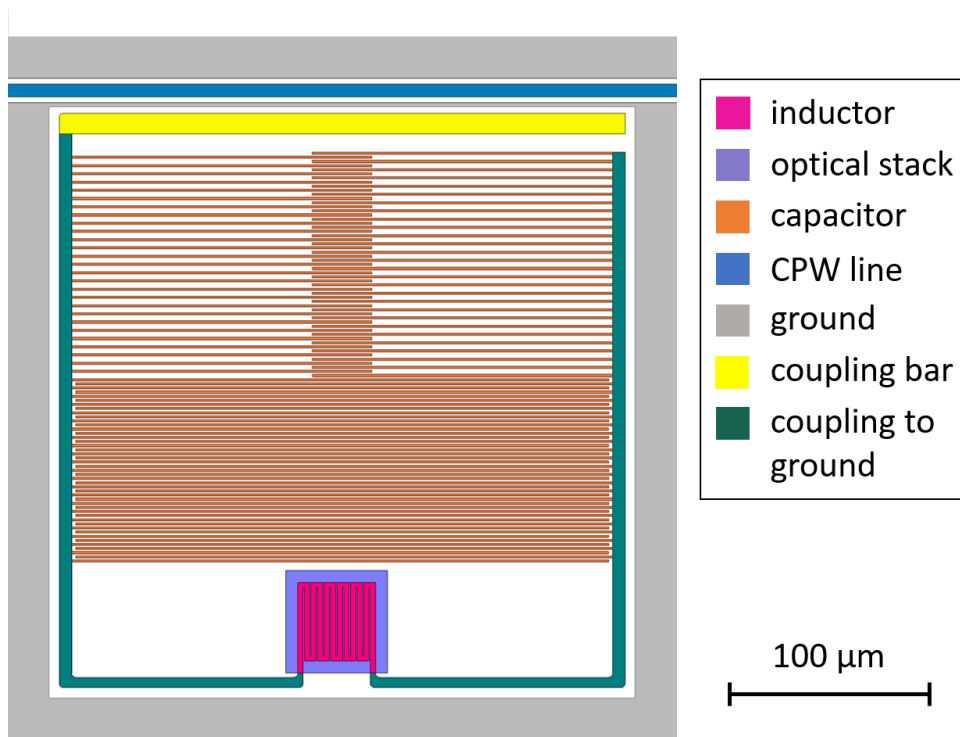
Figure 4.17: Top-view illustration of the MKID design used throughout this work and its coupling to the CPW center strip and ground. All colors are arbitrary and simply here to highlight the different elements.

For the first batch, the material used to pattern the resonator is a 60 nm stoichiometric TiN layer with a N_2 flow of 6 ± 0.1 sccm that corresponds to a critical temperature $T_c = 4.6\ K$. The residual resistivity before the superconducting state can be approximated at room-temperature using a 4-point probe method where a known current is sent through the first two points and the voltage is retrieved by the remaining two points. If we measure

the residual resistivity at temperatures below 10 K once, we can determine the residual resistivity of all the following samples with the RRR to avoid losing time of cooling them down. The measured resistivity at room-temperature is $\rho_{300K}^{TiN} = 325$ µΩ·cm and at temperatures below 10 K is $\rho_n^{TiN} = 270$ µΩ·cm which corresponds to a $RRR_{TiN} \approx 1.2$. Thus, the kinetic inductance per square is $L_k^{TiN} = 12$ pH/□ and the resulting inductance of the whole inductive element computed from Eq. 4.14 is $L_k^{tot} = 2.5$ nH. The analytical resonance frequency of the full-IDC resonator can be computed from Eq. 2.24 which gives $f_0 = 2.6$ GHz. In Fig 4.17, we see in orange the usual and powerful MKID multiplexing method that consists of reducing the length of a specific number of IDC fingers so that each resonator in the 25-pixel array has its own f_0. If we remove a fixed finger length $n_i \Delta l$ for each pixel where n_i is the resonator index, the expected spectral step Δf_0 from simulations will follow a power law. Since Δl and Δf_0 are inversely proportional, it is possible to deduce the corresponding variable $\Delta l(n_i)$ to obtain a fixed frequency step like represented in Fig. 4.18a. This study do not require an optimal multiplexing frequency step but rather to cover a larger spectral window to characterize the evolution of our samples according to frequency. In this design, there are 25 pixels with $\Delta f_0 = 70$ MHz so the total bandwidth is almost 2 GHz.

(a)   (b)
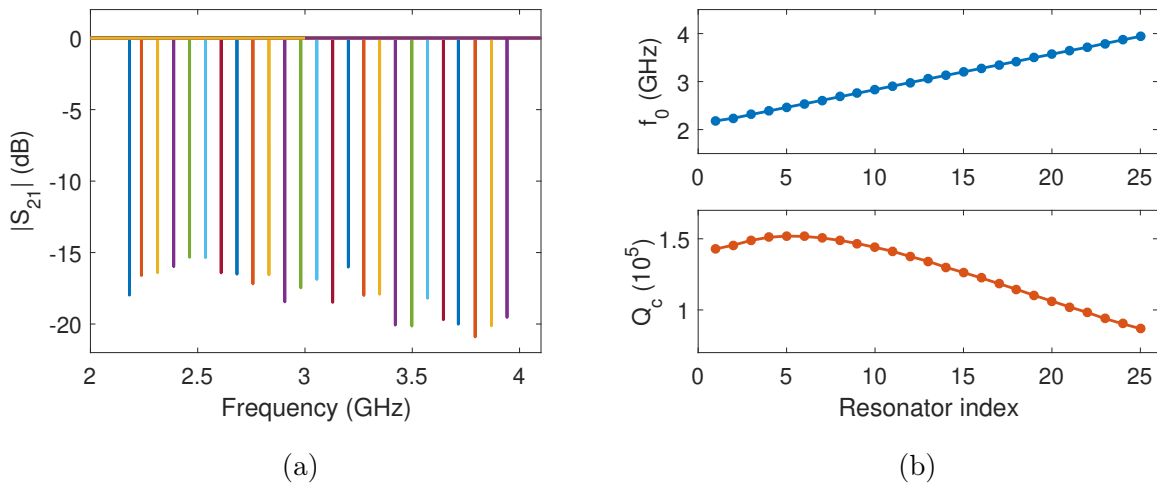
Figure 4.18: Expected f_0, S_{21} and Q_c of the 25-pixel array stoichiometric TiN design from Sonnet simulations with the sapphire substrate dielectric loss tangent set to $\delta = 10^{-6}$. The multiplexing of the resonators is tuned to have a constant f_0 step of 70 MHz.

In Fig. 4.18b, the expected Q_c from simulations was fitted to be between 1×10^5 and 1.5×10^5 which corresponds to the upper limit that we have discussed in previous sections.

The individual Q_c of resonators gets lower with increased frequency because of the weaker electric field as we remove more and more IDC fingers.

4.4.2 Sub-stoichiometric TiNx resonator design parameters

The resonator for the second batch is made of a 30 nm thick sub-stoichiometric TiN layer with a N_2 flow of 4.9 ± 0.1 sccm that we measured to have a critical temperature $T_c \approx 1.67$. This T_c was obtained with a plasma pressure of 0.4 Pa instead of 0.6 Pa after we witnessed a change in our TiN_x thin films parameters over time. Moreover, if we consider the steep change in the TiN crystalline structure as seen in Fig. 3.5, it remains difficult to control the critical temperature if we were to repeat the deposition process with a $\pm$ 0.1 sccm uncertainty on the N_2 flow. This is not critical for our study on 25 pixels but should raise concern when developing large scale arrays. The resistivity at room-temperature is around $\rho_{300K}^{TiN_x} = 267$ µΩ·cm and the resistivity before the superconducting transition that was measured below 10 K is $\rho_n^{TiN_x} = 259$ µΩ·cm, which corresponds to a $RRR_{TiN_x} = 1.03$.

(a) TiN 60 nm-thick absorber

(b) TiN_x 30 nm-thick absorber
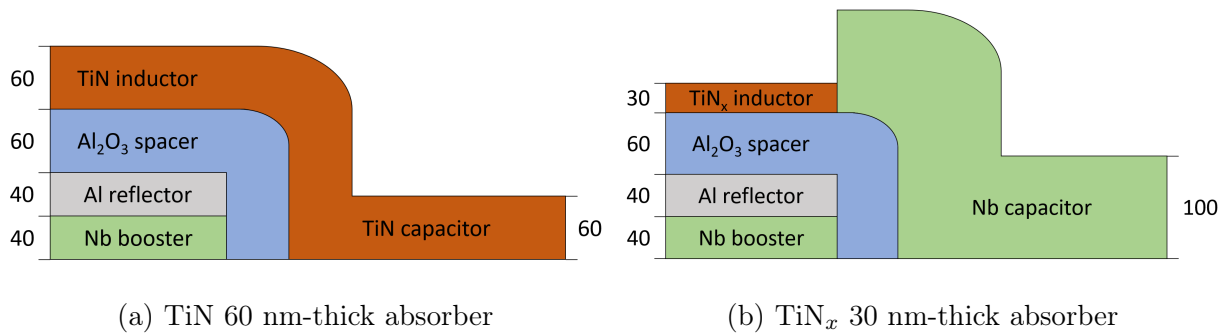
Figure 4.19: Side-view of the two main resonator geometries (all thickness values are in nanometers). (a) The whole LC resonator is deposited in a single 60 nm-thick TiN layer. (b) The TiN_x layer is only used for the absorber because of its higher RF loss. The capacitor is a 100 nm thick Nb layer that overlaps with the inductor during deposition for connection.

The reflector made from aluminium has a low $T_c = 1.2$ K that can induce RF loss and affect the resonator at the normal 300 mK MKID operating temperature because of a non-negligible quasiparticle population. To overcome this issue, we deposit a niobium layer that has a high $T_c = 9.2$ K directly underneath the reflector so that the superconducting

state of Nb is carried over to the Al layer by proximity effect. To maximize this effect, the thickness of the niobium layer must be at least equal to its coherence length $\xi_{Nb} \approx 40$ nm. Since a 40 nm Al reflector has zero transmittance, it was unnecessary to discuss the optical influence of the Nb layer over the stack in previous sections.

(a)   (b)
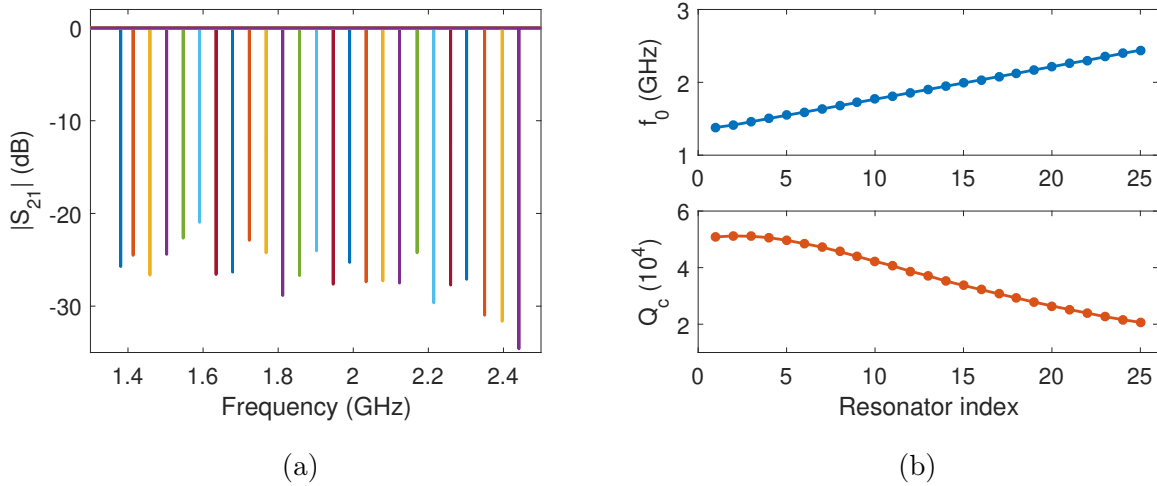
Figure 4.20: Expected f_0, S_{21} and Q_c of the 25-pixel array sub-stoichiometric TiN$_x$ design from Sonnet simulations.

4.4.3   Coupling to the feedline

As discussed in Sec. 2.8.3, we use in this work the compact CPW feedline geometry to excite the resonators. As illustrated in Fig. 4.21, the CPW dimensions have been chosen to ensure the characteristic impedance to be $Z_0 = 50$ Ω.
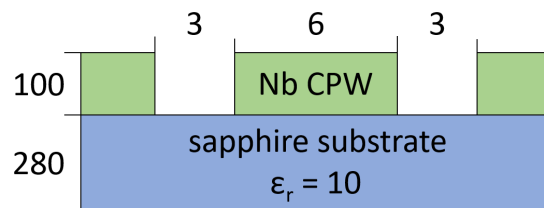
Figure 4.21: Sectional view (not to scale) of the CPW geometry used for all samples in this work and deposited on a sapphire wafer.

The 100 nm-thick Nb layer is deposited on a 280 nm-thick sapphire substrate ($\epsilon_r = 10$) and the CPW central strip is 6 μm wide with 3 μm gaps. In the case of millimeter

MKIDs, the resonator is inductively coupled to the feedline because the inductive surface is usually a tenfold larger than the capacitor. For optical MKIDs, the surface of the inductor is considerably reduced so the main coupling power becomes capacitive as seen in Fig. 4.17. The yellow coupling bar is capacitively coupled to the CPW central strip and accounts for the majority of electric power transferred to the resonator. The coupling to ground around the whole resonator colored in green should not be underestimated as it has a coupling surface three times larger than the coupling bar. For the TiN_x inductor geometry, the increase in kinetic inductance that translates into higher RF loss makes the normal capacitive coupling not enough. One solution that was adopted by other groups is to extend the CPW conductive strip over the ground to directly couple it to the resonator but this method is time-consuming and rather complex as it requires two additional layers to deposit (insulating bridge and conductive extension from CPW to the resonator). Another solution that we have previously proposed for MIM capacitor MKIDs is to remove the CPW ground strip between the central conductive strip and the resonator [74]. This way, we allow for a higher electromagnetic power to be transferred to the IDC capacitor and considerably increase the resonance depth.

4.4.4 Optical stack parasitic capacitor

As presented in Fig 4.22, the different layers beneath the meander that make up the optical stack can be simulated to determine their contribution to microwave loss.
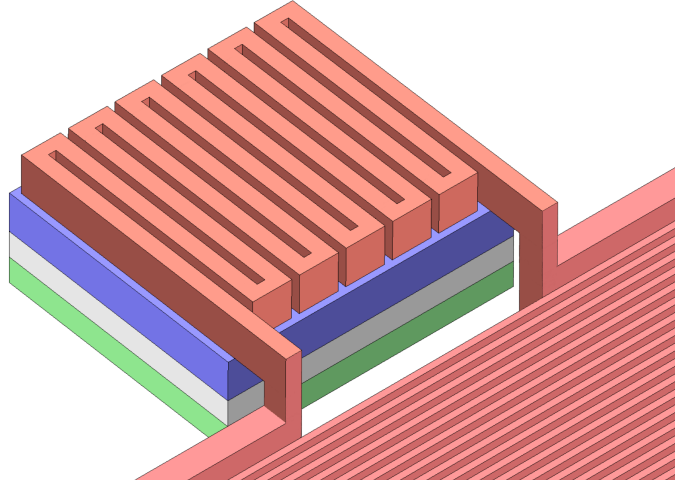
Figure 4.22: 3D geometry of the TiN inductor and optical stack (the layers thickness have been exaggerated for clarity purposes). The TiN meandered absorber rests on the optical stack that consists from top to bottom of: an Al_2O_3 spacer layer, an Al reflective layer and a niobium boosting layer to minimize quasiparticle loss in the low-T_c Al layer through the proximity effect.

We have first simulated the TiN LC resonator by itself for reference in a 2-port system with parameters described in previous sections. We have arbitrary conducted these simulations on the resonator index number 10 which has a computed IDC capacitance $C_{IDC} = 0.86$ pF and a simulated resonance frequency $f_0 = 2.91$ GHz with fitted $Q_c = 1.41 \times 10^5$. If we now introduce a 60 nm-thick Al_2O_3 layer with $\tan \delta = 10^{-6}$ below the inductive meander, f_0 and Q_c are not affected thanks to the low-loss dielectric. However, the addition of the reflector below the dielectric spacer layer lowers the resonance frequency from 2.91 to 2.81 GHz and increases the coupling quality factor from 1.41 to 1.65×10^5 as reported in Table 4.1.

	Resonator TiN 6 sccm	Res. + Al$_2$O$_3$	Res. + Al$_2$O$_3$ + Al	Res. + Al$_2$O$_3$ + Al + Nb
Δf_0 (MHz)	0	-1	-100	-100
ΔQ_c (10^5)	0	0	+0.24	+0.23

Table 4.1: Simulated microwave parameters of the resonator index 10 ($f_0 = 2.91$ GHz, $Q_c = 1.41 \times 10^5$) to measure the influence of the different optical stack layers. Δf_0 and ΔQ_c are respectively the frequency and coupling quality factor difference between the TiN 6 sccm resonator only and the optical stack geometry.

From an electric standpoint, the optical stack can be approached as a parallel-plate capacitor (also known as MIM) where the inductive meander and reflector are respectively the top and bottom plates and the spacer layer is the insulator. Even though the MIM surface here is considerably smaller than the IDC, we have demonstrated that for the same given area, the electric field in MIM is much more stronger than in IDC [74]. The capacitance of this parasitic capacitor can be approximated analytically in terms of plate surface, insulating thickness and dielectric constant or by simulating the MIM geometry on Sonnet from which we obtained $C_{\mathrm{MIM}} = 0.13$ pF [77]. Since the parasitic MIM capacitor is in parallel with the resonator IDC capacitor, we can directly add these two values together to get the total capacitance value of the optical stack resonator which is $C_{\mathrm{tot}} = C_{\mathrm{IDC}} + C_{\mathrm{MIM}} = 0.99$ pF. From this value, we can compute the resonance frequency with the optical stack that shifts to a lower frequency $f_0 = 2.70$ GHz which is in agreement with simulations. The expected surface current density across the resonator at the resonance frequency can be simulated as represented in Fig. 4.23
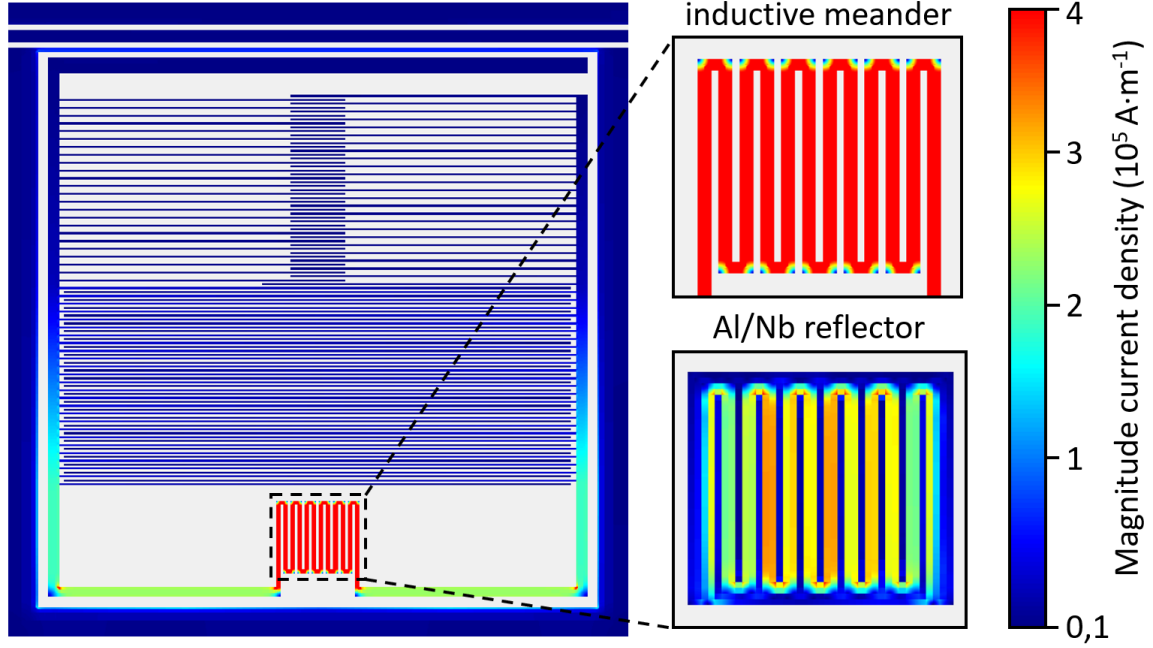
Figure 4.23: Colormap representing the magnitude of the current density J in the pixel at the resonance frequency. Top right: close-up view of the inductive meander where J is the highest. Bottom right: A significant part of the resonator current density is transferred to the reflector where the footprint of the meander is visible.

On the left where the whole resonator is represented, we see that the current density is mainly confined into the inductive element. The average magnitude is around 4×10^5 A· m^{-1} on the meander and is cut by half on the extension arms as designed in Sec. 4.4.1. On the bottom right of Fig. 4.23, the current density on the Al/Nb reflector reveals is shaped into the meander above and reaches up to 3×10^5 A· m^{-1} in magnitude, which is a strong evidence that the parasitic MIM capacitor that arises from the optical stack is not negligible.

4.5 Experimental results for optical stack MKIDs

The optical stack geometry designed in previous sections has been fabricated in our cleanroom using all process described in Sec. 3 and one of the pixel can be seen below in Fig. 4.24
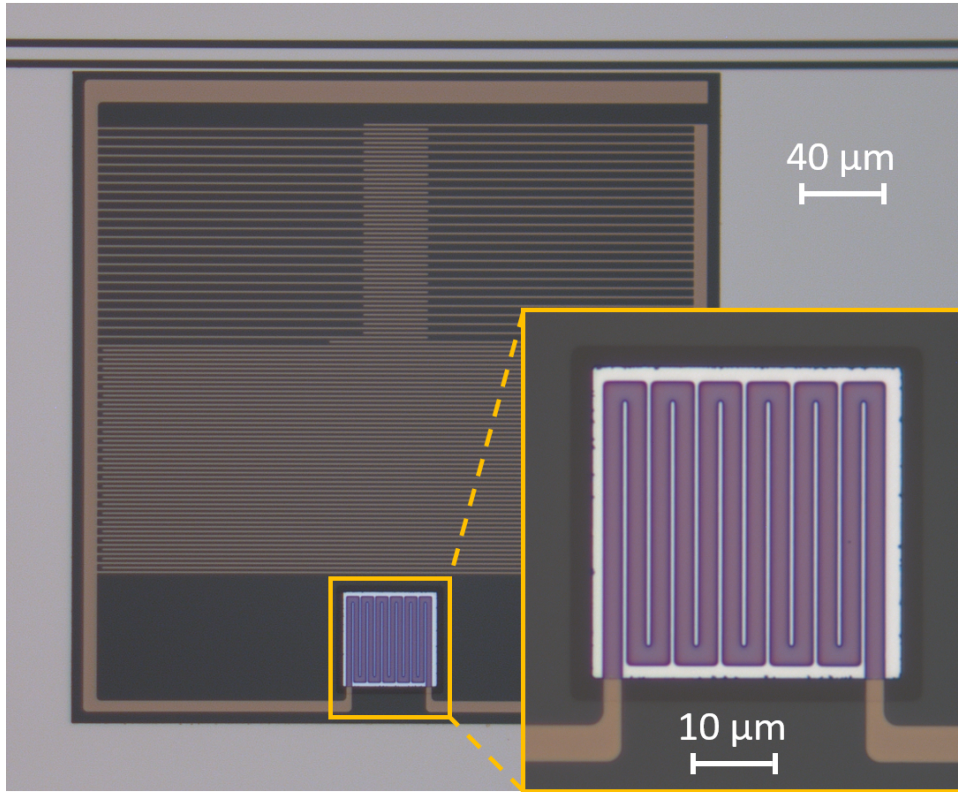
Figure 4.24: Photo taken with an optical microscope of the optical stack design fabricated in our cleanroom. The closeup focuses on the 60 nm thick stoichiometric TiN inductive absorber deposited on top of the Al_2O_3 dielectric and Al reflector. The difference in color between the meander and the rest of the resonator made from the same material is a clear indication that the optical transmittance in TiN is not negligible.

To quantify the influence of each element composing the optical stack, we have fabricated three different geometries: a reference sample on which the resonators have no optical stack (also named *No Diel No Refl*, NDNR), a second sample that has the dielectric spacer layer below the inductor (*Yes Diel No Refl*, YDNR) and a third sample with the whole optical stack (YDYR). The addition of a dielectric layer creates two interfaces (substrate/dielectric and dielectric/superconductor) on which native oxide layers will form because there is no vaccuum continuity between these different process. The amorphous oxide layers are expected to host additional TLS and must be quantified independently with the YDNR sample. We will actually present two batches separately: the first batch has both the inductor and IDC patterned from a single stoichiometric TiN layer like represented in Fig. 4.19a while the second batch also has a stoichiometric TiN inductor but with a Nb IDC deposited after. There will be no discussion concerning sub-stoichiometric

TiN$_x$ as the measured reference and optical stack samples respectively represented in Fig. 4.25a and Fig. 4.25b had shallow resonances that didn't not allow for single-photon mode. However, the higher sensitivity of TiN$_x$ is necessary to obtain a medium energy resolution detector and should be the subject of further investigation.

(a) TiN$_x$ reference

(b) TiN$_x$ optical stack
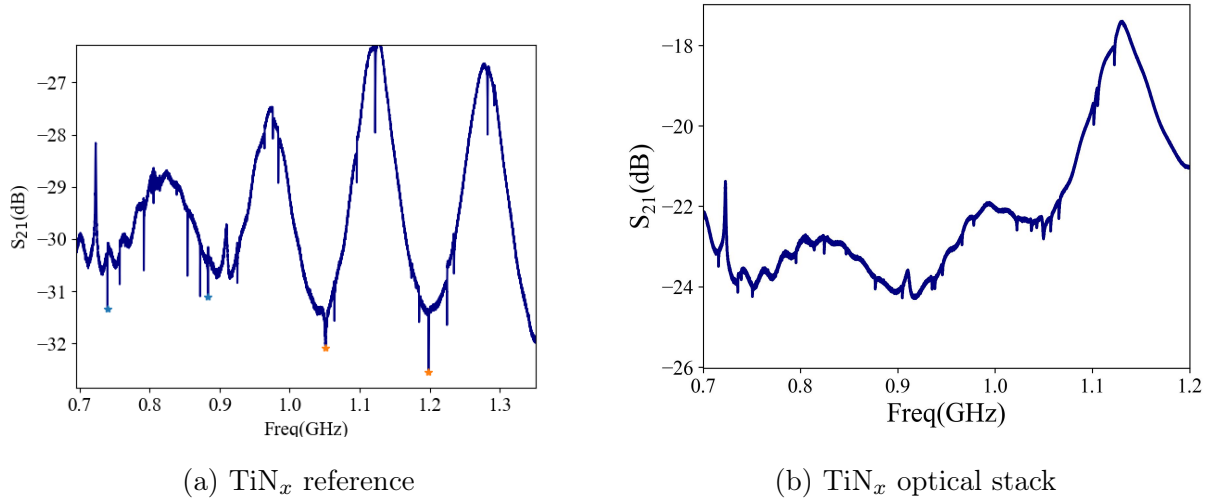
Figure 4.25: Magnitude of S_{21} of (a) the reference sample with TiN$_x$ and (b) the optical stack sample with TiN$_x$.

For the first batch, we will mostly focus on the influence of each layer over the resonator parameters. As for the second batch where single-photon mode was obtained on the reference, we will discuss what has prevented us to count photons on the optical stack sample despite having high quality factors. All samples inside a same batch have been fabricated in the shortest interval of time possible under the same conditions and characterized with the same readout electronics and illuminated with the same optical power. In the following comparison results where each sample has 25 pixels, we will only compare the response of one resonator per sample.

4.5.1 First batch in-dark measurements

Before characterizing the MKIDs response to light pulses, we can extract from the resonators that are in the dark several useful noise-related parameters. By comparing these parameters between the three different geometries listed above, we will have quantitative information regarding the influence of the optical stack layers over the resonator. The value of Q_i is plotted in Fig. 4.26 as a function of bath temperature.
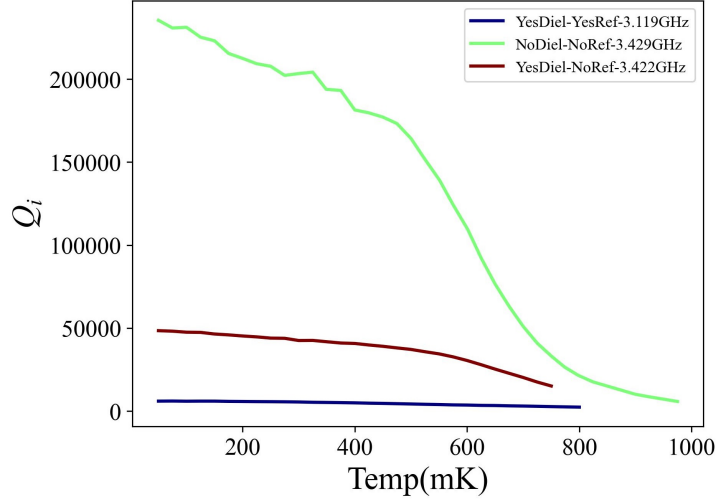
Figure 4.26: Comparison of the internal quality factor of one resonator in each sample with similar f_0 as a function of bath temperature measured at -100 dBm.

The reference sample NDNR has a high $Q_i \approx 200,000$ at the usual operating temperature with a total $Q = 45,000$. As expected, Q_i decreases with increased quasiparticle population at higher temperatures. Now, if we compare it with the YDNR where we only deposited dielectric below the inductor, the Q_i has dropped by a factor of 4 but is still at an acceptable 50,000 at low temperatures with a total $Q = 30,000$. It shows that the sole addition of a compact, low dielectric tangent loss Al_2O_3 layer deposited by ALD can degrade the resonance. This has not been addressed by other groups that demonstrate only by simulations the improvement of optical coupling with the use of dielectric layers [68, 69]. Finally, the optical stack sample YDYR has a very low $Q_i < Q_c$ of around 10,000 with a total $Q = 8,000$ which makes it hard to properly characterize. The reflector on this sample only consists of an Al layer without the Nb below which may explain the considerable RF loss. The sample with the Al/Nb reflector discussed in Sec. 4.4.1 has since been fabricated and measured with high quality factors. The fractional frequency shift shown in Fig. 4.27 also reveals some important behaviour.
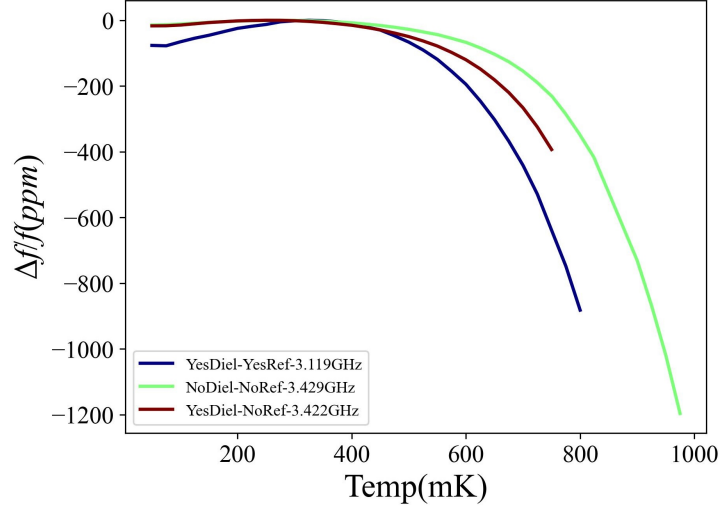
Figure 4.27: Comparison of $\Delta f/f$ as a function of bath temperature measured at -100 dBm.

For NDNR and YDNR, the evolution of $\Delta f/f$ is similar with almost no frequency change up until $T_c/10 = 400$ mK where the quasiparticle density finally starts to increase as expected by the Mattis-Bardeen theory [47] and affects L_k which in turn shifts f_0 to lower frequencies. However for YDYR, $\Delta f/f$ first starts to shift to higher frequencies before following the same behaviour as the two other samples at 400 mK. This evolution at lower temperatures is the influence of TLS over the resonator supported by the model of Eq. 2.41 and was already observed for TiN covered with SiO_x [78] as well as one of my previous samples where the optical stack consisted of TiN, Al_2O_3 and Au/Nb [77]. The particular temperature at which the $\Delta f/f$ changes direction is commonly called the TLS turning point and is around 250 to 300 mK in our stoichiometric TiN samples. Using a signal generator, we can now measure the frequential noise of all three samples between 1 and 10^6 Hz to precisely determine the contribution of each noise source. The comparison between the three geometries is represented at 50 mK in Fig. 4.28a and at 400 mK in Fig. 4.28b and was normalized by the square of their individual resonance frequencies to remove the pixels spectral dependance.
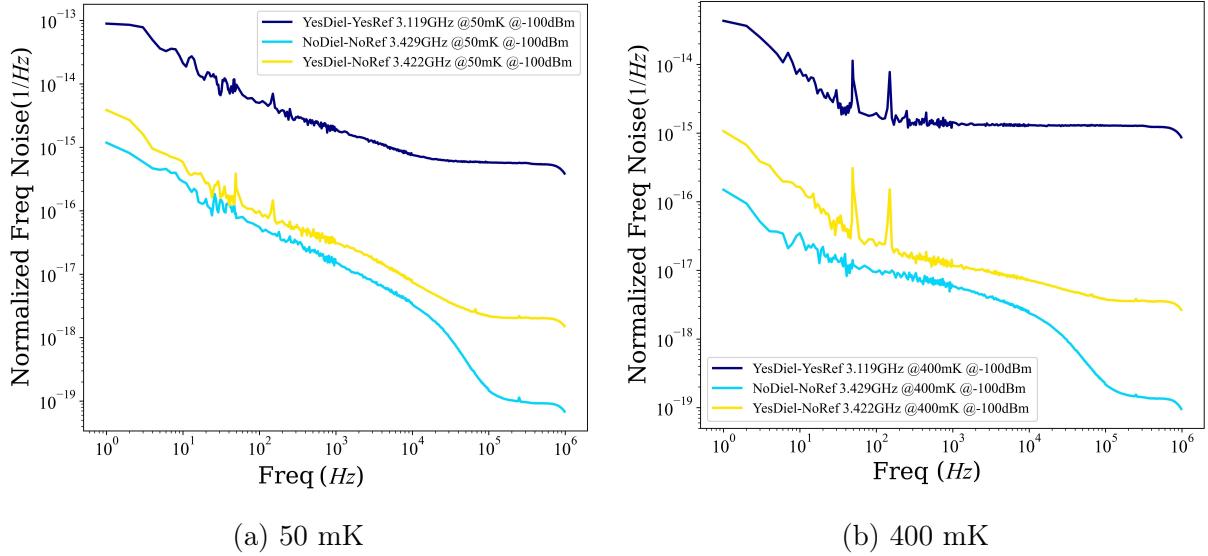
Figure 4.28: Normalized frequential noise of one pixel in each of the three samples measured at -100 dBm input power at (a) 50 mK where TLS is dominant and (b) at 400 mK where TLS is saturated.

As expected, the overall lower spectral density of noise is obtained with NDNR. The addition of the dielectric in YDNR raises the frequential noise by less than an order of magnitude. The noise in YDYR is at least two orders of magnitude more than the reference sample which could be partly explained by its very low Q_i. The noise between 10^2 and 10^4 Hz at 50 mK in Fig. 4.28a has this steep $f^{-1/2}$ slope characteristic of TLS supported by Eq. 2.41 and is similar in all three samples, which indicates that TLS is present whether there is an optical stack or not. In Fig. 4.28b, at 400 mK, the frequential noise of NDNR is around one order of magnitude less with an average noise of 10^{-17} W·Hz$^{-1/2}$ and the TLS slope has flattened to $f^{-1/4}$. The noise level in YDNR however has not lowered as much and this offset might be explained by hot phonons at 400 mK trapped inside the Cooper-pair-hosting inductor that are not able to propagate to the substrate because of the acoustic mismatch created by the Al$_2$O$_3$ dielectric layer in-between [65, 79]. For YDYR, only the $1/f$ and readout noise floor are recorded as the resonance is non-existent at this temperature: it is comparable to measuring the phase noise off resonance like shown in Fig. 2.11. If YDYR had deeper resonances, we would expect it to follow the same behaviour as the two other samples.

4.5.2 First batch illumination response

In this section, we will present the detector's response to short light pulses with the setup detailed in Sec. 3.8. We illuminate the sample using the 405 nm laser diode with the same 4 pW power for each sample and different pulse widths ranging from 50 to 200 ns. Since each sample has very different quality factors, we have represented the pulse response in Fig. 4.29 in terms of frequency to remove the Q dependence. All resonators are 60 nm thick stoichiometric TiN 6 sccm with similar resonance frequencies.
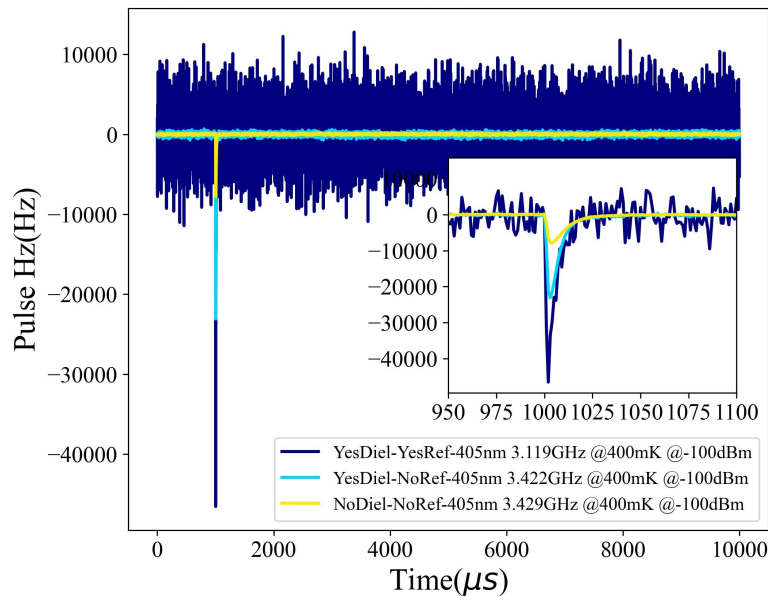
Figure 4.29: Averaged response of a 100 ns pulse normalized by Q for one resonator in all three samples with TiN 6 sccm at 400 mK and -100 dBm input power.

The NDNR sample in yellow has the lowest pulse response as well as the lowest noise which is expected from its high T_c. The addition of the dielectric in YDNR has increased the response by a factor of 3. This could confirm the role of the dielectric acting as a barrier for hot phonons generated by the recombination of quasiparticles inside the inductor after a photon event. Instead of easily propagating to the substrate to reach a fast thermal equilibrium, the acoustic mismatch between layers is trapping hot phonons in the inductor that have enough energy to break more Cooper pairs, resulting in a cascading effect. As for the optical stack YDYR, the shift is five times larger than on the reference sample but the noise also scales accordingly. This larger response can either be due to the same phonon trapping explained earlier or simply thanks to the improvement of optical

coupling with the reflector. For the latter, it is difficult to confirm without the single-photon response from which we would extract the possible quantum efficiency increase between NDNR and YDYR. In any case, the full optical stack sample do not offer a better SNR than the reference in these conditions but we believe that reproducing this study with a more sensitive material for the absorber could settle the actual optical stack performance.

4.5.3 Second batch in-dark measurements

After characterizing the first batch, we were confident that single-photon response could be reached with a few changes. First, we decided to deposit 30 nm thick TiN inductors instead of 60 nm to increase the sensitivity. However, a thinner layer means a higher kinetic inductance and thus more loss. To counteract this, we have made two changes already discussed in Sec. 4.4.2 originally intended for TiN_x samples: the first change is the IDC that is deposited in Nb to prevent having additional RF loss as well as remove detection in the extension arms, and the second is the removal of the CPW ground plane separating the resonator to the center strip to increase coupling to the feedline [74]. Only the reference that we will refer to as NDNR2 and the full optical stack YDYR2 samples were fabricated since the dielectric layer influence has already been established. We have obtained 25 high-Q resonances out of 25 with NDNR2 (cf. Fig 2.8) and 15 with YDYR2 as shown in Fig. 4.30a. We believe that an over-etching of the Al_2O_3 layer may have caused shorts between the reflector and resonator on some pixels. This incident will have no influence whatsoever on the remaining 15 pixels which show good quality factors.
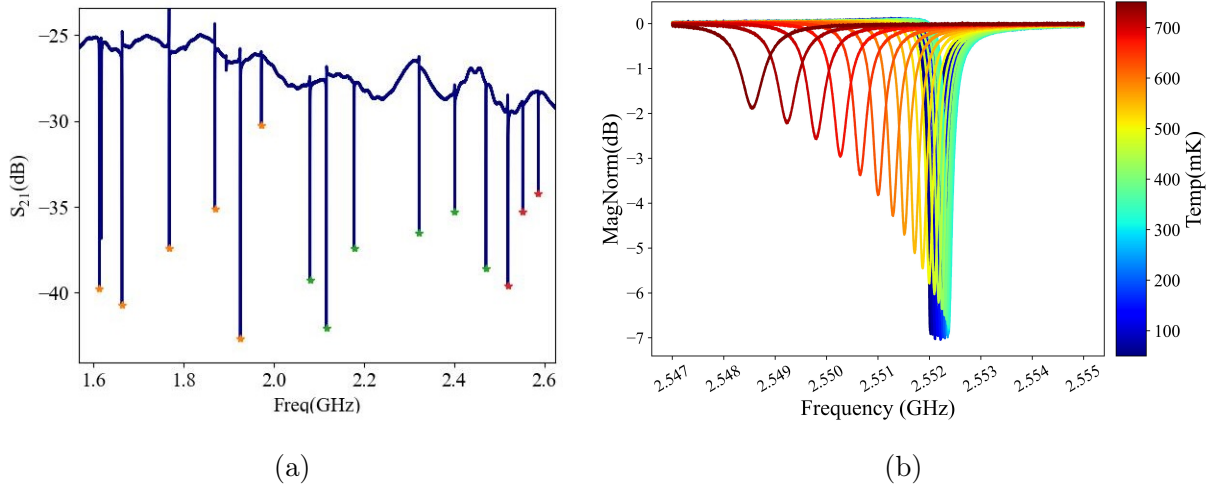
Figure 4.30: (a) Magnitude of S_{21} at 50 mK for YDYR2 where 15 deep resonances can be observed. (b) Normalized magnitude of the resonator with $f_0 = 2.55$ GHz as a function of temperature. The influence of TLS is seen from 50 to 300 mK like observed in Fig 4.27. The resonance is still 2 dB deep at 700 mK.

When comparing the transmission of YDYR2 in Fig. 4.30a to the reference in Fig. 2.8, neither the frequency range nor resonance depths have significantly changed. This confirms the small capacitance contribution that the optical stack parasitic capacitor is adding to the total resonator's capacitance. We can also compare the internal quality factors of both NDNR2 and YDYR2 as well as their fractional frequency shift respectively presented in Fig. 4.31a and Fig. 4.31b.
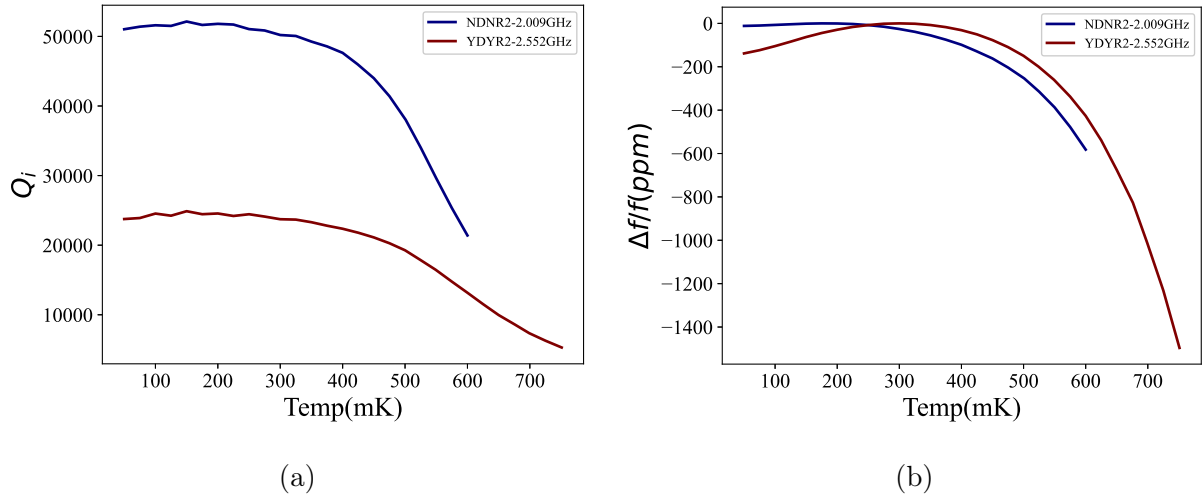
Figure 4.31: (a) Internal quality factors and (b) fractional frequency shift as a function of temperature for NDNR2 and YDYR2.

As expected, the Q_i is reduced with the addition of the optical stack and the evolution of $\Delta f/f$ in YDYR2 as a function of temperature follows the same two-stage behaviour as YDYR in Fig. 4.27. A weak non-saturating electric field may reside in the optical stack parasitic capacitor that would increase TLS. This would explain the larger frequential noise compared to the reference seen in the first batch (cf. Fig. 4.28b) as well as here in Fig. 4.32. The frequential noise increase might also be due to the two additional interface in the optical stack that have suffer uncontrolled oxidation between deposition process and probably have nanometer-thick amorphous layers that host TLS. In this configuration, it is not possible to precisely determine the individual contribution of both the parasitic electric field and amorphous layers to the global noise increase.
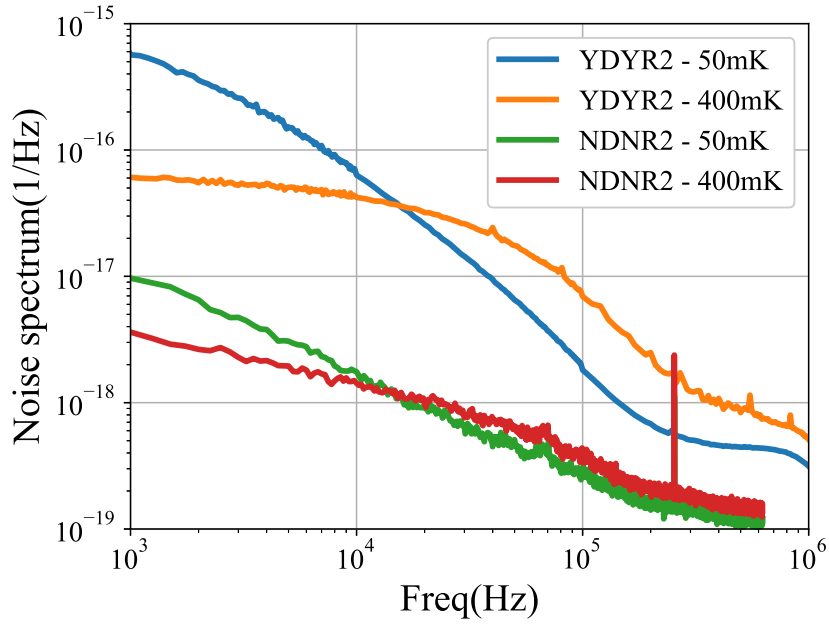
Figure 4.32: Normalized frequential noise at -90 dBm of one pixel in both the reference NDNR2 and the optical stack YDYR2 at 50 and 400 mK.

In any case, the addition of the optical stack has undeniably increased the frequential noise. It is also worth noting that for the reference sample, the noise spectrum level varies only slightly with temperature. For YDYR2, the 10^3 Hz noise at 50 mK is an order of magnitude higher than at 400 mK due to the non-saturated TLS whose signature is this $f^{1/2}$ steep slope represented in blue.

4.5.4 Second batch illumination response

Thanks to optimal filtering explained in Sec. 3.9, the second batch reference sample NDNR2 based on the design detailed above with a 30 nm-thick stoichiometric TiN has given us single-photon response at 405 nm as seen in Fig. 4.33.
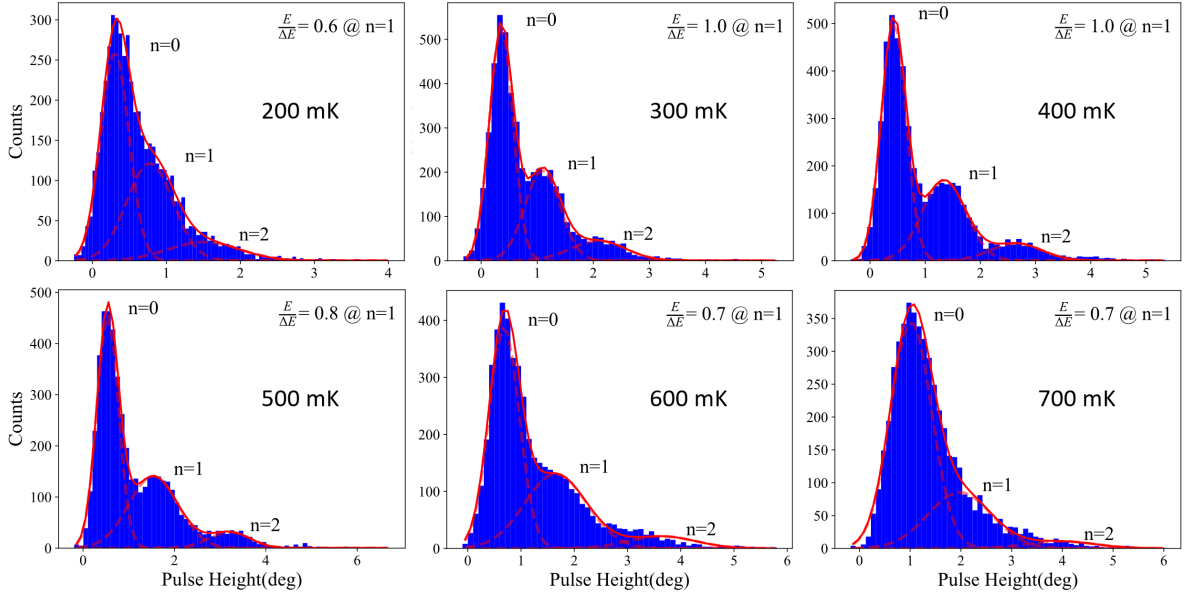
Figure 4.33: Pulse response statistics at -85 dBm of NDNR2 at different temperatures that follow the photon-noise Poisson distribution. The 0-photon peak corresponds to a dark count arising from different noise sources such as generation-recombination or TLS. The 1-photon and 2-photon peaks are clearly distinguishable between 300 and 500 mK. This is the first photon counting ever reported with stoichiometric TiN.

While the energy resolution is very low, we are the first to demonstrate that stoichiometric TiN can indeed count optical photons. We believe that the combination of a low dielectric loss crystalline sapphire substrate, drastic cleaning process and the deposition of TiN at very-high vaccum (10^{-8} mbar) have been key towards achieving this goal. Fig. 4.33 also reveals a clear optimum at around 400mK. At lower temperatures, the energy resolution decreases because of TLS noise and at higher temperatures, it decreases because of thermally-excited quasiparticles. Usually, for low-T_c multi-layer Ti/TiN or sub-stoichiometric TiN$_x$, the operating temperature cannot exceed 100 mK and the use of an ADR is necessary. In our case with NDNR2, photon counting is still possible up to 500 mK, opening up new perspectives for higher-temperature photon counting with less-costly cryostats. If the optical stack can increase the energy resolution, the high-resistivity and uniformity of stoichiometric TiN might compete again with other materials. Most of the resonators in this reference sample have shown saturation at unusually high readout powers which has allowed us to obtain the single-photon mode at -85 dBm. While reading

25 pixels at this power do not cause any issue, the cryogenic LNA cannot handle this load for kilopixels arrays. In Fig. 4.34, we have represented the averaged pulse height from 0, 1 and 2 photons events that appears to be linear as shown by the inset.
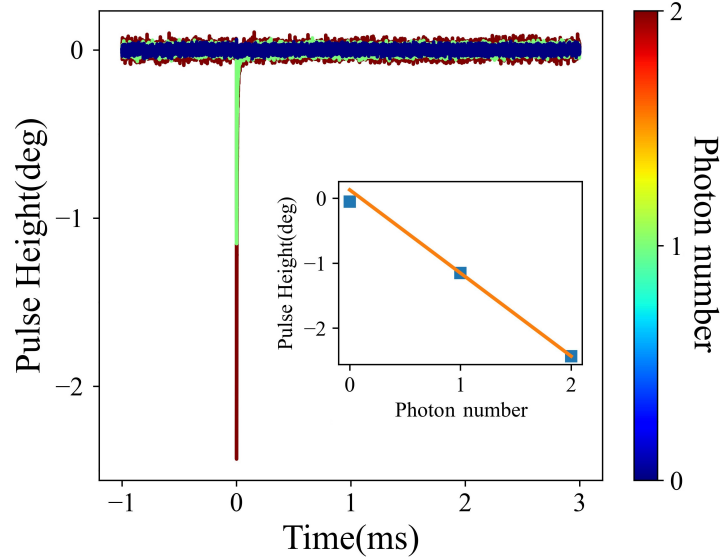
Figure 4.34: Averaged time-domain response to 405 nm pulses at 300 mK and -85 dBm. The inset shows the linearity between the photon number and the phase shift recorded.

As for the second batch optical stack YDYR2, we were not able to obtain single-photon response. We strongly believe that this is related to the frequential noise increase caused by the optical stack and unfortunately no quantum efficiency comparison can be made. We can however compare the pulse response of both samples at different temperatures in Fig. 4.35
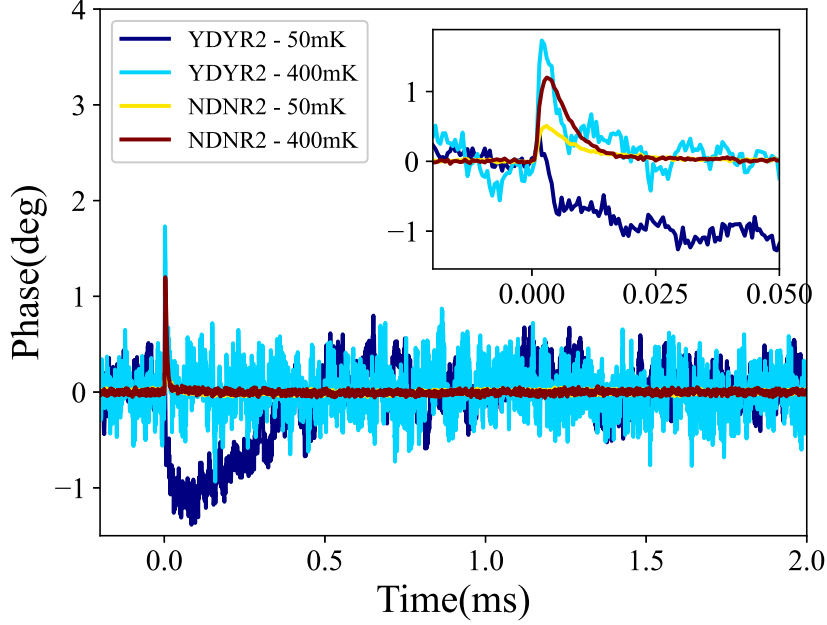
Figure 4.35: Averaged time-domain response to 405 nm pulses at -100 dBm with two different temperatures represented 50 and 400 mK.

Even though for both samples the phase shift induced by photons is on the same order at 400 mK, the noise in YDYR2 is much more prominent. The unusual inverse phase response at 50 mK for the optical stack shown in dark blue is an unexpected phenomenon discovered during this work and will be the main concern of Chapter 5. We have also investigated a possible proximity effect caused by the reflector Al and/or Nb layers that may have modified the TiN inductor relaxation time but the quasiparticle lifetime of NDNR2 in Fig. 4.36a and YDYR2 in Fig. 4.36b are comparable.

(a) NDNR2
(b) YDYR2
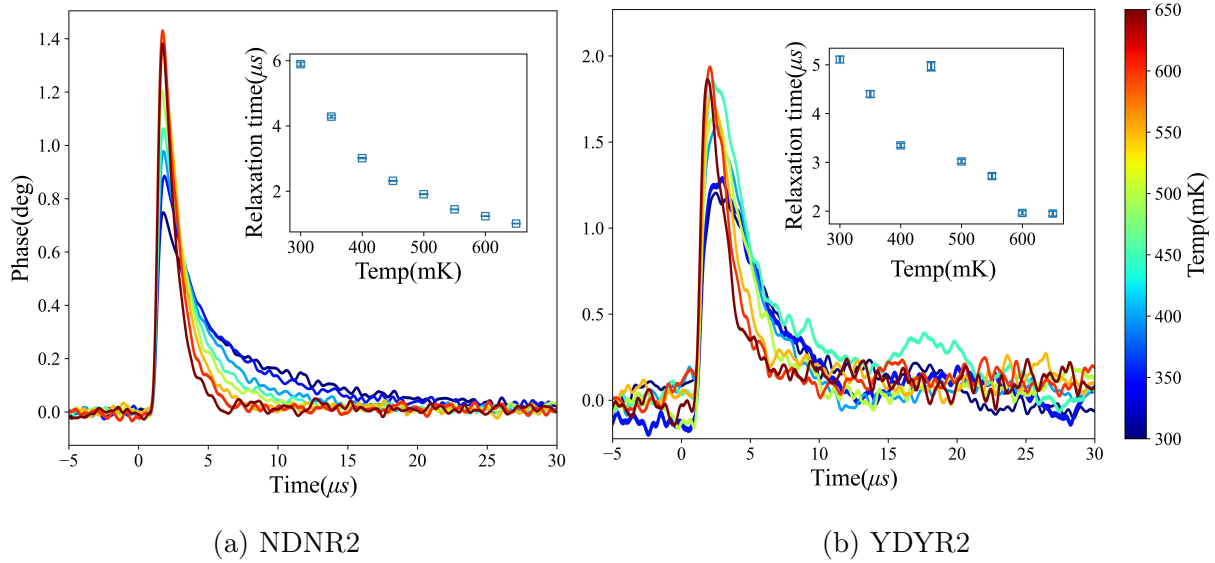
Figure 4.36: Averaged time-domain pulse response comparison between the reference and optical stack samples as a function of temperature. In both case, the relaxation time is close to the resonator response time which should be avoided but has still proven single-photon detection for NDNR2. As for YDYR2, the larger noise may be the reason we have not witnessed single-photon response.

Note that at lower temperatures, $\tau_{\mathrm{qp}} \approx \tau_{\mathrm{rsp}}$ which is not optimal for detection since some quasiparticles will recombine faster than the MKID response time. We have nonetheless demonstrated single-photon counting on NDNR2 and thus cannot be the limiting factor for YDYR2. Instead, we suppose that the optimal filtering is not powerful enough to isolate the single-photon response from the resonator large noise.

Chapter 5

Investigation of a possible MKIDs phonon-based detection

The normal MKIDs detection principle through the change of kinetic inductance is well covered in literature. In a superconducting thin film lithographed as a LC resonator where a RF signal is applied, electrons in Cooper pairs are accelerated with no dissipation and gain momentum that translates into kinetic inductance. An external perturbation such as a photon with enough energy can break Cooper pairs into quasiparticles that scatter off and change the total kinetic inductance, usually quantified by measuring the phase shift of the resonator. At the usual MKID operating temperature $T \approx T_c/10$, TLS becomes dominant and hinder on this kinetic-inductance-based detection [43]. However, during this work, we have measured on all of our high-T_c TiN 6 sccm resonator samples an anomalous response at temperatures lower than the usual operating temperature. Since this phenomenon is TLS dependant, we argue that we could locally amplify TLS where the Cooper pair density is the highest to increase the phonon-based response as a mean of detection [80]. We carried out this investigation on the same array design of 25 lumped-element TiN 6 sccm MKIDs detailed in Sec. 4.4.1.

5.1 The anomalous TiN phase response

5.1.1 General description

When illuminated with a short pulse through an optical fiber, we reported a second phase shift going in the opposite direction directly after the one attributed to Cooper pair breaking. This inverse phase response only appears at $T \leqslant T_c/20$, far below the normal operating temperature, and gets larger as the temperature bath gets lower. This transient phenomenon has only been observed in stoichiometric TiN layers ($T_c = 4.6$ K) as it requires to cool down the samples at temperatures below 250 mK. At this TLS temperature turning point, the phase shift of the phonon response is still low and its amplitude increases rapidly with decreasing temperature. If we want to consider this phenomenon as a mean of detection, we set to characterize the stoichiometric TiN inverse pulse response down to $T_c/100$, which is not feasible with lower T_c materials like substoichiometric TiN_x due to cryostat cooling limitations.
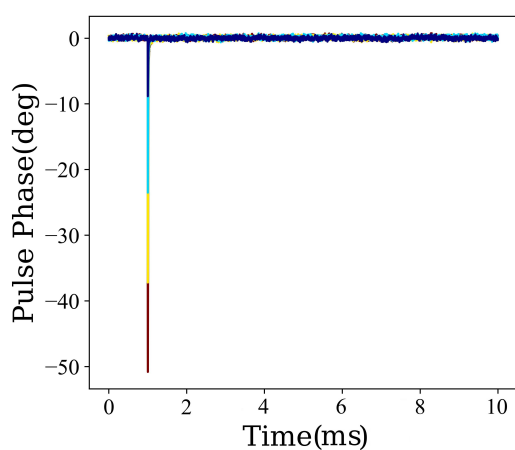
(a) Time domain, $T = 400$ mK
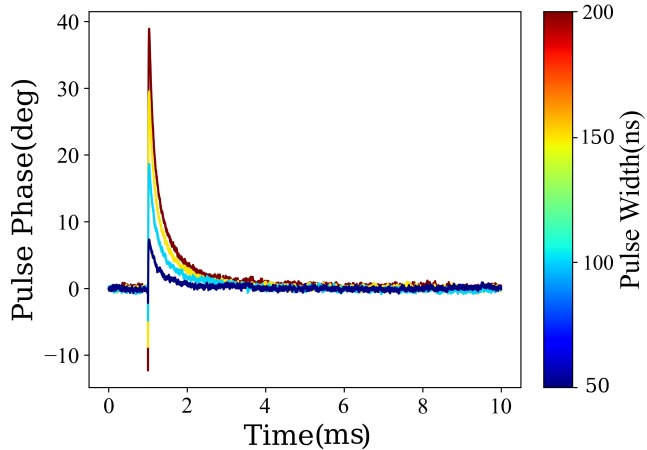
(b) Time domain, $T = 50$ mK
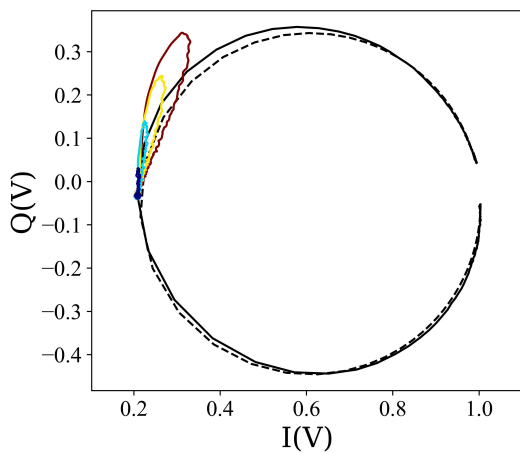
(c) I-Q, $T = 400$ mK
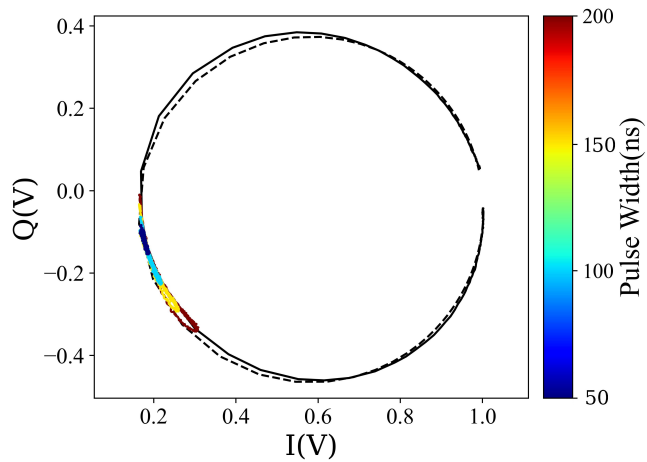
(d) I-Q, $T = 50$ mK

Figure 5.1: Averaged pulse response for different illumination pulse width of a TiN 6 sccm MKID resonator ($f_0 = 3$ GHz, $Q_i \approx 10^5$) with a total attenuation on the path of -100 dBm. The optical pulse is sent at t = 1 ms. (a) At the normal MKID operating temperature $T_c/10$, the usual short-lived pulse response attributed to Cooper pair breaking is observed. (b) For the same resonator, at $T_c/100$ well below the TLS turning point, a longer anomalous inverse pulse response attributed to phonon-TLS interaction is observed with an amplitude on the same order as the normal pulse response in (a). The normal response comes with increased loss from quasiparticles that translates into a change in radius in the I-Q plane of (c) whereas the inverse pulse stays along the resonance circle in (d) which supports a non dissipative phonon-related phenomenon.

Following the illumination with short optical pulses at $\lambda = 405$ nm of our MKID array without the optical stack (TiN 6 sccm LC resonator only), we measured as expected in Fig. 5.1a the usual pulse response attributed to Cooper pair breaking around the normal operating temperature $T_c/10 \approx 400$ mK. However, if we decrease the cryostat bath temperature below the TLS turning point measured at $T = 250$ mK in our films, the anomalous pulse response going in the opposite direction is observed in Fig. 5.1b. The time scale is identical in both figures to highlight the larger inverse pulse relaxation time. The normal quasiparticle recombination time is around $\tau_{\mathrm{qp}} \approx 50$ µs whereas the inverse pulse relaxation time that we will later define as τ_{th} is an order of magnitude longer and vary significantly with different pulse widths. A similar negative response has previously been observed in ALD deposited TiN films but under constant optical illumination [81]. If we now observe in Fig. 5.1c the pulse response evolution in the I-Q plane that shows both the resonance phase and amplitude, the rise edge sees a change in angle while going towards the center of the resonance circle because quasiparticles increase kinetic inductance and thus RF loss. The pulse decay then goes back to the steady state after quasiparticle recombination. In Fig. 5.1d, we observe the same quasiparticle behavior directly followed by the inverse pulse. The IQ plane reveals that the inverse pulse decay goes back to the stable state along the resonance circle which indicated that all quasiparticles from the optical pulse have already recombined by that point. We can also study at different temperatures the MKIDs PSD presented in Fig. 5.2.
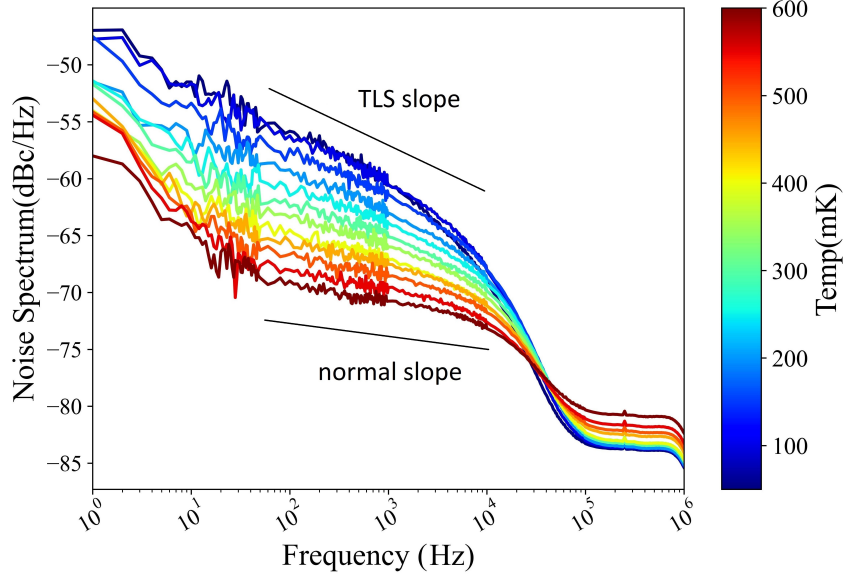
Figure 5.2: Noise spectrum of the resonator presented in Fig. 5.1 with the same -100 dBm total attenuation for bath temperatures ranging from 50 mK to 600 mK. The noise signature of TLS is apparent between 10^2 and 10^4 Hz where the slope gets steeper with decreasing temperature.

Starting at lower frequencies ($<10^2$ Hz), the spectrum is dominated by $1/f$ noise. If we jump to frequencies above the resonator roll-off ($>10^5$ Hz), we observe the readout noise increasing with bath temperature as predicted by Eq. 2.40. In our case, the region of interest is between 10^2 and 10^4 Hz as it is dominated by the MKIDs intrinsic noise. The PSD in this region is inversely proportional to the bath temperature. At 10^4 Hz, the noise increases from -70 dBc/Hz at 600 mK to -60 dBc/Hz at 50 mK. The slope also gets steeper with lower temperatures, which is a strong evidence of TLS noise as supported by Eq. 2.43. Below a certain temperature and at low readout power, the TLS mostly present between the MKID layer and the substrate is no longer saturated and will cause variations in the resonance frequency that hinder on detection. This TLS turning point is easily identifiable when looking at the fractional frequency shift $\frac{f-f_0}{f}$ as a function of temperature presented in Fig. 5.3
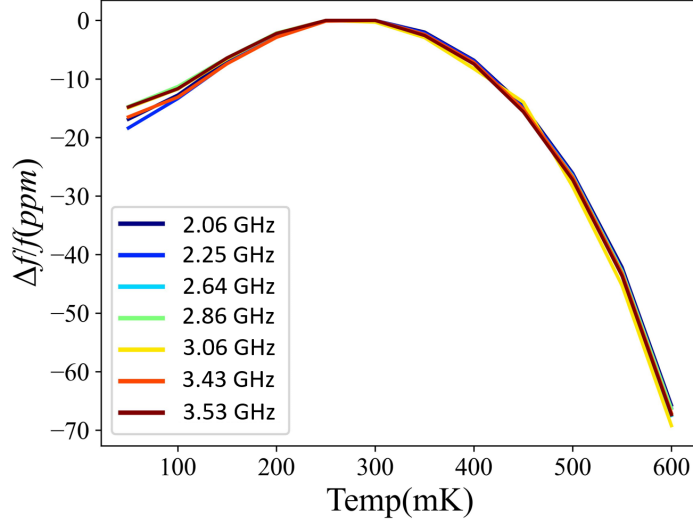
Figure 5.3: Fractional frequency shift as a function of bath temperature of different pixels in the array at -105 dBm attenuation.

There is a striking similarity across the spectrally different pixels (index 0 and 21 have their respective resonances at 2 and 3.5 GHz). Between 50 and 300 mK, the fractional frequency shift is dominated by the TLS noise that is inversely proportional to temperature as suggested by Eq. 2.41, so the resonance point shifts to higher frequencies. Above 300 mK, TLS is saturated and the normal increase in quasiparticle density is responsible for the shift to lower frequencies. The lowest value of $\Delta f/f$ corresponds to the TLS turning point temperature that seems to be around 250-300 mK in our samples but can vary from one material to the other. If we now compare the frequency noise between the different pixels, we can isolate a frequency at which TLS is dominant (see Fig. 5.2) and study its evolution as a function of temperature in Fig. 5.4a and input power in Fig. 5.4b. The frequential noise has been normalized by the f_0 of each pixel to remove the resonator spectral dependance.
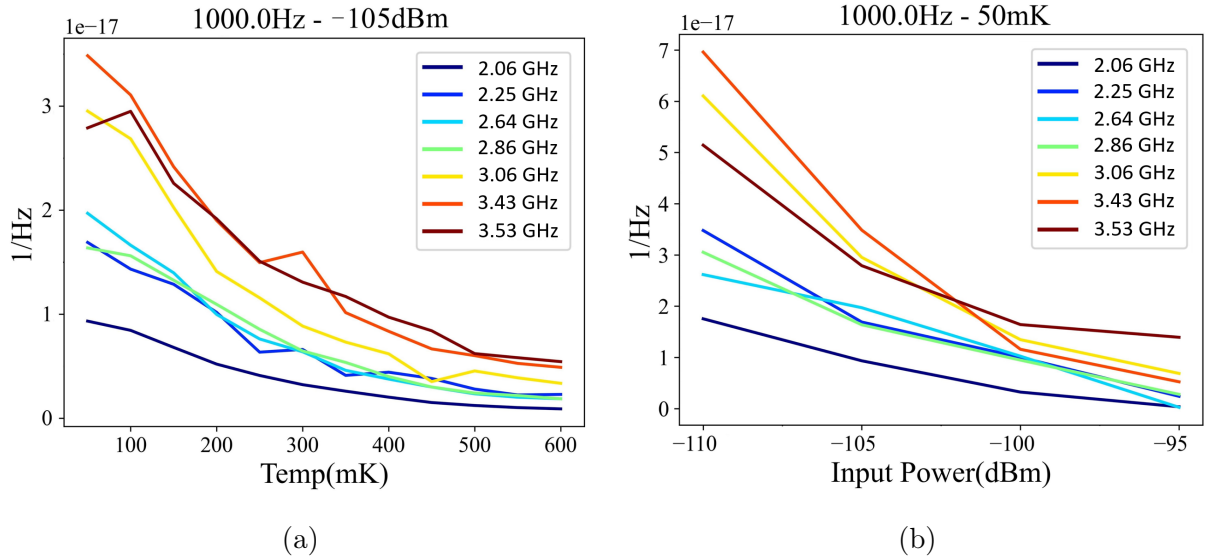
Figure 5.4: Normalized frequency noise at 10^3 Hz where the TLS signature is present for different pixels as a function of (a) temperature at -105 dBm and (b) input power at 50 mK.

As expected, the normalized frequential noise at 10^3 Hz decreases rapidly when increasing temperature and input power. However, both figures still shows some kind of spectral dependance as the pixels with higher resonance frequencies tend to have a higher noise level. The resonators all have the same IDC size but with a different number of fingers for multiplexing (see Sec. 2.8.2). The pixels with higher resonance frequencies have less fingers in their IDC and thus a weaker electric field which increases the TLS spectral density as supported by Eq. 2.43.

5.1.2   Pinpointing the inverse pulse origin

In order to pinpoint the origin of this inverse pulse, we have fabricated the same sample described in the previous section under the same conditions but this time we have covered the inductive absorber of each MKID with a shielding Niobium layer as seen in Fig. 5.5.
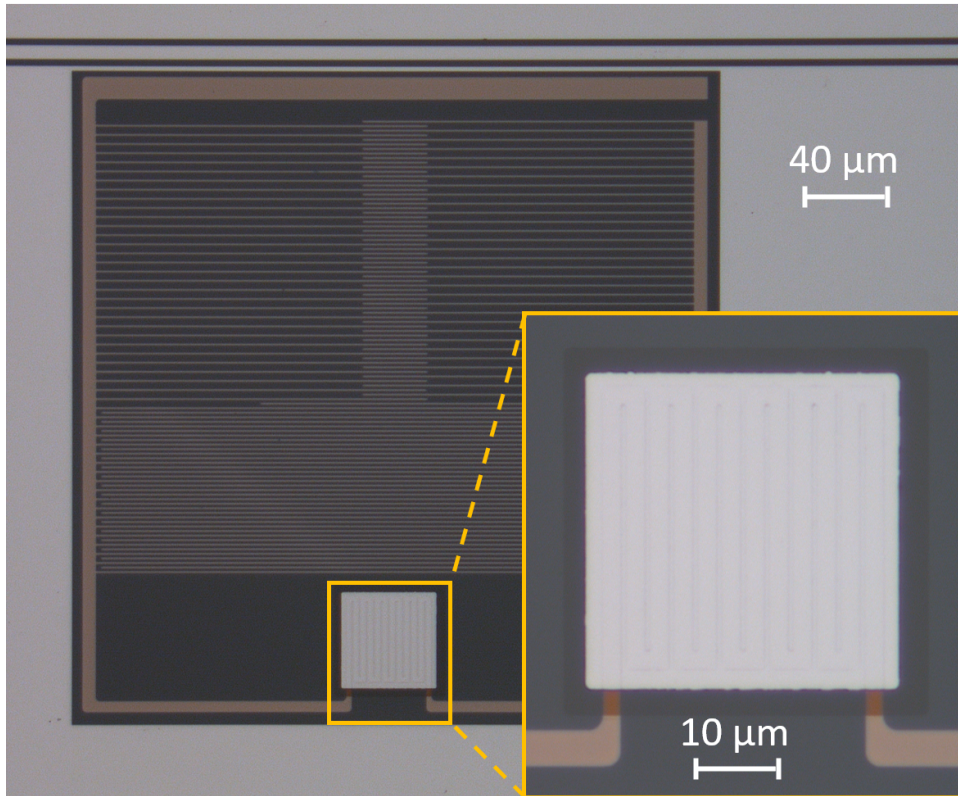
Figure 5.5: MKID pixel with a close up on the meander, barely visible in relief as it is covered by an opaque Nb layer to determine the origin of the phonon response. The shielding layer is separated from the meander by a dielectric layer. The fabrication steps are reversed compared to the optical stack pixel shown in Fig. 4.24.

By doing so, we prevent the MKID to absorb any incoming photon while still illuminating the large capacitive part of the pixels as well as the substrate below. The point of this experiment is to know whether the phonons that we think responsible for the inverse pulse originate either from quasiparticle recombination inside the inductor or from direct substrate heating. The fabrication process to cover the meander was very similar to the optical stack design but instead in a reverse order: first is the deposition of the TiN LC resonators directly on the substrate, then an Al_2O_3 layer is etched on top of the meander-shaped inductors and finally an opaque Niobium layer on top that is covering up the totality of the meanders. We have already demonstrated for the optical stack EM simulations in Sec. 4.4.4 that placing a superconducting layer close to the inductor do not deteriorate significantly the quality factors. We have chosen the relatively high T_c Niobium for the superconducting shielding layer to have a negligible quasiparticle population and minimize loss that can flow through the dielectric and into the resonator as simulated in

111

Fig. 4.23 with Aluminium. The dielectric thickness has been chosen to be larger than the Niobium coherence length so that photons absorbed by this shielding layer do not indirectly break the Cooper pairs inside the TiN meander through the proximity effect. The level of frequential noise and other measurements in-dark are similar to the optical stack sample in Sec. 4.5.1 and will not be covered here. We will focus on comparing the pulse response of the reference with the shielded sample at 400 mK in Fig. 5.6a where TLS is saturated and at 50 mK in Fig. 5.6b where the phonon response dominates. The resonator of each sample presented here have similar resonance frequencies (respectively 2.06 GHz and 2.29 GHz), similar internal quality factors (resp. 7.8×10^4 and 6.3×10^4), measured at the same -100 dBm readout power and illuminated with the same 405 nm laser diode for 200 ns.
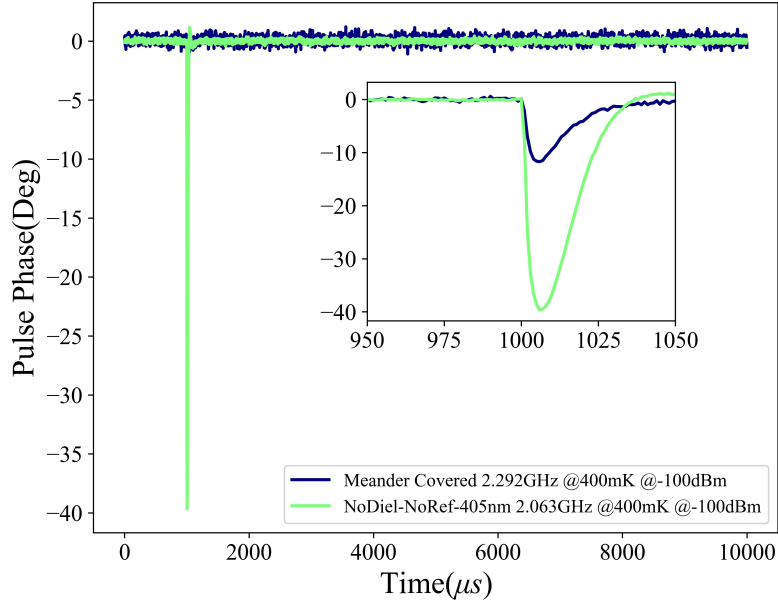
(a) 400 mK
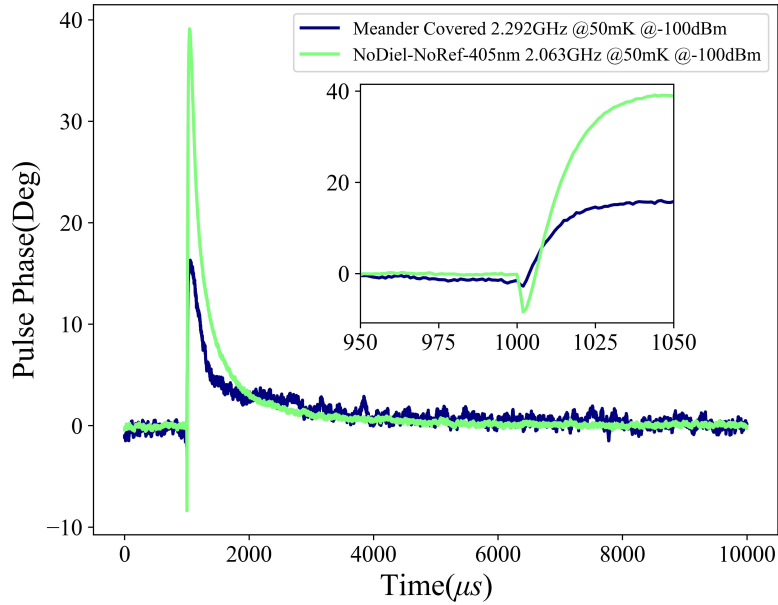
(b) 50 mK

Figure 5.6: Time-domain evolution of the pulse response to a 200 ns-long illumination with the 405 nm diode of the reference (NDNR) and the covered inductor samples at -100 dBm readout power. Both resonators have similar resonance frequencies and quality factors. The insets focus on the first 50 µs after illumination. (a) The response from the covered meander seems to have almost no quasiparticle breaking which reflects in (b) where the phonon response is also greatly diminished.

The phase shift in Fig. 5.6a corresponds to the expected Cooper pair breaking response with the short decay time. For the reference sample, we obtain a large phase shift of 40 degrees. For the covered meander sample however, we have reduced the response by almost a factor of 4 with a phase shift of 12 degrees. While the shielding layer covers the meander, a non-negligible part of the Cooper pair population is situated in the arms extending towards the IDC. In Sec. 4.4.1, we predicted the arms to account for 1/5th of Cooper pair breaking which is close from the experimental results. Now that we have successfully prevented most of the Cooper pair to break and recombine by emitting phonons, we can deduce whether the inverse pulse response originates from directly heating the substrate with the laser diode or from quasiparticle recombination. In Fig. 5.6b, the same diminution is observed for the inverse pulse where the reference and the covered meander have respectively a 40 and 16 degrees phase shift. This shows a strong correlation between the number of quasiparticles recombining and the inverse pulse when TLS is not saturated. It would be relevant to verify if the residual inverse phase shift is truly attributed to Cooper pair breaking and recombining in the extending arms by having a shielding layer that covers both the meander and the arms.

5.2   Phonon response model

From observations in the previous sections, we suspect this inverse phase shift to be related to thermal perturbations generated by phonon-TLS interaction. After a relaxation time of a few microseconds in the time domain of the standard phase shift, quasiparticles return to their lowest state and recombine into Cooper pairs by releasing phonons that excite the TLS in the substrate. The thermal perturbation associated is responsible for briefly affecting the dielectric constant of the substrate which has a direct impact on the capacitance of the resonator and thus on its phase.

5.2.1   Superconductor heat capacity analysis

The total heat capacity of a superconductor C_s has three main components: electrons, phonons and TLS. For temperatures $T \leq T_c/20$ where the inverse pulse phenomenon appears, the volumetric heat capacity of electrons in a superconducting LC resonator with volume V_{LC} can be estimated as:

$$\frac{C_{e^-}}{V_{\text{LC}}} = 1.34 N_{e^-} \gamma_s T_c \left(\frac{\Delta(0)}{k_B T} \right)^{\frac{3}{2}} \exp\left(-\frac{\Delta(0)}{k_B T} \right) \tag{5.1}$$

where N_{e^-} is the number of free electron per unit volume and $\gamma_s = \pi^2 k_B^2 / 2E_F$ is the linear coefficient of the specific heat in a normal metal. We estimate $N_{e^-} = 7.955 \times 10^{10}$ μm^{-3} and $\gamma_s = 0.603 \times 10^{-3}$ J $\cdot$ mol^{-1} $\cdot$ K^{-2} with $E_F = 5.865$ eV [82].

The volumetric heat capacity of phonons far below the Debye temperature ($T \ll \theta_D \approx$ 750 K [83]) can be approximated by the Debye T^3 law such as:

$$\frac{C_{\text{ph}}}{V_{\text{LC}}} = \frac{12\pi^4}{5} N_{\text{ph}} k_B \left(\frac{T}{\theta_D} \right)^3 \tag{5.2}$$

where N_{ph} is the number of phonon modes per unit volume. We estimate the number of TiN phonon modes in our film to be $N_{\text{ph}} = 1.553 \times 10^{11}$ μm^{-3}.

The TLS specific heat capacity can be estimated by [84]:

$$c_{\text{TLS}} = k_B N_{\text{TLS}} \left(\frac{\Delta E}{k_B T} \right)^2 \exp\left(-\frac{\Delta E}{k_B T} \right). \tag{5.3}$$

where N_{TLS} is the number of particles in a two-level system and ΔE represents the energy difference between the two potential wells. From the standard tunnelling model of TLS [57], the loss tangent of the TLS loaded material can be estimated as:

$$\delta_{\text{TLS}} = \frac{\pi P d^2}{3\epsilon} \tag{5.4}$$

where P is the TLS density of states in the material, d is the TLS electrical dipole and ϵ is the material dielectric constant. Finally, the volumetric heat capacity of the TLS can be estimated as:

$$\frac{C_{\text{TLS}}}{V_{\text{LC}}} = P \int_{E_1}^{E_2} c_{\text{TLS}} \mathrm{d}E = \frac{3\epsilon\delta}{\pi d^2} \int_{E_1}^{E_2} k_B \left(\frac{\Delta E}{k_B T} \right)^2 \exp\left(-\frac{\Delta E}{k_B T} \right) \mathrm{d}E \tag{5.5}$$

If we assume the TLS and phonons temperatures to be on the same order, the energy difference of the TLS will be on the order of the thermal phonons. $E_1 \approx k_B T$ with the same temperature of the superconductor and $E_2 \approx k_B T_2$. With these approximations, Eq. 5.5 can be simplified as:

$$\frac{C_{\text{TLS}}}{V_{\text{LC}}} = \frac{3\epsilon\delta k_B^2 T}{\pi d^2} \left\{ 1.839 - \left[\left(\frac{T_2}{T}\right)^2 + 2\frac{T_2}{T} + 2 \right] \exp\left(-\frac{T_2}{T}\right) \right\} \qquad (5.6)$$

where $T_2 \approx 250$ mK is the TLS temperature turning point measured in our samples. Eq. 5.6 shows that $C_{\text{TLS}} \propto T$ as opposed to the heat capacity of phonons that follows a T^3 Debye law. The electrical dipole is defined by $d = ed_0$ where $d_0 = 0.424$ nm is the stoichiometric TiN lattice constant.
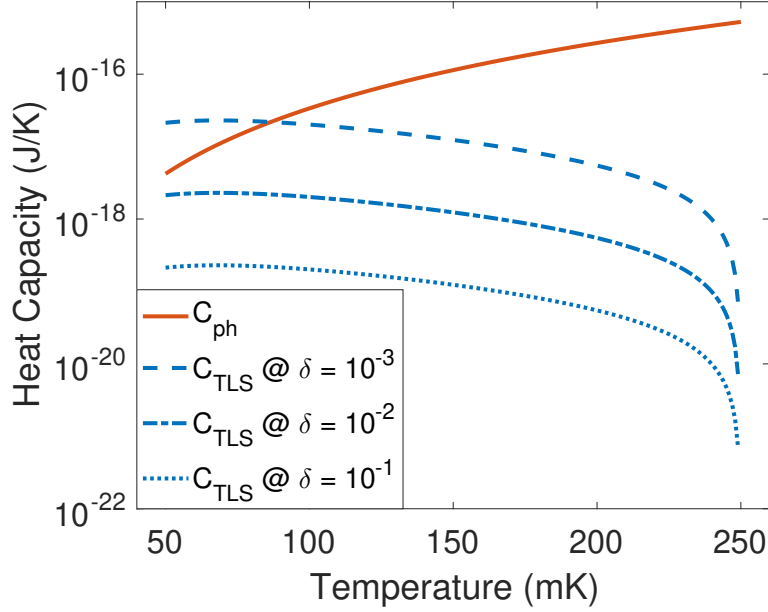
Figure 5.7: Semilog plot of the expected heat capacity of phonons and TLS for different values of dielectric tangent loss. The electron heat capacity is not represented here as it is negligible next to phonons and TLS.

As seen in Fig. 5.7, higher dielectric loss at the interface between the substrate and superconductor is synonym with less energy needed to produce heat which should be responsible for the inverse pulse longer decay. As the temperature decreases, the TLS heat capacity becomes significant and can even surpass the heat capacity of phonons produced inside the superconductor. Since the electron heat capacity is negligible, the total superconductor heat capacity can be approximated to $C_s \approx C_{\text{ph}} + C_{\text{TLS}}$.

5.2.2 Modelization of the thermal perturbation phase response

As detailed in Sec. 2.5, when an incident photon with enough energy to break Cooper pairs is absorbed by the MKID, the electrons are excited to a quasiparticle state during

a short time, usually on the order of 10 µs, after which they recombine to Cooper pairs by emitting thermal pertubations called phonons. If the bath temperature or MKID readout power is too low, the phonons generated inside the absorber can in turn excite the non-saturated TLS in the amorphous TLS hosting layer at the interface between the MKID and substrate. These ballistic phonons can propagate at extreme velocities through the substrate [53] resulting in a rapid change of dielectric $\epsilon_r + \Delta\epsilon_r$ measurable with the MKIDs capacitance. The fractional dielectric constant scales with Eq. 2.41 as $\Delta f/f = -\frac{1}{2}\Delta\epsilon/\epsilon$ [57] which naturally affects the frequency and phase of the resonator. This whole mechanism is depicted in Fig. 5.8 and is supported by the experiment we conducted in Sec. 5.1.2 where we demonstrated a strong correlation between Cooper pair breaking and the inverse pulse response.
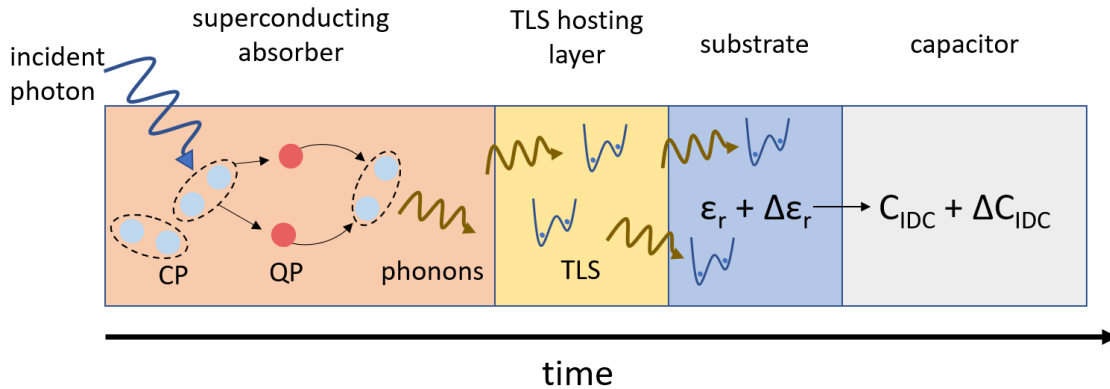
Figure 5.8: Timeline of the TLS-phonon interaction mechanism. An incident photon breaks Cooper pairs (CP) in the MKID absorber that are briefly excited to a quasiparticle (QP) state before recombination that emits energetic phonons. These phonons excites the non-saturated TLS in the amorphous TLS hosting layer and travel to the substrate which results in a change of dielectric constant $\Delta\epsilon_r$ and thus a change in frequency supported by Eq. 2.41

The thermal response of such a system is comparable to bolometers and thus can be expressed as [85]:

$$C_s \frac{dT}{dt} = -K(T^n - T_{\text{bath}}^n) + P_s + P_{\text{opt}} \qquad (5.7)$$

where K is a geometry-dependant factor, n the power-law coefficient, P_{opt} the optical

illumination power and C_s the heat capacity of the superconductor defined in the previous Sec. 5.2.1. P_s is the power from the feedline dissipating into the MKID that can be expressed on resonance as [53, 86]:

$$P_s = P_r \frac{2Q^2}{Q_i Q_c} \tag{5.8}$$

where P_r is the MKID readout power. In the case of a phonon event, the superconductor is subject to a time-varying change of temperature $T_{\mathrm{ph}}(t)$ such as:

$$T(t) = T_s + T_{\mathrm{ph}}(t) \tag{5.9}$$

where $T_s = (P_s/K + T_{\mathrm{bath}}^n)^{1/n}$ is the superconductor temperature in the steady-state under no optical illumination. Subsequently, Eq. 5.7 can be rewritten to include the phonon perturbation as follow:

$$\frac{dT_{\mathrm{ph}}}{dt} \approx -\frac{G}{C_s} \left[1 + \frac{(n-1)T_{\mathrm{ph}}}{2T_s} \right] T_{\mathrm{ph}} \tag{5.10}$$

where $G = nKT_s^{n-1}$ is the thermal conductance. Finally, using the analytical solution of Eq. 5.10, we can model the inverse phase response $\Delta\phi$ as a function of phonon perturbation at $t > t_0$, when the normal Cooper pair breaking process is considered to be over:

$$\Delta\phi(T_s, t > t_0) \approx -\frac{4Q}{f_0} \frac{\partial f_0(t)}{\partial T} \frac{T_{\mathrm{ph}}(t_0) \exp\left(-\dfrac{t-t_0}{\tau_{\mathrm{th}}}\right)}{1 + \dfrac{(n-1)T_{\mathrm{ph}}(t_0)}{2T_s} \left[1 - \exp\left(-\dfrac{t-t_0}{\tau_{\mathrm{th}}}\right) \right]} \tag{5.11}$$

where $\tau_{\mathrm{th}} = C_s/G$ is the inverse pulse response characteristic time related to the thermal flow between the superconductor and substrate. This model has been successfully fitted to the inverse pulse evolution in Fig. 5.9a as a function of temperature and in Fig. 5.9b as a function of input power. The characteristic phonon time represented in the inset of Fig. 5.9a clearly shows the inverse pulse dependance to TLS strength as τ_{th} drops down by a factor of 3 between 100 and 150 mK and it becomes negligible at 200 mK. We can draw the same conclusion from the inset of Fig. 5.9b where τ_{th} drops down between -105 and -100 dBm of readout power. There is an abrupt temperature and power transition between

the TLS saturated and non-saturated states, which was not as obvious for the larger IDC MKID size we measured where τ_{th} seemed to follow a more linear behavior [87].
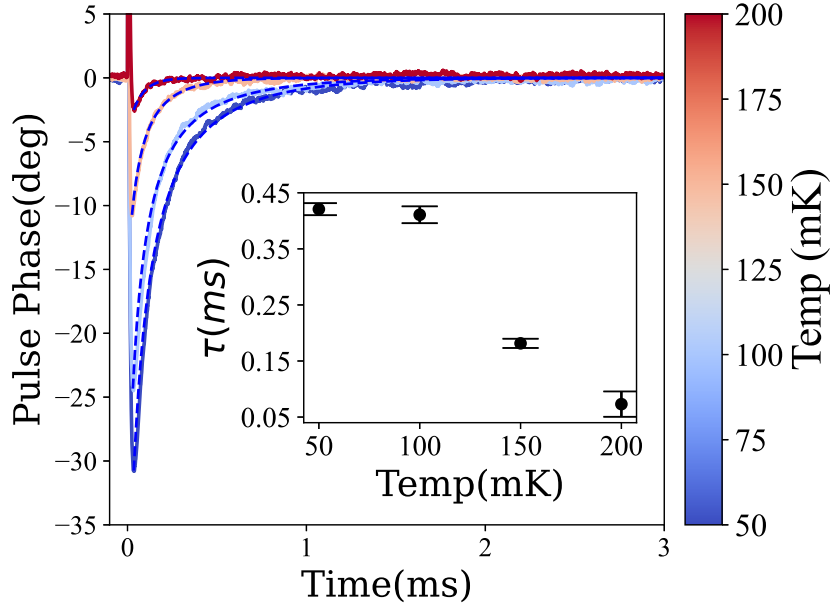
(a)
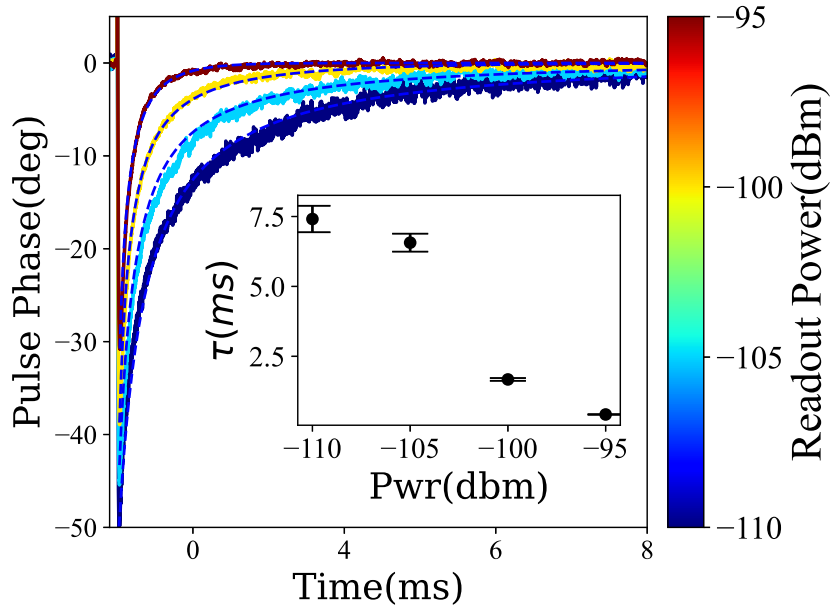
(b)

Figure 5.9: Time-domain evolution of the pulse response on the reference sample following a 200 ns-long illumination with the 405 nm diode. The dashed lines represents the fitting from the model proposed in Eq. 5.11 and the insets show the fitted characteristic time τ_{th}. Unlike for the normal quasiparticle phase response that is not represented here, the inverse pulse decay is TLS-dependant and varies as a function of (a) bath temperature or (b) readout power.

5.3 Amplification of the inverse pulse response for a possible phonon-based detection

In this section, we will investigate whether the source of TLS regarded as noise for MKIDs can be amplified to reach single-photon sensitivity. It has already been demonstrated that thermometers based on MKIDs have had increased responsivity by boosting TLS [88]. In our case, the detector would not probe the kinetic inductance change in the meander but rather the capacitance change in the IDC caused by TLS-phonon interactions. We will name this technology MTAD for *Microwave TLS Amplified Detector*. In contrast to MKIDs that need low-T_c materials to count photons, a MTAD would be made from high-T_c materials to be cooled down well below its TLS turning point. We will conduct this study with stoichiometric TiN resonators as we have already demonstrated its large phonon response at $T < T_c/20$. We propose to add the same 60 nm-thick Al_2O_3 dielectric layer used for the optical stack but this time deposited below the IDC. We expect to increase the TLS density in the vicinity of the capacitor responsible for the large inverse phase response. The dielectric layer surface is increased by a tenfold compared to the optical stack design as the IDC is much larger than the inductor which should also lead to an increase in phonon response.

5.3.1 In-dark measurements

Similarly to the optical stack study, we will first measure the different in-dark parameters before illumination. We have chosen to compare this new geometry (*Dielectric Below IDC*, DBI) to the same NDNR and YDNR samples presented in the optical stack chapter, starting with Q_i as a function of temperature in Fig. 5.10.
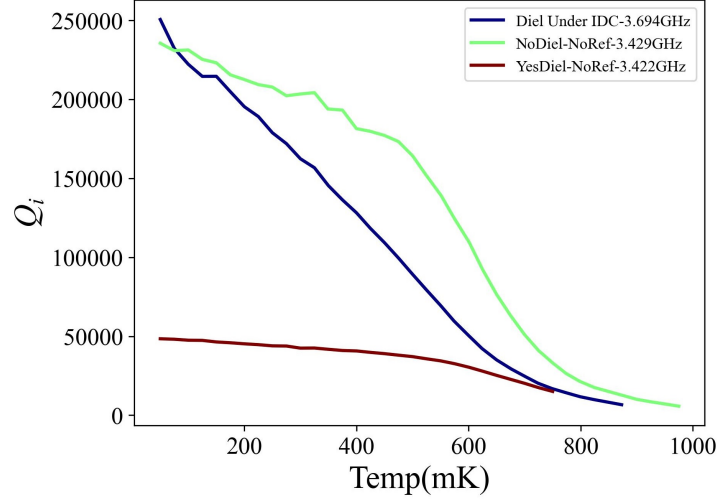
Figure 5.10: Comparison of the internal quality factor of one resonator in each sample with similar f_0 as a function of bath temperature measured at -100 dBm.

Surprisingly, the DBI sample has a similar Q_i to the NDNR reference at low temperatures where TLS should be the most abundant and is confirmed in Fig. 5.11. However, we have to keep in mind that in DBI, there is no dielectric below the inductor where the Cooper pair density is the highest. We suspect that the dielectric in YDNR thermally isolates the inductor from the substrate and cannot reach temperatures low enough to reduce its quasiparticle population. In DBI and NDNR, the inductor is deposited directly on the substrate and may explain why we obtain this high level of Q_i.
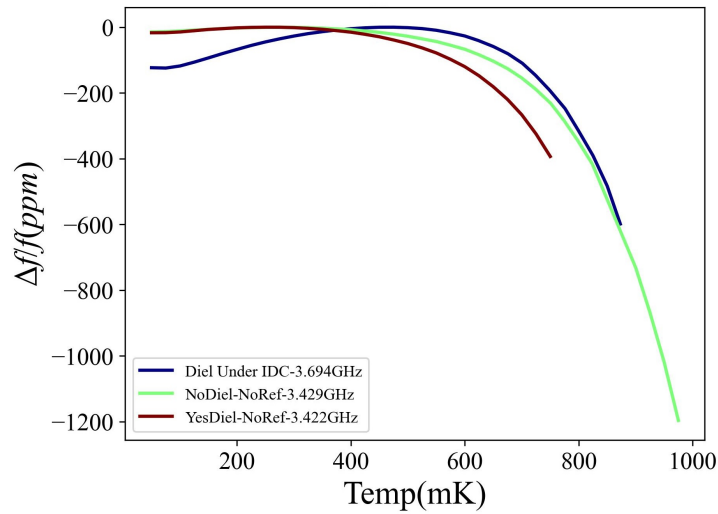
Figure 5.11: Comparison of $\Delta f/f$ as a function of bath temperature measured at -100 dBm.

The $\Delta f/f$ of the DBI sample is similar to YDYR in Fig. 4.27 as the resonance first shifts to higher frequencies due to TLS. However, the TLS turning point in DBI has doubled compared to YDYR and is now around 500 mK. This is consistent with the reported evolution of the fractional frequency shift as a function of the dielectric volume in contact with the resonator [78].
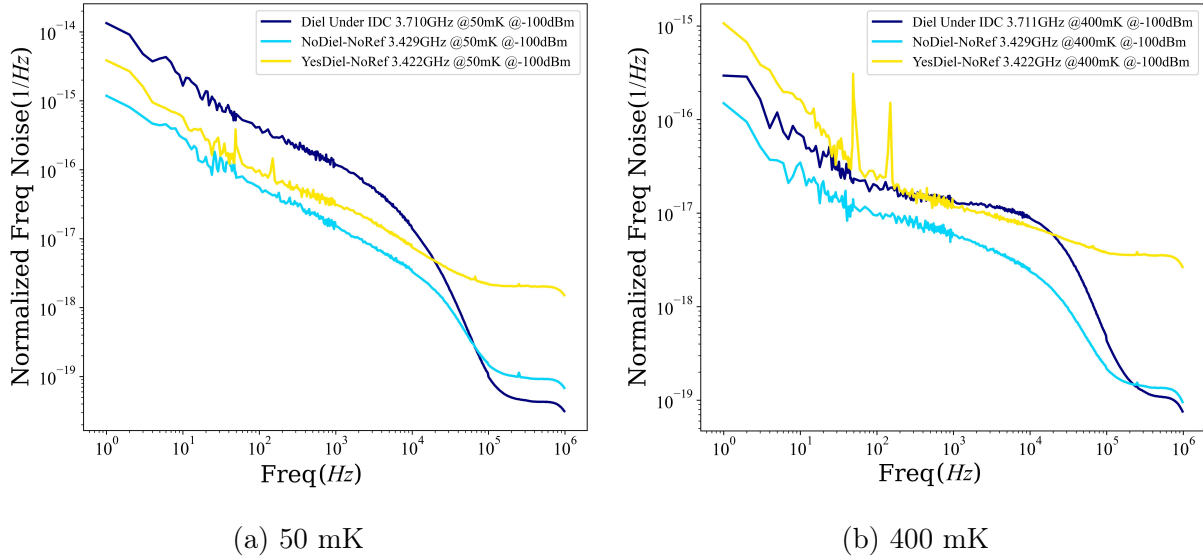
(a) 50 mK

(b) 400 mK

Figure 5.12: Normalized frequential noise of one pixel in each of the three samples measured at -100 dBm input power at (a) 50 mK where TLS is dominant and (b) at 400 mK where TLS is saturated.

In Fig. 5.12a, all three samples share the same $f^{-1/2}$ slope between 10^2 and 10^4 and the frequency noise in DBI caused by TLS is naturally higher than in YDNR where the dielectric volume is much smaller. In Fig. 5.12b, the slope of the DBI sample in the same spectral region has completely flattened out and has lowered to the same level as YDNR. This could be explained by the larger Q_i of DBI at 40 mK compared to YDNR seen in Fig. 5.10 which is inversely proportional to the dielectric loss tangent in Eq. 2.42. Moreover, in YDNR, the dielectric is in contact with the inductor where the denser Cooper pair population responsible for detection directly interacts with TLS that may not be completely saturated at 400 mK.

5.3.2 Optical illumination response

In this section, we will present the detector's response to short light pulses with the setup detailed in Sec. 3.8. We illuminate the sample using the 405 nm laser diode with the same power of 4 pW as for previous samples. The largest inverse phase response at 50 mK and -100 dBm shown in Fig. 5.13 was measured on the resonator with the lowest $f_0 \approx 2.2$ GHz with a $Q_i = 3.5 \times 10^5$ and a total $Q = 1.3 \times 10^5$.
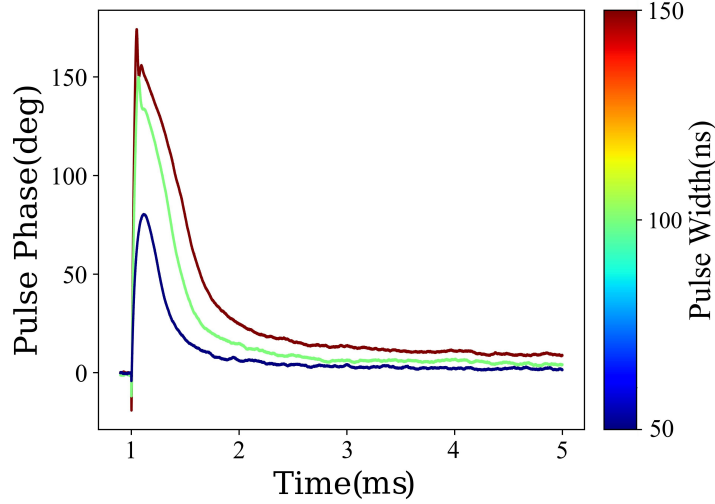
Figure 5.13: Averaged pulse phase response with different illumination width at 50 mK and -100 dBm. The inverse pulse response is much larger than for the reference sample in Fig. 5.1b

The inverse pulse response at 50 mK has drastically increased compared to the reference sample without dielectric shown in Fig. 5.1b. For a 50 ns-long pulse, the phase change is around 80 degrees, a tenfold of what was recorded for the reference sample. However, if we consider the detector SNR, the frequential noise in the resonator bandwidth represented in Fig. 5.12a has also increased by a tenfold. For longer illumination pulse width, the phase seems to enter a non-linear response that may be caused by the resonator response time $\tau_{\mathrm{rsp}} = 20$ µs computed from Eq. 3.4 not fast enough to register this large of a phase shift. The single-photon mode on this sample has not been reached but we have nonetheless demonstrated the amplification of the inverse pulse by cleverly placing a TLS-loaded material below the capacitor, where the fractional dielectric change has the most influence on the resonator.

Conclusion and outlook

As an effort to improve optical coupling in MKIDs, we have proposed a novel optical stack design below the absorber. We have conducted several optical characterization and modelization on our thin-film layers to optimize the coupling: an Al reflector is set at a quarter-wavelength of the absorber with the use of a transparent low dielectric tangent loss Al_2O_3 layer. In the first fabrication and measurement run, it was observed that high quality factors were not achievable with this geometry. The low-T_c Al layer has been suspected to have a large quasiparticle density at the 400 mK operating temperature which would increase loss. This was resolved in the second batch by placing a higher T_c Nb "booster" layer below Al so that it could share its superconducting properties through the proximity effect. While we obtained high-Q factors with this new optical stack sample, we have not reached single-photon counting due to a tenfold of frequential noise compared to the reference. This larger noise is probably distributed between the optical stack parasitic capacitance, the TLS inside the Al_2O_3 layer as well as the number of interface where nanometer-thick TLS-hosting layers prone to form has tripled. In order to counteract this larger noise, we can either reduce the optical stack noise or use a more sensitive material as the absorber. For the former, we are considering replacing the quarter-wavelength spacer Al_2O_3 layer with vaccum. Our group has already demonstrated in the past the feasability to suspend TiN using a sacrificial layer to fabricate vacuum MIM capacitors that allowed for high quality factors millimeter MKIDs [64]. The same principle could be reproduced for the optical stack so that the parasitic capacitance would be completely nullified. The amorphous layers forming at the surface of the reflector and absorber would not be avoided but it would help us determine their contribution to the total noise increase caused by the optical stack. For the latter, we have fabricated and characterized MKIDs with the more sensitive sub-stoichiometric TiN_x. The results

were not discussed here as we obtained in both the reference and optical stack samples mediocre quality factors that led to shallow resonances on which single-photon mode was not possible. We suspect a mismatch between the TiN_x and sapphire substrates supported by other groups results [12]. Another solution would be to use multi-layer Ti/TiN: the succession of pure Ti and stoichiometric TiN layers can act by proximity effect as a single layer with a controllable T_c as a function of each layer's thickness. Once we will have fully characterized multi-layer Ti/TiN, we plan to recreate the optical stack study with a $T_c \approx 1$ K to hopefully quantify the optical coupling efficiency. Moreover, both Ti and TiN have better reproducibility and uniformity than TiN_x which would favor multi-layer Ti/TiN for kilopixels arrays such as the future SPIAKID instrument. Otherwise, if we were to set aside Titanium, the most promising up-and-coming material would be Hafnium for its high resistivity, high quality factors and uniformity largely superior than for TiN_x [62]. However, its very-low $T_c \approx 400$ mK requires a high-end ADR to operate.

In parallel, we have been the first to demonstrate with my reference sample the possibility to use stoichiometric TiN for photon-counting at temperatures up to 500 mK. While the energy resolution is still relatively low in this configuration compared to the theoretical limit, it opens up new possibilities for the use of higher-T_c materials to count optical photons without the need of a costly ADR to operate at 100 mK and below.

During this thesis work, a new anomalous response from stoichiometric TiN has been observed on some of our samples in the form of a large transient inverse pulse. We have attributed this phenomenon to phonon perturbations that excites the non-saturated TLS in amorphous layers as well as the substrate bulk at temperatures below $T_c/20 \approx 300$ mK. This leads to a change of the substrate dielectric constant which directly affects the MKIDs IDC and thus the resonance frequency. Since phonons are generated by the recombination of quasiparticles, we have confirmed their origin by covering the MKIDs absorber with an opaque layer to prevent Cooper pair breaking. We have naturally observed a large diminution in Cooper pair breaking during illumination followed by a proportional diminution of the inverse phase response. This has confirmed that phonons are indeed generated in the absorber after a photon event and not from the substrate direct heating. With that in mind, we have deliberately added a TLS-hosting layer below the IDC to try and amplify the phonon response. The detection would not be recorded by the change

in kinetic inductance inside the absorber like for normal MKIDs but rather through the change of the substrate dielectric constant in what we called a MTAD. Such a technology could be useful in other astronomy applications such as dark matter experiments where phonons are probed [89]. We have successfully demonstrated the amplification of the inverse response while also increasing the resonator frequential noise which has prevented the recording of a photon event. We will further investigate this detection mechanism by using more sensitive absorbing materials to increase the TLS-phonon interaction and hopefully reach the single-photon response.

Appendix A

Acid cleaning parameters

Solution	Volume ratio	Temp	Time	Target
Piranha	H_2SO_4 (3) : H_2O_2 (1)	95°C	600 s	Organic contaminants
SC1	NH_4OH (1) : H_2O_2 (1) : H_2O (5)	70°C	600 s	Particles
Dilute HF	HF (1) : H_2O (10)	20°C	30 s	Oxides and H-Passivation

Table A.1: Wet cleaning procedure

Bibliography

[1]   W. S. Boyle and G. E. Smith. "Charge coupled semiconductor devices". In: *The Bell System Technical Journal* 49.4 (1970), pp. 587–593. DOI: `10.1002/j.1538-7305.1970.tb01790.x` (page 1).

[2]   M Sirianni, M J Jee, N Benítez, J P Blakeslee, A R Martel, G Meurer, M Clampin, G De Marchi, H C Ford, R Gilliland, G F Hartig, G D Illingworth, J Mack, and W J Mccann. *The Photometric Performance and Calibration of the HST Advanced Camera For Surveys*. 2005 (page 1).

[3]   Brian et al. Welch. "A highly magnified star at redshift 6.2". In: *Nature* 603.7903 (Mar. 2022), pp. 815–818. DOI: `10.1038/s41586-022-04449-y` (page 1).

[4]   Olivier Daigle, Oleg Djazovski, Denis Laurin, René Doyon, and Étienne Artigau. "Characterization results of EMCCDs for extreme low-light imaging". In: 8453 (2012). Ed. by Andrew D. Holland and James W. Beletic, p. 845303. DOI: `10.1117/12.926385` (page 1).

[5]   D. H. Andrews, W. F. Brucksch, W. T. Ziegler, and E. R. Blanchard. "Attenuated Superconductors I. For Measuring Infra-Red Radiation". In: *Review of Scientific Instruments* 13.7 (1942), pp. 281–292. DOI: `10.1063/1.1770037` (page 2).

[6]   K. D. Irwin. "An application of electrothermal feedback for high resolution cryogenic particle detection". In: *Applied Physics Letters* 66.15 (1995), pp. 1998–2000. DOI: `10.1063/1.113674` (page 2).

[7]   B. D. Josephson. "Possible new effects in superconductive tunnelling". In: *Physics Letters* 1 (1962), pp. 251–253. DOI: `10.1016/0031-9163(62)91369-0` (pages 2, 15).

[8]   Dileep V. Reddy, Robert R. Nerem, Sae Woo Nam, Richard P. Mirin, and Varun B. Verma. "Superconducting nanowire single-photon detectors with 98% system

detection efficiency at 1550 nm". In: *Optica* 7.12 (Dec. 2020), p. 1649. DOI: `10.1364/OPTICA.400751` (page 2).

[9]   Boris Korzh, Qing-Yuan Zhao, Jason P. Allmaras, Simone Frasca, Travis M. Autry, Eric A. Bersin, Andrew D. Beyer, Ryan M. Briggs, Bruce Bumble, Marco Colangelo, Garrison M. Crouch, Andrew E. Dane, Thomas Gerrits, Adriana E. Lita, Francesco Marsili, Galan Moody, Cristián Peña, Edward Ramirez, Jake D. Rezac, Neil Sinclair, Martin J. Stevens, Angel E. Velasco, Varun B. Verma, Emma E. Wollman, Si Xie, Di Zhu, Paul D. Hale, Maria Spiropulu, Kevin L. Silverman, Richard P. Mirin, Sae Woo Nam, Alexander G. Kozorezov, Matthew D. Shaw, and Karl K. Berggren. "Demonstration of sub-3 ps temporal resolution with a superconducting nanowire single-photon detector". In: *Nature Photonics* 14.4 (Mar. 2020), pp. 250–255. DOI: `10.1038/s41566-020-0589-x` (page 2).

[10]   Peter K. Day, Henry G. LeDuc, Benjamin. A. Mazin, Anastasios Vayonakis, and Jonas Zmuidzinas. "A broadband superconducting detector suitable for use in large arrays". In: *Nature* 425 (2003), pp. 817–821. DOI: `10.1038/nature02037` (page 3).

[11]   W. Guo, X. Liu, Y. Wang, Q. Wei, L. F. Wei, J. Hubmayr, J. Fowler, J. Ullom, L. Vale, M. R. Vissers, and J. Gao. "Counting near infrared photons with microwave kinetic inductance detectors". In: *Applied Physics Letters* 110.21 (2017). DOI: `10.1063/1.4984134` (pages 3, 32, 60, 79).

[12]   Benjamin A. Mazin. "Superconducting Materials for Microwave Kinetic Inductance Detectors". In: (2020) (pages 3, 126).

[13]   Nicholas Zobrist, W. Hawkins Clay, Grégoire Coiffard, Miguel Daal, Noah Swimmer, Peter Day, and Benjamin A. Mazin. "Membrane-less phonon trapping and resolution enhancement in optical microwave kinetic inductance detectors". In: (2022), pp. 1–10. DOI: `10.1103/PhysRevLett.129.017701` (pages 3, 32).

[14]   A. Monfardini, R. Adam, A. Adane, P. Ade, P. André, A. Beelen, B. Belier, A. Benoit, A. Bideaud, N. Billot, O. Bourrion, M. Calvo, A. Catalano, G. Coiffard, B. Comis, A. D'Addabbo, F. X. Désert, S. Doyle, J. Goupy, C. Kramer, S. Leclercq, J. Macias-Perez, J. Martino, P. Mauskopf, F. Mayet, F. Pajot, E. Pascale, N. Ponthieu, V. Revéret, L. Rodriguez, G. Savini, K. Schuster, A. Sievers, C. Tucker, and R. Zylka. "Latest NIKA results and the NIKA-2 project". In: *Journal of Low Tem-*

perature Physics 176.5-6 (2014), pp. 787–795. DOI: `10.1007/s10909-013-0985-4` (page 3).

[15] M. Calvo, A. Benoît, A. Catalano, J. Goupy, A. Monfardini, N. Ponthieu, E. Barria, G. Bres, M. Grollier, G. Garde, J. P. Leggeri, G. Pont, S. Triqueneaux, R. Adam, O. Bourrion, J. F. Macías-Pérez, M. Rebolo, A. Ritacco, J. P. Scordilis, D. Tourres, A. Adane, G. Coiffard, S. Leclercq, F. X. Désert, S. Doyle, P. Mauskopf, C. Tucker, P. Ade, P. André, A. Beelen, B. Belier, A. Bideaud, N. Billot, B. Comis, A. D'Addabbo, C. Kramer, J. Martino, F. Mayet, F. Pajot, E. Pascale, L. Perotto, V. Revéret, A. Ritacco, L. Rodriguez, G. Savini, K. Schuster, A. Sievers, and R. Zylka. "The NIKA2 Instrument, A Dual-Band Kilopixel KID Array for Millimetric Astronomy". In: *Journal of Low Temperature Physics* 184.3-4 (2016), pp. 816–823. DOI: `10.1007/s10909-016-1582-0` (page 3).

[16] B. A. Mazin, S. R. Meeker, M. J. Strader, P. Szypryt, D. Marsden, J. C. van Eyken, G. E. Duggan, A. B. Walter, G. Ulbricht, M. Johnson, B. Bumble, K. O'Brien, and C. Stoughton. "ARCONS: A 2024 Pixel Optical through Near-IR Cryogenic Imaging Spectrophotometer". In: *Publications of the Astronomical Society of the Pacific* 125.933 (2013), pp. 1348–1361. DOI: `10.1086/674013` (page 4).

[17] Seth R. Meeker, Benjamin A. Mazin, Alex B. Walter, Paschal Strader, Neelay Fruitwala, Clint Bockstiegel, Paul Szypryt, Gerhard Ulbricht, Grégoire Coiffard, Bruce Bumble, Gustavo Cancelo, Ted Zmuda, Ken Treptow, Neal Wilcer, Giulia Collura, Rupert Dodkins, Isabel Lipartito, Nicholas Zobrist, Michael Bottom, J. Chris Shelton, Dimitri Mawet, Julian C. Van Eyken, Gautam Vasisht, and Eugene Serabyn. "DARKNESS: A microwave kinetic inductance detector integral field spectrograph for high-contrast astronomy". In: *Publications of the Astronomical Society of the Pacific* 130.988 (2018), p. 65001. DOI: `10.1088/1538-3873/aab5e7` (page 4).

[18] Alex B. Walter, Clinton Bockstiegel, Timothy D. Brandt, and Benjamin A. Mazin. "Stochastic speckle discrimination with time-tagged photon lists: Digging below the speckle noise floor". In: *Publications of the Astronomical Society of the Pacific* 131.1005 (2019). DOI: `10.1088/1538-3873/AB389A` (page 4).

[19] Alexander B. Walter, Neelay Fruitwala, Sarah Steiger, John I. Bailey, Nicholas Zobrist, Noah Swimmer, Isabel Lipartito, Jennifer Pearl Smith, Seth R. Meeker, Clint Bockstiegel, Gregoire Coiffard, Rupert Dodkins, Paul Szypryt, Kristina K. Davis,

Miguel Daal, Bruce Bumble, Giulia Collura, Olivier Guyon, Julien Lozi, Sebastien Vievard, Nemanja Jovanovic, Frantz Martinache, Thayne Currie, and Benjamin A. Mazin. "The MKID exoplanet camera for Subaru SCEXAO". In: *Publications of the Astronomical Society of the Pacific* 132.1018 (2020), pp. 1–13. DOI: 10.1088/1538-3873/abc60f (page 4).

[20] Sarah Steiger, Thayne Currie, Timothy D. Brandt, Olivier Guyon, Masayuki Kuzuhara, Jeffrey Chilcote, Tyler D. Groff, Julien Lozi, Alexander B. Walter, Neelay Fruitwala, John I. Bailey, III, Nicholas Zobrist, Noah Swimmer, Isabel Lipartito, Jennifer Pearl Smith, Clint Bockstiegel, Seth R. Meeker, Gregoire Coiffard, Rupert Dodkins, Paul Szypryt, Kristina K. Davis, Miguel Daal, Bruce Bumble, Sebastien Vievard, Ananya Sahoo, Vincent Deo, Nemanja Jovanovic, Frantz Martinache, Greg Doppmann, Motohide Tamura, N. Jeremy Kasdin, and Benjamin A. Mazin. "SCExAO/MEC and CHARIS Discovery of a Low-mass, 6 au Separation Companion to HIP 109427 Using Stochastic Speckle Discrimination and High-contrast Spectroscopy*". In: *The Astronomical Journal* 162.2 (2021), p. 44. DOI: 10.3847/1538-3881/ac02cc (page 4).

[21] Noah Swimmer, Thayne Currie, Sarah Steiger, G Mirek Brandt, Timothy D Brandt, Olivier Guyon, Masayuki Kuzuhara, Jeffrey Chilcote, Taylor Tobin, Tyler D Groff, Julien Lozi, John I I I Bailey, Alexander B Walter, Neelay Fruitwala, Nicholas Zobrist, Jennifer Pearl Smith, Gregoire Coiffard, Rupert Dodkins, Kristina K Davis, Miguel Daal, Bruce Bumble, Sebastien Vievard, Nour Skaf, and Vincent Deo. "SCExAO and Keck Direct Imaging Discovery of a Low-mass Companion Around the Accelerating F5 Star HIP 5319". In: *The Astronomical Journal* 164.4 (2022), p. 152. DOI: 10.3847/1538-3881/ac85a8 (page 4).

[22] Gerhard Ulbricht, Mario De Lucia, and Eoin Baldwin. "Applications for microwave kinetic induction detectors in advanced instrumentation". In: *Applied Sciences (Switzerland)* 11.6 (2021). DOI: 10.3390/app11062671 (page 4).

[23] V. C. Rubin, Jr. Ford W. K., and N. Thonnard. "Rotational properties of 21 SC galaxies with a large range of luminosities and radii, from NGC 4605 (R=4kpc) to UGC 2885 (R=122kpc)." In: *Astrophysical Journal* 238 (June 1980), pp. 471–487. DOI: 10.1086/158003 (page 6).

[24] S. D. M. White and M. J. Rees. "Core condensation in heavy halos: a two-stage theory for galaxy formation and clustering". In: *Monthly Notices of the Royal Astronom-*

ical Society 183.3 (July 1978), pp. 341–358. DOI: `10.1093/mnras/183.3.341`. eprint: `https://academic.oup.com/mnras/article-pdf/183/3/341/2943374/mnras183-0341.pdf` (page 6).

[25] Daniel R. Weisz, Jay Anderson, Martha L. Boyer, Andrew A. Cole, Andrew Eugene Dolphin, Marla C. Geha, Jason Kalirai, Nitya Kallivayalil, Kristen B. W. McQuinn, Karin Marie Sandstrom, and Benjamin F. Williams. *The Resolved Stellar Populations Early Release Science Program*. JWST Proposal ID 1334. Cycle 0 Early Release Science. Nov. 2017 (page 7).

[26] Beth Willman, Michael R. Blanton, Andrew A. West, Julianne J. Dalcanton, David W. Hogg, Donald P. Schneider, Nicholas Wherry, Brian Yanny, and Jon Brinkmann. "A New Milky Way Companion: Unusual Globular Cluster or Extreme Dwarf Satellite?" In: *The Astronomical Journal* 129.6 (June 2005), p. 2692. DOI: `10.1086/430214` (page 8).

[27] Beth Willman, Julianne J. Dalcanton, David Martinez-Delgado, Andrew A. West, Michael R. Blanton, David W. Hogg, J. C. Barentine, Howard J. Brewington, Michael Harvanek, S. J. Kleinman, Jurek Krzesinski, Dan Long, Jr. Neilsen Eric H., Atsuko Nitta, and Stephanie A. Snedden. "A New Milky Way Dwarf Galaxy in Ursa Major". In: *The Astrophysical Journal Letters* 626.2 (June 2005), pp. L85–L88. DOI: `10.1086/431760` (page 8).

[28] K. Bechtol et al. "Eight New Milky Way Companions Discovered In First-Year Dark Energy Survey Data". In: *Astrophysical Journal* 807 (1 July 2015). DOI: `10.1088/0004-637X/807/1/50` (page 8).

[29] David J. Sand, Burçin Mutlu-Pakdil, Michael G. Jones, Ananthan Karunakaran, Feige Wang, Jinyi Yang, Anirudh Chiti, Paul Bennet, Denija Crnojević, and Kristine Spekkens. "Tucana B: A Potentially Isolated and Quenched Ultra-faint Dwarf Galaxy at D = 1.4 Mpc*". In: *The Astrophysical Journal Letters* 935.1 (2022), p. L17. DOI: `10.3847/2041-8213/ac85ee` (page 8).

[30] Simon E. T. Smith, Jaclyn Jensen, Joel Roediger, Federico Sestito, Christian R. Hayes, Alan W. McConnachie, Jean-Charles Cuillandre, Stephen Gwyn, Eugene Magnier, Ken Chambers, Francois Hammer, Mike Hudson, Nicolas Martin, Julio Navarro, and Douglas Scott. "Discovery of a new Local Group Dwarf Galaxy Candidate in UNIONS: Bo\"otes V". In: (2022) (page 8).

[31] W. Cerny, C. E. Martínez-Vázquez, A. Drlica-Wagner, A. B. Pace, B. Mutlu-Pakdil, T. S. Li, A. H. Riley, D. Crnojević, C. R. Bom, J. A. Carballo-Bello, J. L. Carlin, A. Chiti, Y. Choi, M. L. M. Collins, E Darragh-Ford, P. S. Ferguson, M. Geha, D. Martínez-Delgado, P. Massana, S. Mau, G. E. Medina, R. R. Muñoz, E. O. Nadler, K. A. G. Olsen, A. Pieres, J. D. Sakowska, J. D. Simon, G. S. Stringfellow, A. K. Vivas, A. R. Walker, and R. H. Wechsler. "Six More Ultra-Faint Milky Way Companions Discovered in the DECam Local Volume Exploration Survey". In: (2022) (page 8).

[32] Mia S. Bovill and Massimo Ricotti. "Pre-reionization Fossils, Ultra-faint Dwarfs and the Missing Galactic Satellite Problem". In: (June 2008). DOI: `10.1088/0004-637X/693/2/1859` (page 8).

[33] R. J. Bouwens, G. D. Illingworth, P. A. Oesch, M. Trenti, I. Labbe, M. Franx, M. Stiavelli, C. M. Carollo, P. van Dokkum, and D. Magee. "Lower-Luminosity Galaxies could reionize the Universe: Very Steep Faint-End Slopes to the UV Luminosity Functions at z>=5-8 from the HUDF09 WFC3/IR Observations". In: (May 2011). DOI: `10.1088/2041-8205/752/1/L5` (page 8).

[34] Francesca Matteucci. "Modelling the chemical evolution of the Milky Way". In: *Astronomy and Astrophysics Reviews* 29.1, 5 (Dec. 2021), p. 5. DOI: `10.1007/s00159-021-00133-8` (page 9).

[35] Massimo Ricotti and Nickolay Y. Gnedin. "Formation Histories of Dwarf Galaxies in the Local Group". In: *The Astrophysical Journal* 629.1 (Aug. 2005), p. 259. DOI: `10.1086/431415` (page 9).

[36] Stefania Salvadori, Ása Skúladóttir, and Eline Tolstoy. "Carbon-enhanced metal-poor stars in dwarf galaxies". In: *Monthly Notices of the Royal Astronomical Society* 454.2 (Oct. 2015), pp. 1320–1331. DOI: `10.1093/mnras/stv1969` (page 9).

[37] Joss Bland-Hawthorn, Ralph Sutherland, and David Webster. "Ultrafaint Dwart Galaxies: The Lowest-Mass Relics From Before Reionization". In: *The Astrophysical Journal* 807.2 (July 2015), p. 154. DOI: `10.1088/0004-637X/807/2/154` (page 9).

[38] W. Meissner and R. Ochsenfeld. "Ein neuer Effekt bei Eintritt der Supraleitfähigkeit." In: *Naturwissenschaften* 21 (1933), pp. 787–788. DOI: `10.1007/BF01504252` (page 14).

[39] A. W.B. Taylor. "The microscopic theory of superconductivity". In: *Contemporary Physics* 9.6 (1968), pp. 549–564. DOI: `10.1080/00107516808220097` (page 15).

[40] J. R. Schrieffer. "Theory of super conductivity". In: *Theory of Superconductivity* (2018), pp. 1–332. DOI: `10.1201/9780429495700` (page 15).

[41] Leon N. Cooper. "Bound Electron Pairs in a Degenerate Fermi Gas". In: *Physical Review Letters* 104 (1956), p. 1189. DOI: `10.1103/PhysRev.104.1189` (page 15).

[42] John Bardeen. "Two-Fluid Model of Superconductivity". In: *Physical Review Letters* 1 (1958), pp. 399–400. DOI: `10.1103/PhysRevLett.1.399` (page 20).

[43] Jiansong Gao, Miguel Daal, John M. Martinis, Anastasios Vayonakis, Jonas Zmuidzinas, Bernard Sadoulet, Benjamin A. Mazin, Peter K. Day, and Henry G. Leduc. "A semiempirical model for two-level system noise in superconducting microresonators". In: *Applied Physics Letters* 92.21 (2008), pp. 1–11. DOI: `10.1063/1.2937855` (pages 20, 36, 104).

[44] A. G. Kozorezov, A. F. Volkov, J. K. Wigmore, A. Peacock, A. Poelaert, and R. den Hartog. "Quasiparticle-phonon downconversion in nonequilibrium superconductors". In: *Phys. Rev. B* 61 (17 May 2000), pp. 11807–11819. DOI: `10.1103/PhysRevB.61.11807` (page 21).

[45] S. B. Kaplan, C. C. Chi, D. N. Langenberg, J. J. Chang, S. Jafarey, and D. J. Scalapino. "Quasiparticle and phonon lifetimes in superconductors". In: *Phys. Rev. B* 14 (11 Dec. 1976), pp. 4854–4873. DOI: `10.1103/PhysRevB.14.4854` (page 21).

[46] G. Cataldo, E. M. Barrentine, B. T. Bulcha, N. Ehsan, L. A. Hess, O. Noroozian, T. R. Stevenson, K. U-Yen, E. J. Wollack, and S. H. Moseley. "Second-Generation Design of Micro-Spec: A Medium-Resolution, Submillimeter-Wavelength Spectrometer-on-a-Chip". In: *Journal of Low Temperature Physics* 193 (2018), pp. 923–930. DOI: `10.1007/s10909-018-1902-7` (page 23).

[47] D. C. Mattis and J. Bardeen. "Theory of the Anomalous Skin Effect in Normal and Superconducting Metals". In: *Phys. Rev.* 111 (2 July 1958), pp. 412–417. DOI: `10.1103/PhysRev.111.412` (pages 25, 93).

[48] J. S. Chawla, X. Y. Zhang, and D. Gall. "Effective electron mean free path in TiN(001)". In: *Journal of Applied Physics* 113.6 (2013). DOI: `10.1063/1.4790136` (page 25).

[49] Markus J. Rosch. *Development of lumped element kinetic inductance detectors for mm-wave astronomy at the IRAM 30 m telescope.* 2013 (pages 25, 82).

[50] U. Fano. "Ionization Yield of Radiations. II. The Fluctuations of the Number of Ions". In: *Physical Review* 72 (1947), p. 26. DOI: `10.1103/PhysRev.72.26` (page 32).

[51] M. Kurakado. "Possibility of high resolution detectors using superconducting tunnel junctions". In: *Nuclear Instruments and Methods in Physics Research* 196.1 (1982), pp. 275–277. DOI: `https://doi.org/10.1016/0029-554X(82)90654-1` (page 32).

[52] Jonas Zmuidzinas. "Thermal noise and correlations in photon detection". In: *Applied Optics* 42.25 (2003), p. 4989. DOI: `10.1364/ao.42.004989` (page 34).

[53] L. J. Swenson, P. K. Day, B. H. Eom, H. G. Leduc, N. Llombart, C. M. McKenney, O. Noroozian, and J. Zmuidzinas. "Operation of a titanium nitride superconducting microresonator detector in the nonlinear regime". In: *Journal of Applied Physics* 113.10 (2013), pp. 1–11. DOI: `10.1063/1.4794808` (pages 34, 117, 118).

[54] J. Hubmayr, J. Beall, D. Becker, H. M. Cho, M. Devlin, B. Dober, C. Groppi, G. C. Hilton, K. D. Irwin, D. Li, P. Mauskopf, D. P. Pappas, J. Van Lanen, M. R. Vissers, Y. Wang, L. F. Wei, and J. Gao. "Photon-noise limited sensitivity in titanium nitride kinetic inductance detectors". In: *Applied Physics Letters* 106.7 (2015), pp. 1–4. DOI: `10.1063/1.4913418` (page 34).

[55] John Clarke and Frank K. Wilhelm. "Superconducting quantum bits". In: *Nature* 453.7198 (June 2008), pp. 1031–1042. DOI: `10.1038/nature07128` (page 34).

[56] Jiansong Gao, Miguel Daal, Anastasios Vayonakis, Shwetank Kumar, Jonas Zmuidzinas, Bernard Sadoulet, Benjamin A. Mazin, Peter K. Day, and Henry G. Leduc. "Experimental evidence for a surface distribution of two-level systems in superconducting lithographed microwave resonators". In: *Applied Physics Letters* 92.15 (2008), pp. 1–13. DOI: `10.1063/1.2906373` (page 35).

[57] Clemens Müller, Jared H. Cole, and Jürgen Lisenfeld. "Towards understanding two-level-systems in amorphous solids: Insights from quantum circuits". In: *Reports on Progress in Physics* 82.12 (2019), pp. 1–34. DOI: `10.1088/1361-6633/ab3a7e` (pages 36, 115, 117).

[58] David P. Pappas, Michael R. Vissers, David S. Wisbey, Jeffrey S. Kline, and Jiansong Gao. "Two Level System Loss in Superconducting Microwave Resonators". In: *IEEE Transactions on Applied Superconductivity* 21.3 (2011), pp. 871–874. DOI: `10.1109/TASC.2010.2097578` (page 36).

[59] P. J. De Visser, J. J.A. Baselmans, P. Diener, S. J.C. Yates, A. Endo, and T. M. Klapwijk. "Number fluctuations of sparse quasiparticles in a superconductor". In: *Physical Review Letters* 106.16 (2011), pp. 2–6. DOI: 10.1103/PhysRevLett.106.167004 (page 37).

[60] D. Zhang and Y. Gan. "Recent Progress on Critical Cleaning of Sapphire Single-Crystal Substrates: A Mini-Review". In: *Recent Patents on Chemical Engineering* 6 (2013), pp. 161–166. DOI: 10.2174/2211334707999140331121752 (page 39).

[61] P. Szypryt, B. A. Mazin, G. Ulbricht, B. Bumble, S. R. Meeker, C. Bockstiegel, and A. B. Walter. "High quality factor platinum silicide microwave kinetic inductance detectors". In: *Applied Physics Letters* 109.15 (2016), pp. 1–5. DOI: 10.1063/1.4964665 (page 44).

[62] G. Coiffard, M. Daal, N. Zobrist, N. Swimmer, S. Steiger, B. Bumble, and B. A. Mazin. "Characterization of sputtered hafnium thin films for high quality factor microwave kinetic inductance detectors". In: *Superconductor Science and Technology* 33.7 (2020), pp. 1–9. DOI: 10.1088/1361-6668/ab8d99 (pages 44, 126).

[63] Michael R. Vissers, Jiansong Gao, Jeffrey S. Kline, Martin Sandberg, Martin P. Weides, David S. Wisbey, and David P. Pappas. "Characterization and in-situ monitoring of sub-stoichiometric adjustable superconducting critical temperature titanium nitride growth". In: *Thin Solid Films* 548 (2013), pp. 485–488. DOI: 10.1016/j.tsf.2013.07.046 (page 47).

[64] Faouzi Boussaha, Samir Beldi, Alessandro Monfardini, Jie Hu, Martino Calvo, Christine Chaumont, Florence Levy-Bertrand, Thibaut Vacelet, Alessandro Traini, Josiane Firminy, Michel Piat, and Florent Reix. "Development of TiN Vacuum-Gap Capacitor Lumped-Element Kinetic Inductance Detectors". In: *Journal of Low Temperature Physics* 199.3-4 (2020), pp. 994–1003. DOI: 10.1007/s10909-019-02309-0 (pages 47, 125).

[65] Pieter J. De Visser, Steven A.H. De Rooij, Vignesh Murugesan, David J. Thoen, and Jochem J.A. Baselmans. "Phonon-Trapping-Enhanced Energy Resolution in Superconducting Single-Photon Detectors". In: *Physical Review Applied* 16 (3 2021), pp. 1–14. DOI: 10.1103/PhysRevApplied.16.034051 (pages 59, 94).

[66] Maurice H. Bernstein and Daniel C. Pease. "Electron Microscopy of the Tapetum Lucidum of the Cat ". In: *The Journal of Biophysical and Biochemical Cytology* 5.1 (Jan. 1959), pp. 35–39. DOI: 10.1083/jcb.5.1.35 (page 60).

[67] C. Bracken, G. de Lange, M. D. Audley, N. Trappe, J. A. Murphy, M. Gradziel, W. J. Vreeling, and D. Watson. "A novel, highly efficient cavity backshort design for far-infrared TES detectors". In: *Infrared Physics and Technology* 89 (Mar. 2018), pp. 194–202. DOI: 10.1016/j.infrared.2018.01.004 (page 60).

[68] M. Dai, W. Guo, X. Liu, M. Zhang, Y. Wang, L. F. Wei, G. C. Hilton, J. Hubmayr, J. Ullom, J. Gao, and M. R. Vissers. "Measurement of Optical Constants of TiN and TiN/Ti/TiN Multilayer Films for Microwave Kinetic Inductance Photon-Number-Resolving Detectors". In: *Journal of Low Temperature Physics* 194.5-6 (2019), pp. 361–369. DOI: 10.1007/s10909-018-2095-9 (pages 60, 73, 79, 92).

[69] K. Kouwenhoven, I. Elwakil, J. van Wingerden, V. Murugesan, D. J. Thoen, J. J. A. Baselmans, and P. J. de Visser. "Model and Measurements of an Optical Stack for Broadband Visible to Near-IR Absorption in TiN KIDs". In: (2021), pp. 1–7. DOI: 10.1007/s10909-022-02774-0 (pages 60, 62, 79, 92).

[70] I. Chambouleyron and J.M. Martinez. "Optical properties of dielectric and semiconductor thin films". In: *Handbook of Thin Films* 3 (2002), pp. 593–622. DOI: 10.1016/b978-012512908-4/50048-5 (page 62).

[71] I. H. Malitson. "Interspecimen Comparison of the Refractive Index of Fused Silica". In: *Optical Society of America* 55 (1965), pp. 1205–1209. DOI: 10.1364/JOSA.55.001205 (page 65).

[72] Jinchao Liu, Di Zhang, Dianqiang Yu, Mengxin Ren, and Jingjun Xu. "Machine learning powered ellipsometry". In: *Light: Science and Applications* 10.1 (2021). DOI: 10.1038/s41377-021-00482-0 (page 66).

[73] A. G. Mathewson and H. P. Myers. "Absolute Values of The Optical Constants of Some Pure Metals". In: *Physica Scripta* 4.6 (1971), pp. 291–292. DOI: 10.1088/0031-8949/4/6/009 (page 67).

[74] Samir Beldi, Faouzi Boussaha, Jie Hu, Alessandro Monfardini, Alessandro Traini, Florence Levy-Bertrand, Christine Chaumont, Manuel Gonzales, Josiane Firminy, Florent Reix, Michael Rosticher, Shan Mignot, Michel Piat, and Piercarlo Bonifacio. "High Q-factor near infrared and visible Al 2 O 3 -based parallel-plate capacitor

kinetic inductance detectors". In: *Optics Express* 27.9 (2019), p. 13319. DOI: `10.1364/oe.27.013319` (pages 70, 86, 88, 96).

[75] Ahmet Lale, Emmanuel Scheid, Fuccio Cristiano, Lucien Datas, Benjamin Reig, Jérome Launay, and Pierre Temple-Boyer. "Study of aluminium oxide thin films deposited by plasma-enhanced atomic layer deposition from tri-methyl-aluminium and dioxygen precursors: Investigation of interfacial and structural properties". In: *Thin Solid Films* 666.September (2018), pp. 20–27. DOI: `10.1016/j.tsf.2018.09.028` (page 70).

[76] E. Shkondin, T. Repän, O. Takayama, and A. V. Lavrinenko. "High aspect ratio titanium nitride trench structures as plasmonic biosensor". In: *Optical Materials Express* 7.11 (2017), p. 4171. DOI: `10.1364/ome.7.004171` (page 73).

[77] Paul Nicaise, Jie Hu, Jean Marc Martin, Samir Beldi, Christine Chaumont, Piercarlo Bonifacio, Michel Piat, Hervé Geoffray, and Faouzi Boussaha. "Investigation of Optical Coupling in Microwave Kinetic Inductance Detectors Using Superconducting Reflective Plates". In: *Journal of Low Temperature Physics* 0123456789 (2022). DOI: `10.1007/s10909-022-02789-7` (pages 88, 93).

[78] R. Barends, H. L. Hortensius, T. Zijlstra, J. J. A. Baselmans, S. J. C. Yates, J. R. Gao, and T. M. Klapwijk. "Contribution of dielectrics to frequency and noise of NbTiN superconducting resonators". In: (Apr. 2008). DOI: `10.1063/1.2937837` (pages 93, 123).

[79] Elmira M. Baeva, Nadezhda A. Titova, Louis Veyrat, Benjamin Sacépé, Alexander V. Semenov, Gregory N. Goltsman, Anna I. Kardakova, and Vadim. S. Khrapai. "Thermal Relaxation in Metal Films Limited by Diffuson Lattice Excitations of Amorphous Substrates". In: *Physical Review Applied* 15.5, 054014 (May 2021), p. 054014. DOI: `10.1103/PhysRevApplied.15.054014` (page 94).

[80] Yiwen Wang, Pinjia Zhou, Lianfu Wei, Haijie Li, Beihong Zhang, Miao Zhang, Qiang Wei, Yurong Fang, and Chunhai Cao. "Photon-induced thermal effects in superconducting coplanar waveguide resonators". In: *Journal of Applied Physics* 114.15 (2013), pp. 1–5. DOI: `10.1063/1.4826271` (page 104).

[81] J. Bueno, P. C.J.J. Coumou, G. Zheng, P. J. De Visser, T. M. Klapwijk, E. F.C. Driessen, S. Doyle, and J. J.A. Baselmans. "Anomalous response of superconduct-

ing titanium nitride resonators to terahertz radiation". In: *Applied Physics Letters* 105.19 (2014), pp. 1–5. DOI: `10.1063/1.4901536` (page 107).

[82]   Panos Patsalas, Nikolaos Kalfagiannis, and Spyros Kassavetis. "Optical properties and plasmonic performance of titanium nitride". In: *Materials* 8.6 (2015), pp. 3128–3154. DOI: `10.3390/ma8063128` (page 115).

[83]   Anton Kozma. "Thermodynamic, Thermal and Elastic Properties of Titanium Nitride TiN: Comparison of Various Data and Determination of the Most Reliable Values". In: *Technology transfer: fundamental principles and innovative technical solutions* 4 (Nov. 2020), pp. 14–17. DOI: `10.21303/2585-6847.2020.001475` (page 115).

[84]   W. A. Phillips. "Two-level states in glasses". In: *Reports on Progress in Physics* 50.12 (1987), pp. 1657–1708. DOI: `10.1088/0034-4885/50/12/003` (page 115).

[85]   Albert Wandui, James J. Bock, Clifford Frez, M. Hollister, Lorenzo Minutolo, Hien Nguyen, Bryan Steinbach, Anthony Turner, Jonas Zmuidzinas, and Roger O'Brient. "Thermal kinetic inductance detectors for millimeter-wave detection". In: *Journal of Applied Physics* 128.4 (2020), pp. 1–18. DOI: `10.1063/5.0002413` (page 117).

[86]   P. J. De Visser, D. J. Goldie, P. Diener, S. Withington, J. J.A. Baselmans, and T. M. Klapwijk. "Evidence of a nonequilibrium distribution of quasiparticles in the microwave response of a superconducting aluminum resonator". In: *Physical Review Letters* 112.4 (2014), pp. 1–10. DOI: `10.1103/PhysRevLett.112.047004` (page 118).

[87]   Jie Hu, Faouzi Boussaha, Jean Marc Martin, Paul Nicaise, Christine Chaumont, Samir Beldi, Michel Piat, and Piercarlo Bonifacio. "Large inverse transient phase response of titanium-nitride-based microwave kinetic inductance detectors". In: *Applied Physics Letters* 119.21 (2021). DOI: `10.1063/5.0074103` (page 119).

[88]   J. Wheeler, M. R. Vissers, M. Malnou, J. Hubmayr, J. N. Ullom, and J. Gao. "Sub-Kelvin Thermometer for On-Chip Measurements of Microwave Devices Utilizing Two-Level Systems in Superconducting Microresonators". In: (Nov. 2020). DOI: `10.1063/5.0029351` (page 121).

[89]   O. Wen, T. Aralis, R. Basu Thakur, B. Bumble, Y. -Y. Chang, K. Ramanathan, and S. R. Golwala. "Performance of a Phonon-Mediated Detector Using KIDs Optimized for Sub-GeV Dark Matter". In: *Journal of Low Temperature Physics* (July 2022). DOI: `10.1007/s10909-022-02764-2` (page 127).

RÉSUMÉ

Les détecteurs à inductance cinétique (MKIDs) sont des résonateurs LC à haut facteur de qualité faits à partir de couches minces supraconductrices. Ils peuvent simultanément déterminer le temps d'arrivée de chaque photon en mesurant leur énergie sans optique supplémentaire. Grâce au pouvoir de multiplexage des MKIDs qui permet de facilement réaliser des matrices de plusieurs kilopixels, cette technologie est au centre de l'attention pour les nouvelles applications en astronomie. Parmi eux se trouve l'instrument SpectroPhotometric Imaging for Astronomy with Kinetic Inductance Detectors (SPIAKID), projet du GEPI à l'Observatoire de Paris. Nous utilisons la technologie MKID pour construire un spectrophotomètre composé de 20 000 pixels qui sera déployé sur le New Technology Telescope (NTT) de 3.6m au Chili à l'horizon 2025. SPIAKID s'intéressera à la population stellaire des galaxies naines ultra faibles du Groupe Local pour mieux comprendre la formation des galaxies ainsi que la matière noire. Nous présenterons dans ce travail de thèse un design novateur pour améliorer le couplage optique entre les photons incidents et la partie sensible du détecteur ainsi qu'une réponse anormale de notre supraconducteur qui pourrait faire l'objet d'un nouveau moyen de détection.

MOTS CLÉS

détecteur – supraconductivité – inductance cinétique – optique et infrarouge proche – couplage optique – interactions des phonons

ABSTRACT

Microwave Kinetic Inductance Detectors (MKIDs) are superconductive thin films LC resonators with high quality factors. They can simultaneously record single-photon events and measure their energy without any added optics. Combined with the ease of multiplexing thousands of pixels into a large array, MKIDs are now at the heart of current and upcoming ground-based astronomy applications. Among them is the SpectroPhotometric Imaging for Astronomy with Kinetic Inductance Detectors (SPIAKID) project at Paris Observatory. We are using MKID technology to build a 20,000 pixels spectrophotometer that will be deployed in 2024 on the 3.58m New Technology Telescope (NTT) in Chile. SPIAKID aims to study the population and metallicity of stars in Ultra Faint Dwarf (UFD) galaxies in the Local group to have a better understanding of galaxy formation and evolution. We will present an original design intended to improve the optical coupling between incident photons and the absorber part of the detector as well as an anomalous response from our superconductor that could offer a new mean of detection.

KEYWORDS

detector – superconductivity – kinetic inductance – optical and near-infrared – optical coupling – phonon interactions